CONVECTIVE STRUCTURE AND ITS EVOLUTION IN TROPICAL CYCLONES AS OBSERVED BY PASSIVE MICROWAVE SENSORS IN RELATION TO INTENSITY CHANGE

BY

DANIEL HARNOS

THESIS

Submitted in partial fulfillment of the requirements
for the degree of Master of Science in Atmospheric Sciences
in the Graduate College of the
University of Illinois at Urbana-Champaign, 2010

Urbana, Illinois

Adviser:

Assistant Professor Stephen W. Nesbitt

ABSTRACT

The use of passive microwave sensors in analysis of tropical cyclones provide unique insight into the microphysical attributes and system structure opposed to other instruments that are only able to detect information about the cloud top. With the ability to infer information about key microphysical processes and structure at high resolution, these platforms provide a glimpse into tropical cyclone development and intensification over systems' life cycles. In particular, passive microwave observations have the potential to depict crucial precursors of rapid intensification (RI; defined as a wind increase of 30 kt/24 hr).

A dataset with a common resolution of 8 km across all channels is developed for the Special Sensor Microwave Imager (SSM/I) from 1987-2008 and Tropical Rainfall Measuring Mission Microwave Imager (TMI) for 1997-2008. Statistical metrics are calculated for each storm overpass using 85 GHz and 37 GHz polarization corrected temperatures as well as microwave rain rate estimates. These products are examined as a function of azimuth and annuli in true-north, storm-relative motion, and shear-relative coordinates and evaluated in terms of intensity (wind speed) and intensity change (wind speed change over time).

To examine predictive potential of these sensors, the brightness temperature statistics are evaluated in terms of linear correlations between intensity and its change. Highest values occur on the order of 0.7, and are seen at radii of 110 km between median values for 85 GHz PCT and rain rates with observed intensity. An increase in skill is evident following the initial satellite overpass, suggesting a lag between latent heating at the time

of overpass and the resultant intensification. Despite this, correlation is consistently less skillful for evaluations of intensity change with values at short time changes of around 0.3.

The distribution of statistical values are also evaluated in the context of the dataset with median values at the 110 km distance showing the greatest distinction of 85 GHz PCTs and rain rates for storms at the onset of RI and those that are not, with less variation seen for percentiles $\geq$ 90% that are indicative of isolated convective activity. With the differentiation in structure noted between RI and non-RI storms, composites are created for each of the brightness temperature products, with a distinct modest convective ring structure evident at the onset of RI that is not present in the non-RI class. Over time this convective ring shows a tendency to contract and intensify over the 24 hour period examined for RI, with the increased latent heating over a more focused area acting to increase the system intensity. Through these evaluations the continued importance spatial convective coverage and axisymmetricization is underscored in intensity and intensity change evaluation, with a lack of signal seen in more isolated convective predictors.

For my loving parents, Barry and Ginny.

ACKNOWLEDGEMENTS

The work contained within this thesis is an accumulation of hard work that I would have been unable to accomplish without the outstanding people around me. The writing within may be mine, but the path to it has had countless contributors along the way.

First are undoubtedly my parents, for their undying support pushing me to become a better person and make the most of every opportunity. The man I am today is a complete result of their years of patience and teaching. Without their steady presence I would be nowhere near the person that I am today and for that I am forever grateful.

Many thanks must be given to my research advisor, Steve Nesbitt. I appreciate him taking me on in the first place in addition to his constant oversight and vision throughout. Steve has been a consistent positive voice and the best advisor I could imagine.

My future wife, Kirstin Gleicher, has been outstanding in a support role and providing feedback on preliminary work. I am grateful for her putting up with many long workdays and making sure I still took care of myself. Chase and Oscar also get thanks for kitty stress relief throughout this research.

The Nesbitt research group (Wendi Kaufeld, Nicole Schiffer, and Kim Reed) have all played a role in this. In particular thanks go to Wendi, as she has been an outstanding mentor since I began graduate school and recruited me to Steve in the first place (and likely regrets it to this day!). All of you however have been co-advisors in my mind and helped keep me sane. The entire atmospheric sciences community at the University of Illinois has played a role in my development as a student, researcher, and person and I thank them.

This work has been funded by NASA grant NNX09AB82G awarded through the Hurricane Science Research Program

TABLE OF CONTENTS

CHAPTER 1: INTRODUCTION AND LITERATURE REVIEW……1
1.1 TROPICAL CYCLONES……1
1.2 RAPID INTENSIFICATION……2
1.3 PASSIVE MICROWAVE SENSORS……5

CHAPTER 2: DATA AND METHODOLOGY……11
2.1 SATELLITE DATA……11
2.2 BEST TRACK DATA……13
2.3 NCEP/NCAR REANALYSIS DATA……14
2.4 METHODOLOGY……14

CHAPTER 3: RESULTS……18
3.1 RELATIONSHIPS BETWEEN PM PRODUCTS AND TC INTENSITY……18
3.2 TC STRUCTURAL VARIATIONS BY INTENSITY CHANGE……37
3.3 EVOLUTION OF TC STRUCTURE DURING RI……53

CHAPTER 4: CONCLUSIONS……105

REFERENCES……115

CHAPTER 1

INTRODUCTION AND LITERATURE REVIEW

1.1 - Tropical Cyclones

Tropical cyclones (TCs) present a two-fold challenge for forecasting offices across the globe when it comes to their prediction, as the most recent report released from the National Hurricane Center (NHC; Rappaport et al., 2009) revealed diverging courses when it came to track and intensity forecasts. During the period 1970-2008, North Atlantic track forecast accuracy increased on the order of 3%/year since 1990, resulting largely from improvements in data assimilation, model parameterizations, and forecast model resolution. These trends do not hold true however for intensity; a minimal increase of skill on the order of 10% total occurred from 1990-2008.

These deficiencies in regard to intensity forecasts lend themselves to the difficulty in understanding and observing meso- to micro-scale processes taking place within the inner-core of the system that drive the circulation of the larger cyclone. Low-level inflow near the surface flows towards the low pressure of the TC core, causing moisture to evaporate as the air traverses the sea surface. This inflow converges into the outward sloping eyewall, where latent heat is released aloft increasing the warm thermal anomaly. As a byproduct of this heating aloft, the pressure within the eye decreases hydrostatically, further increasing inflow to the eyewall. This positive feedback process acts to develop and sustain the TC in absence of outside influences.

The inner-core of TCs are inherently difficult to observe due to the system's location over water in their formative and developmental stages. Direct observation is further

hindered by the violent nature of the core region, introducing uncertainty in any measurements of key properties such as aerosols and microphysical parameters that are present due to the high winds. Satellites present an outstanding observing tool with expansive coverage of the tropics, however a majority of satellites operate in the visible or infrared wavelengths and are rendered nearly useless from obscuration of the TC structure by cirrus outflow.

1.2 - Rapid Intensification

One particularly compelling issue complicating intensity forecasts is that of storms undergoing rapid intensification (RI; also frequently described as rapid deepening). Numerous definitions have been used to classify storms undergoing RI however no clear consensus of a criteria has been agreed upon. A study by Kaplan and DeMaria (2003) of the North Atlantic basin determined a definition of RI of 30 kts/24 hrs by utilizing the 95th percentile of intensity changes for TCs from 1989-2000. A more recent study by Kaplan et al. (2010) determined that this 30 kt/24 hr criteria represented intensity changes in the 90th percentile in the North Atlantic and 92nd percentile for the East Pacific. The NHC officially defines rapid deepening as "a decrease in the minimum sea-level pressure of a tropical cyclone of 1.75 mb/hr or 42 mb for 24 hours"[1]. Regardless of a consensus definition, the NHC recently declared "The slow rate of improvement in intensity forecast accuracy and skill, and the particularly large errors that can occur in episodes of rapid intensification, have prompted NHC to elevate this deficiency to its top priority for the tropical meteorology research community" (Rappaport et al, 2009).

[1] NHC glossary of terms: http://www.nhc.noaa.gov/aboutgloss.shtml

RI has been linked with a host of asymmetric structural features resulting from strong ambient wind shear. Frank and Ritchie (1999; 2001) and Kaplan and DeMaria (2003) have documented the propensity of storms to undergo RI when under regions of weak vertical wind shear, however this has not shown to be entirely consistent. Mesovorticies and the development of convective asymmetries forced by wind shear has been documented by Braun et al. (2006) as the vortex was tilted throughout its intensification period and stalled as the vortex became vertically stacked. Nolan and Montgomery (2002) detail the importance of mesovorticies in mixing high θ_e air into the eyewall, resulting from the reduced central pressure of the system due to vorticity mixing from the eyewall into the eye. Molinari and Vollaro (2010) have shown the evolution of multiple TC centers during the evolution of RI in a highly sheared environment with an upright inner vortex and more tilted counterpart outside of this in Tropical Storm Gabrielle (2001).

The body of evidence for the importance of symmetric core structure in TCs undergoing RI is also extensive. The axisymmetric component of heating has been shown to dominate the asymmetric component during intensification by the work of Nolan and Grasso (2003). Miyamoto (2010) has shown that prior to RI asymmetries prevail and as the system undergoes RI, the axisymmetic component grows to quickly dominate the system structure. Rodgers (2010) has shown in simulations of Hurricane Dennis (2005) an increase in areal coverage of convection precludes RI initiation. Observationally, banded (axisymmetric) precipitation has been frequently noted by reconnaissance flights just prior to eye formation and periods of hurricane intensification (Vigh, 2010).

The societal impacts of RI are the underlying reason necessitating improved forecasts of its occurrence. With increasing populations along the global coastlines and property values rising coastal vulnerability to TC activity has been freqeuent (Willoughby et al., 2010; Pielke et al., 2008). However, efforts must be taken to determine the causes and potential predictors of RI to better predict impact of landfalling hurricanes. Examination of the global distribution of RI utilizing the International Best Track Archive for Climate Stewardship (IBTrACS; Knapp et al., 2010) along with the North American definition of Kaplan and DeMaria (2003) of 30 kt/24 hr shows the propensity of RI to occur near coastlines clustered around 15° latitude with a particular coastal focus in the East Pacific south of Mexico and the West Pacific east of the Phillipines (Figure 1a). Normalizing RI frequency by storm count (Figure 1b) shows that 20-40% of all storms in most regions globally experiencing TCs undergo RI, with a few preferred locations where all or nearly all storms have undergone RI in the East and South Pacific. In the United States the only storm in recent years to undergo RI shortly prior to landfall was Charley (2004) that saw its winds increase from 110 to 145 mph (Category 2 to Category 4) over a 3-hour span as it approached the Florida coast. Fortunately the core and its radius of maximum winds were relatively compact, averting disaster as the unexpected intensification that took place was not foreseen and the evacuation orders were accordingly not on level with a storm of Charley's observed intensity.

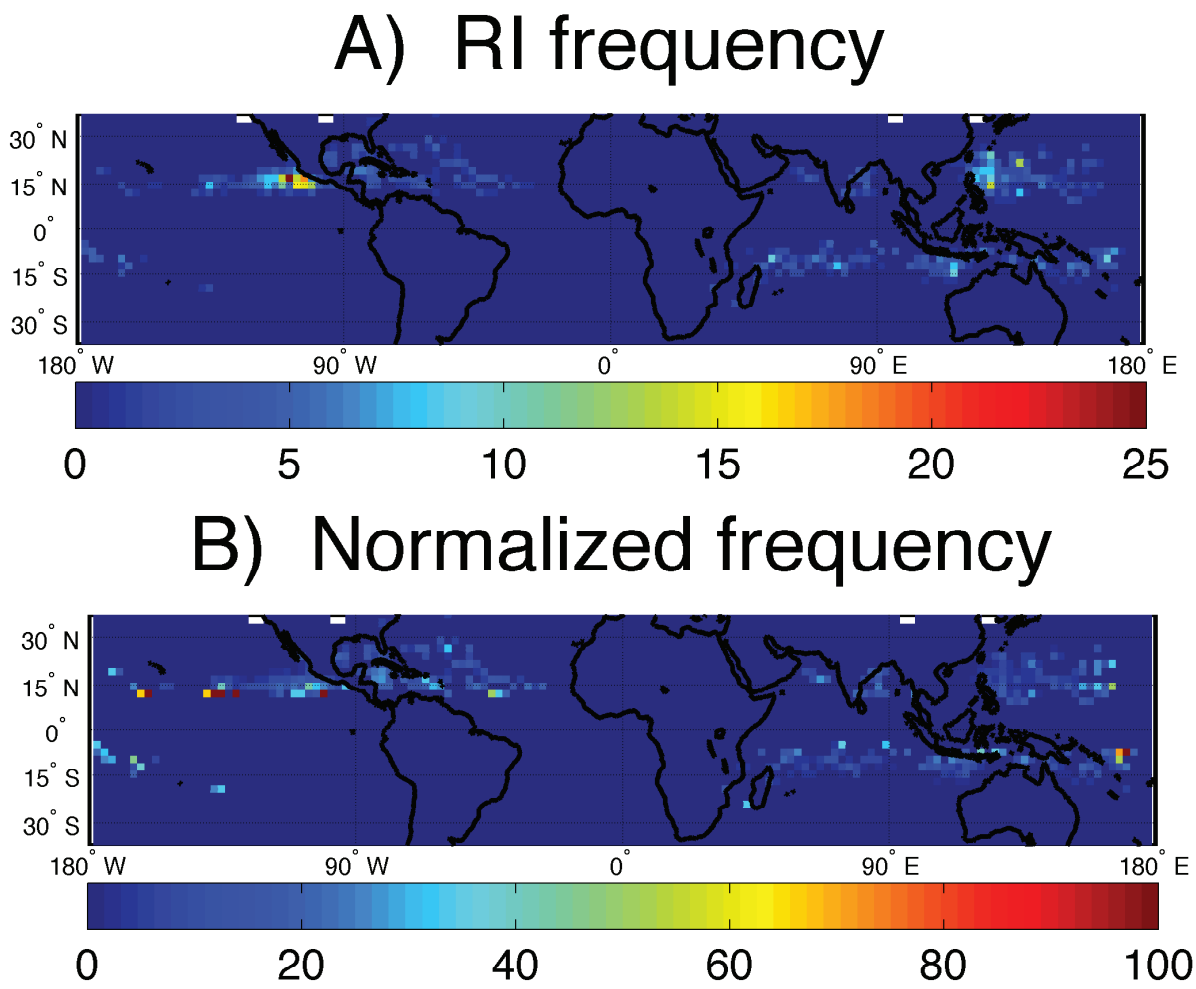

Figure 1: Frequency of RI initiation for 1987-2008 (a; #) and normalized by total storm count (b; %). Grid is 2.5°.

1.3 - Passive Microwave Sensors

In recent years the utility of passive microwave (PM) sensors has come to the forefront of TC study, due to the observations being easily relatable to precipitation characteristics and as the number of available platforms has grown. Current instruments in operation include the Special Sensor Microwave/Imager (SSM/I) onboard the Defense Meteorological Satellite Program (DMSP) orbiters, Tropical Rainfall Measurement Mission Microwave Imager (TMI), Special Sensor Microwave Imager/Sounder (SSMIS) on DMSP-16, and Advanced Scanning Microwave Radiometer-EOS (AMSR-E) flying on NASA's Aqua

satellite. Additional microwave sensors are planned in the coming years with the Megha-Trophiques mission (Roca, 2010) as well as the Global Precipitation Measurement mission (Smith et al., 2004).

The advantage of PM platforms when observing TCs is the relative transparency to clouds yielding the ability to detect the structure of precipitation and cloud features. Lower frequency microwave channels such as 10 and 19 GHz have shown utility in sensing emission of liquid rain whereas higher frequency channels such as 37 and 85 GHz can utilize ice scattering as a proxy for updraft intensity (McGaughey et al. 1996; Vivekanandan et al., 1991). Recalling Mie theory, scattering at 37 GHz is a result of graupel and large ice particles whereas at 85 GHz scattering is a byproduct of smaller cloud ice. An example of the utility of PM observations is seen in Figure 2, showing Hurricane Jimena from 2001 when the storm had an estimated wind speed of 125 kt. With such extreme winds one would expect an eye to persist, however the IR image (Fig. 2a) shows no hint of an eye, whereas the TMI overpass (Fig. 2b) at the same time reveals more information about the inner core of the system: a clear pinhole eye surrounded by convection, unaffected opposed to the IR image contaminated by the central dense overcast.

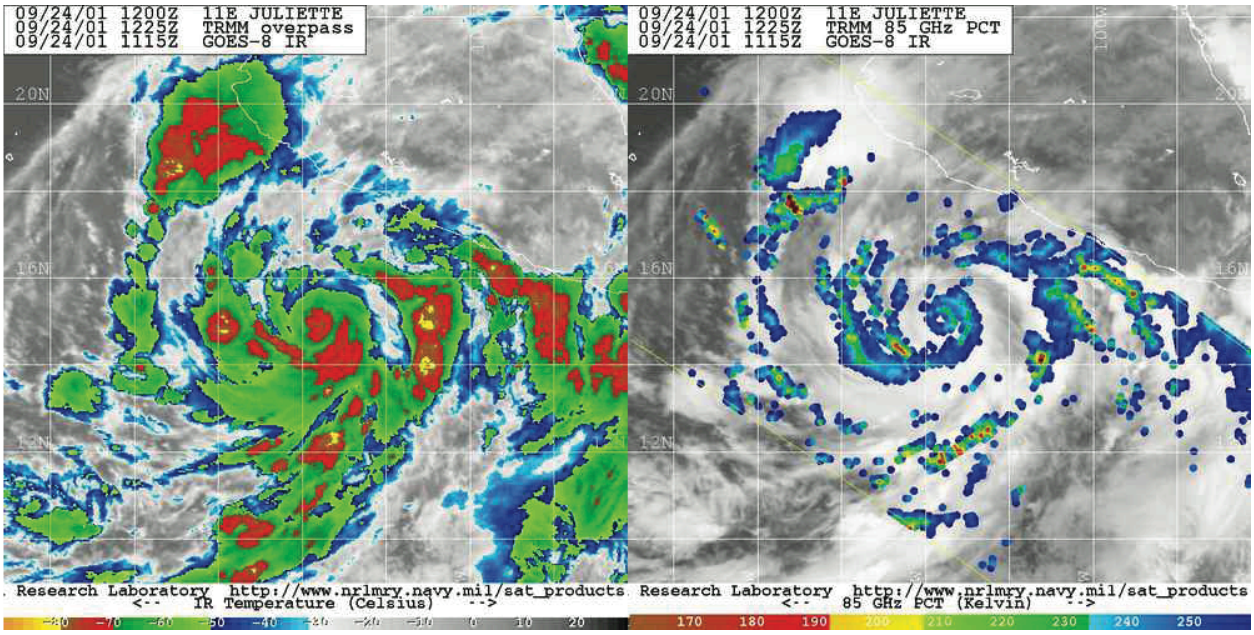

Figure 2: Brightness temperature comparisons for IR (left) and PM (right – 85 GHz polarization corrected temperature) of East Pacific Hurricane Jimena (2001) on 24 September 2001 when the storm had an estimated intensity of 125 kts. Image courtesy of the Naval Research Laboratory's Tropical Cyclone page.

Studies of passive microwave satellite observations of TCs have occurred sporadically since the launch of the first SSM/I in 1987. The studies have for the most part focused on commonly observed trends in brightness temperature or other algorithm fields for a single basin over one hurricane season. The first of these was by Rodgers et al. (1994) who examined 103 SSM/I derived inner-core rain rates for the North Atlantic from 1987-1989 and determined that in fast moving systems (defined as: $\geq$ 15 kt) that the majority of rainfall occurred to the right of storm motion, while for slow moving systems (< 8 kt) it was in the forward half. Rao and MacArthur (1994) observed 12 West Pacific typhoons for 27 viewings between 1987-1988 and noted that SSM/I derived rain volume rates (rain rates averaged over an specified area) for the region extending out to 444 km had a strong correlation with 24 hr future intensity. In addition, they noted that deepening storms moving to the northwest had higher light rain volume rates within a region extending to 222 km. Rodgers and Pierce (1995) examined West Pacific systems with a much larger

sample size of 1018 SSM/I samples from 1987-1992 and attempted to correlate spatial increases in core rain rates with 12 and 24 hour intensity changes with widely varied results. They did however did show that the duration and extent of diabatic heating played a key role in system intensification with large increases in heating initiating and sustaining periods of intensification, in particular when the period was prolonged. Rao and McCoy (1997) examined 1° annuli of 85 GHz vertically polarized brightness temperatures in relation to 12 and 24-hour future intensities for 29 overpasses in the West Pacific from 1987 and observed a correlation of 0.82 for typhoons moving northwestward and a 24 hour intensity change correlation of 0.5. Cecil and Zipser (1999) utilized 265 SSM/I overpasses from the North Atlantic, East Pacific, and West Pacific to show skill in the use of SSM/I 85 GHz brightness temperatures and estimation of wind speed, however little merit was found in use of this as a proxy for intensity change. Cecil et al. (2002) along with Cecil and Zipser (2002) used TMI, TRMM's Precipitation Radar, and TRMM's Lightning Imaging Sensor in a holistic perspective to determine TC precipitation characteristics in comparison to other forms of oceanic and continental convection. Ice-scattering at 85 GHz is associated with convection-induced ice-scatter at higher levels within TCs, and 37 GHz scattering being a product of large cloud ice at lower levels as determined by Cecil and Zipser (2002). Rainfall distributions from 2121 global TMI observations over 1998-2000 were examined by Lonfat et al. (2004) with Fourier analysis and determined that globally, peak rain rates contracted as TCs intensified as well as a shift in wavenumber-1 asymmetries from the front left quadrant of the system to the front right as intensification occurred. An attempt using TMI 10 and 19 GHz brightness temperatures to estimate storm intensity was made by Hoshino and Nakazawa (2007) through a relationship of wind speed to both emission

and scattering channels. Their study spanned from 1999-2003 globally and saw core minimum and mean brightness temperatures at these low frequency channels resulting in correlations on the order of 0.7 with system intensity. Kieper (2008) advocated the use of 37 GHz data in detection of a thick ring of precipitation prior to episodes of RI for the North Atlantic from 2003-2007, despite questions relating to the subjective nature of the authors's methodology. Velden et al. (2010) further examined this 37 GHz ring idea.

Despite these studies the use of PM data in operational algorithms relating to storm intensity and intensity change has been slow to take hold. At present only the Statistical Hurricane Intensity Prediction Scheme (SHIPS) has a microwave scheme, and it is fairly simple with only a few brightness temperature parameters (mean, median, standard deviation, and minimum) included in a minimalistic predictor scheme (Jones et al., 2006). More recently the Advanced Dvorak Technique has looked to improve upon its more traditional counterpart by augmenting intensity analyses prior to an eye forming in infrared imagery (Sears et al., 2010).

The focus of this work is to examine intensity changes and specifically RI in the context of information available from PM sensors. Specific structural features detectable by PM sensors such as banding of precipitation features, convective asymmetries, and the like are examined in the context of wind shear and sea surface temperatures. The frequencies and distributions of brightness temperatures occurring prior to episodes of RI has not been ascertained and once quantified can provide a solid baseline for its forecast. Additionally, the importance and role of asymmetric versus axisymmetric structures has not been determined. With the increased availability of PM data in the near future it is

imperative to develop algorithms that will be able to utilize these platforms for intensity estimation and prediction as the sensors become operational.

CHAPTER 2

DATA AND METHODOLOGY

2.1 - Satellite Data

Data from two current conically-scanning passive microwave platforms in orbit are utilized in this study. The first of these is the Special Sensor Microwave/Imager (SSM/I), which has flown on board the Defense Meteorological Satellite Program satellites (F-8 through F-15) since 1987. These satellites have limited daily coverage as they are polar orbiting, so several-hour gaps often exist between sampling of TCs. The SSM/I operates at both horizontal and vertical polarizations for 19.35 GHz, 37.0 GHz, and 85.5 GHz in addition to 22.235 GHz in just the vertical. The sensor first launched in 1987 on F-8 and data in this study spans from July of that year through December 2008. A more comprehensive overview of SSM/I can be found in Hollinger (1991).

Additionally, brightness temperature observations Tropical Rainfall Measuring Mission's Microwave Imager (TMI) were used. The TMI was launched in November 1997 and operates in vertical and horizontal polarizations at 10.65, 19.35, 37.0, and 85.5 GHz and observes at 21.3 GHz in vertical polarization only. More background on TMI can be found in Kummerow et al. (1998). TRMM became operational in 1997 and the timeframe for this study consists of data from December 1997 through December 2008. The TMI instrument was based off of the SSM/I, as evidenced in the similarity among the channel frequencies, making the two a natural source for comparison.

Due to varying resolutions across both channel and platform, additional treatment of the satellite data is necessary to allow for meaningful comparison across platforms. The

HURSAT-MW dataset (Knapp, 2008) is the source for the SSM/I data, and its characteristics are applied to TMI overpasses of TCs. Using IBTrACS best track data (described below), TMI orbital overpasses of tropical storms are regridded as in HURSAT-MW, whereby the 6-hourly best track data are interpolated to the time of the satellite overpass. For both SSM/I and TMI data, the estimated storm center from best track data is used as the center of the grid, and swath brightness temperatures at all frequencies are linearly interpolated to a common 8 km resolution. Due to occasional instrument failures, in particular with SSM/I F-8 shortly following its launch, a quality control procedure was applied to all overpasses to ensure valid brightness temperature information. The quality control was performed by searching the individual overpasses for anomalously high or low brightness temperature values. In addition, missing portions of the swaths were identified in individual channels, as this had the potential to contaminate empirical brightness temperature products.

A number of algorithms developed for passive microwave data are utilized in an attempt to derive more tangible results from brightness temperature data. The first of which is the empirically derived rain rate (RR) algorithm over water from Ferraro and Marks (1995) for SSM/I:

$$RR = .0015 \times SI^{2.022}$$

where SI, the scattering index, is defined as:

$$SI = -174.4 + 0.72T_{19}^{V} + 2.439T_{22}^{V} - .00504\left(T_{22}^{V}\right)^{2} - T_{85}^{V}$$

with the subscript indicating the frequency of the channel and the superscript its polarization. For the aforementioned algorithm it is assumed that the vertically polarized TMI channel of 21 GHz can be substituted for the 22 GHz channel of SSM/I, as a comparison

of the rain rate distributions (not shown) for SSM/I and TMI yielded little difference. A 5 km land mask is applied, as the algorithm is valid only for oceanic regimes. The land ocean mask was derived from the National Geophysical Data Center's ETOPO2 version 2 global digital elevation model[2]. The DEM has a spatial resolution of 2 arc minutes, and was thresholded on elevations greater than zero as being land, and water elsewhere.

Lastly two techniques to determine polarization corrected temperatures (PCTs) were applied to the 85 GHz and 37 GHz channels in line with the relationships found by Spencer et al. (1989) and Cecil et al. (2002) respectively:

$$PCT_{85} = 1.818T_{85}^{V} - 0.818T_{85}^{H}$$
$$PCT_{37} = 2.20T_{37}^{V} - 1.20T_{37}^{H}$$

These equations correct for the impact of varying land surface emissivities and assumed background water vapor levels on brightness temperatures as opposed to the radiometrically cold ocean (Grody and Weng, 2008).

2.2 - Best Track Data

Best track data is utilized from the International Best Track Archive for Climate Stewardship (IBTrACS; Knapp, et al. 2010). This archive is a database that is globally consistent across regional forecasting centers and the most extensive TC database available at present. The satellite data are interpolated to the nearest best track records when analysis is performed, therefore temporal errors of up to 3 hours may be present. For the purpose of this study wind speed (V) is chosen as the measure of intensity. In addition to

[2] http://www.ngdc.noaa.gov/mgg/global/etopo2.html.

wind data, storm motion is derived from latitude and longitude values and storms are stratified according to their oceanic basin for further comparison. The regions encompassing the 7 oceanic basins are depicted in Figure 3.

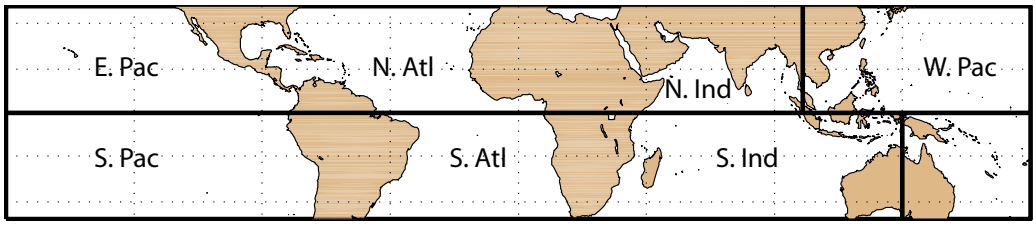

Figure 3: Oceanic basin ranges. Continental coastlines and thick black lines signify boundaries. The South Pacific basin extends across the International Date Line.

2.3 - NCEP/NCAR Renanalysis Data

For environmental information the NCEP/NCAR reanalysis (Kalnay, et al. 1996) is utilized. The spatial resolution of the data is 2.5° with a temporal resolution of 6 hours. Wind shear is determined from the reanalysis data according to the difference between the 850 hPa and 200 hPa u and v winds. Sea surface temperature (SST) information is also utilized from the skin temperature metric in conjunction with the land mask mentioned earlier, by interpolating in a nearest-neighbor manner the estimated best-track location to the reanalysis.

2.4 - Methodology

Each satellite overpass is analyzed via 55 km (0.5 degree) additive annuli as well as azimuth. Three coordinate systems were utilized, true-north, storm-motion relative, and wind shear relative. Brightness temperatures and derived values are analyzed according to

these additive annuli and in half/quadrant regions determined by the coordinate framework chosen in order to better diagnose structural features. An example of the framework is depicted in Figure 4.

For each region basic statistical quantities are determined, including the: mean, median, minimum (maximum in the case of rain rate), and percentiles at the 75th, 90th, 95th, 99th, and 99.9^{th} values. These values for each overpass are stratified according to the storm's basin and its intensity change status. The definition chosen for RI is $\Delta V \geq 30$ kts/24 hrs as in Kaplan and DeMaria (2003), which corresponds to the top 4 % of intensity changes, nearly in line with their 5%. Other definitions utilized are intensifying (30 kts/24 hrs > $\Delta V \geq 10$ kts/24 hrs), steady state (10 kts/24 hrs > ΔV > -10 kts/24 hrs), and weakening ($\Delta V \leq$ -10 kts/24 hrs). All storms that do not undergo RI (ΔV < 30 kts/ 24 hrs) are classified as non-rapid intensification (nonRI).

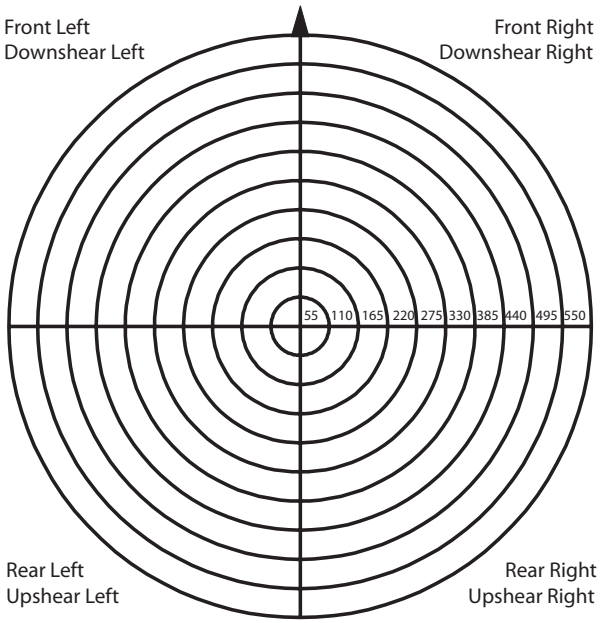

Figure 4: Example of the coordinate system utilized for analysis. The radii are at additive 55 km (0.5°) values from the estimated center of the TC. Storm motion or wind shear orientation is indicated by the arrow and the quadrants/sides are referred to by the above labels throughout this paper.

In order to capture the true nature of TCs and their intensities a number of criteria are applied to the overpasses within the database. First, estimated winds at the time of overpass must be in excess of 33 kts (tropical storm strength). Additionally a minimum of 50% of the innermost 110 km (1 degree) must be sampled by the sensor for an accurate depiction of the core of the system. Systems undergoing an extratropical transition are removed by imposing a latitude threshold of $\leq 35°$. Finally, land contamination and weakening associated with landfall (and potentially artificial events of RI caused by a system emerging over water after being over land) are removed by limiting the dataset to TCs that are at least 150 km from land at the time of overpass. Table 1 summarizes the characteristics of the final satellite data record after quality control and these thresholds are applied. Throughout the remainder of this thesis when individual basins are examined,

the North Indian and South Atlantic will be excluded from analyses due to their limited sample sizes, however they remain included in the global dataset.

	All Storms		*Rapid Intensification*		*Non-rapid Intensification*	
Basin	*Number of Observations*	*Number of Storms*	*Number of Overpasses*	*Number of Storms*	*Number of Overpasses*	*Number of Storms*
Global	14209	1328	555	234	13654	1321
E. Pacific	2475	256	156	60	2319	256
N. Atlantic	2250	182	75	31	2175	179
N. Indian	320	56	18	10	302	56
S. Atlantic	15	1	0	0	15	1
S. Indian	3029	262	107	50	2922	262
S. Pacific	1455	152	73	25	1382	151
W. Pacific	4665	440	126	58	4539	437

Table 1: Complete dataset statistics. Note that the number of unique storms does not add up exactly due to storms transitioning from one basin to another.

CHAPTER 3

RESULTS

Three focus areas will be examined under the heading of PM observations of TCs: (1) the predictability potential of TC intensity and intensity change from PM observations, (2) observed differences from PM imagery in structure stratified by intensity change, and in particular those undergoing RI compared to the rest of the subset, and (3) the observed evolution of cloud and precipitation features during the RI life cycle.

3.1 - Relationships between PM products and TC intensity

To determine the interplay of brightness temperature parameters and TC intensity and intensity change, linear correlation coefficients (Pearson product-moment coefficient of linear correlation) are evaluated between the miscellaneous statistics and wind speed or its change. This value (r) can be determined between two variables x and y through the following (Wilks, 2006):

$$r_{x,y} = \frac{\frac{1}{n-1}\sum_{i=1}^{n}\left[\left(x_i-\bar{x}\right)\left(y_i-\bar{y}\right)\right]}{\left[\frac{1}{n-1}\sum_{i=1}^{n}\left(x_i-\bar{x}\right)^2\right]^{\frac{1}{2}}\left[\frac{1}{n-1}\sum_{i=1}^{n}\left(y_i-\bar{y}\right)^2\right]^{\frac{1}{2}}}$$

This statistic provides a simple association between two variables but is not robust due to a lack of signal for nonlinear relationships or resistant due to the dependency of the outliers having a strong influence on the mean values in its calculation. Nevertheless, it is computationally simple and provides an easy comparison source between two variables.

Linear correlations between areal means and medians of 85 GHz PCTs and intensity are consistently highest at annuli of 1 and 1.5° than at other distances, with the areal median statistic having slightly higher correlation coefficients than areal means at all hours (Fig. 5). The annuli sizes of 110 and 165 km showing the most skill depict the importance of core processes in the modification of system intensity, while the 55 km annuli seems too small to consistently capture an intensification signal. Slight but noteworthy is the increase in correlation coefficient for means and medians at 110 and 165 km, with the most skillful performer of the medians going from -0.61 and -0.64 (Fig. 5a) and progressing to -0.68 and -0.70 (Fig. 5b) and then -0.72 and -0.72 (Fig. 5c). Only at 24 hours (Fig. 5d) does the skill begin to decrease to -0.71 for each. The delay seen between the observed ice-scattering signature at 85 GHz and the highest correlations hints at the predictive potential that exists, and is likely a byproduct of the lag between latent heat release and resultant TC intensification. The 85 GHz minimum parameter does see an increase in skill over time as well, but consistently performs well worse than the mean and median evaluators.

For more insight, the scatter plot of the strongest of these correlations, 110 km annuli median 85 GHz PCT and 12 hour future intensity is evaluated (Fig. 6). It is seen that more intense TCs are most frequently associated with lower median values, despite a large amount of spread in the data with evidence of a bifurcation in medians from 220-240 K. A possible explanation for outlier storms with low median PCT values and low 12 hour intensities may be landfall, while those with high median PCTs and intensities may have large eye and/or moat values which may bias the medians towards warmer PCTs however more analysis in the future is necessary to determine the exact source. This correlation at 12 hours is superior to that of Cecil and Zipser's (1999) 12-hour intensity and 85 GHz

means over the 1° radius of -0.67 for the EP, NA, and WP basins. It is additionally just shy of Hoshino and Nakazawa's (2007) best correlation of 0.744 between storm intensity (defined as pressure) at time of observation and 10 GHz horizontal brightness temperature minima over the 0-0.5° annuli.

With the strongest correlations consistently seen from the median (50th percentile) to observed intensity, other percentiles are evaluated to determine the importance of spatial coverage of ice-scattering (Fig. 7). At all times and radii these predictors fail to match the skill seen in the median predictor at 85 GHz with higher percentages showing increasingly poor performance. Despite its lack of skill it is noted that the 99th percentile shows improvement at large radii, where it is believed this parameter acts to capture primarily the eyewall convection but is still unreliable due to potential influences from convective cells in the rainbands or other sources.

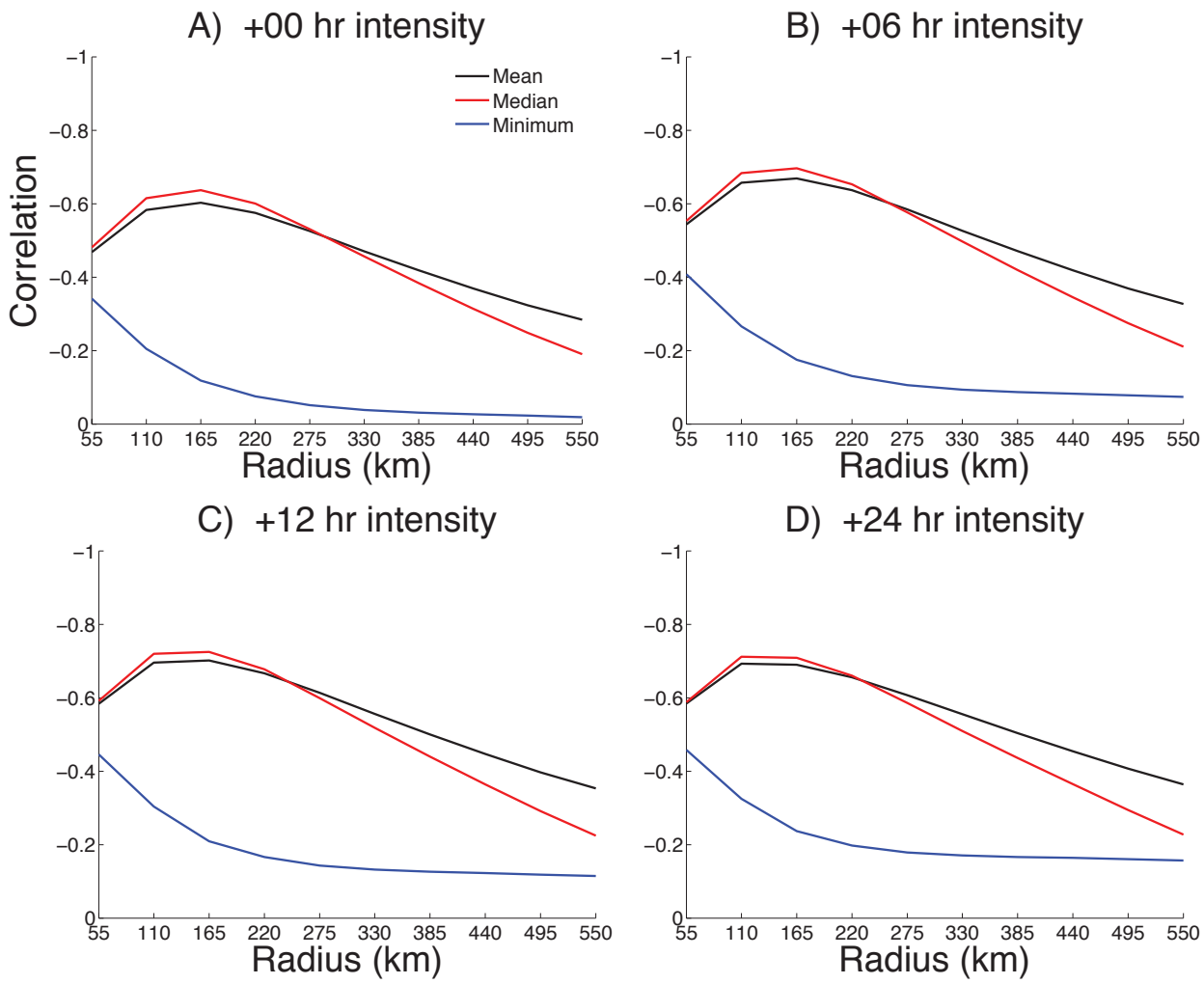

Figure 5: Correlations between 85 GHz PCT metrics and intensity (a) at the time of overpass, (b) 6 hours after, (c) 12 hours after, and (d) 24 hours after for the annuli regions depicted by the radii along the abscissa.

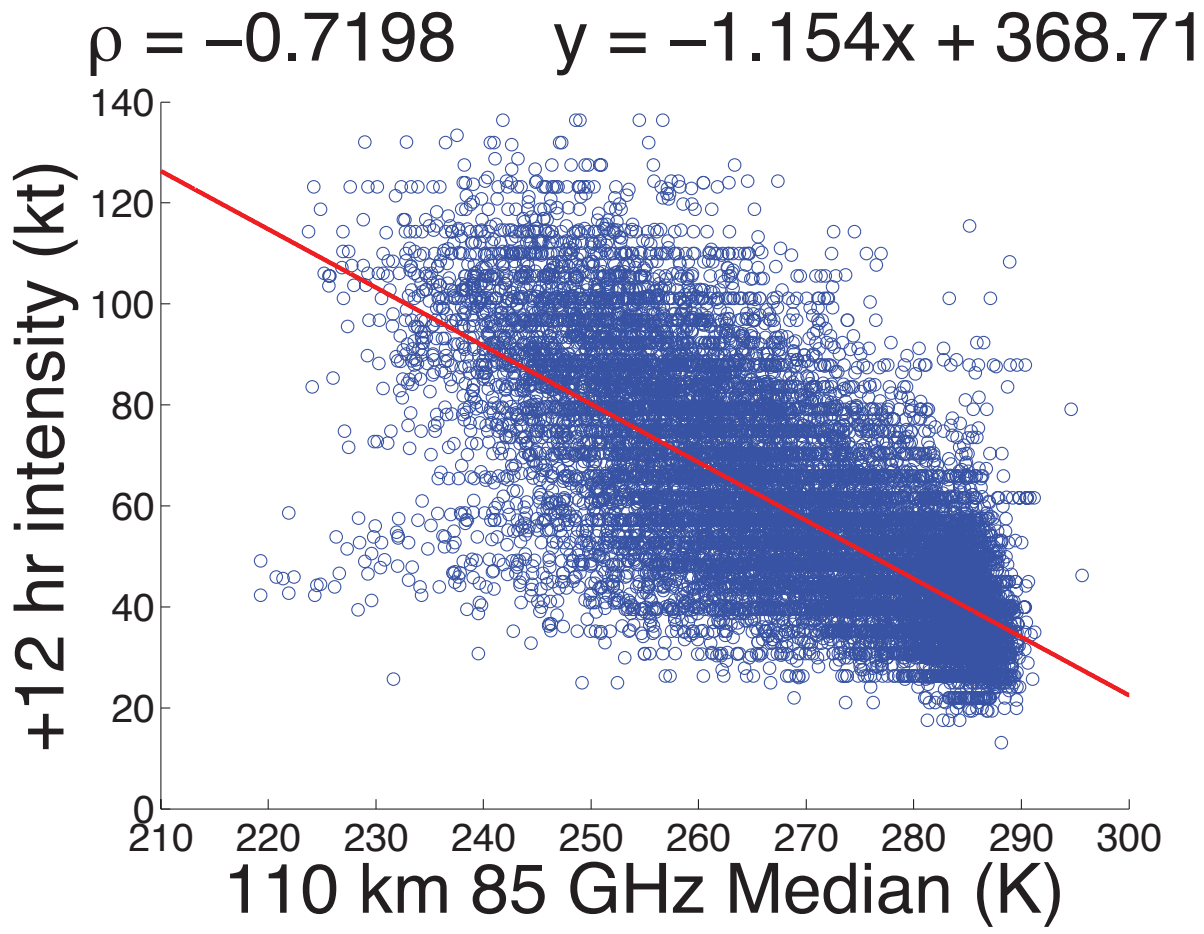

Figure 6: Intensity (kt) 12 hours after the time of SSM/I or TMI observation as a function of 0-110 km radius areal median.

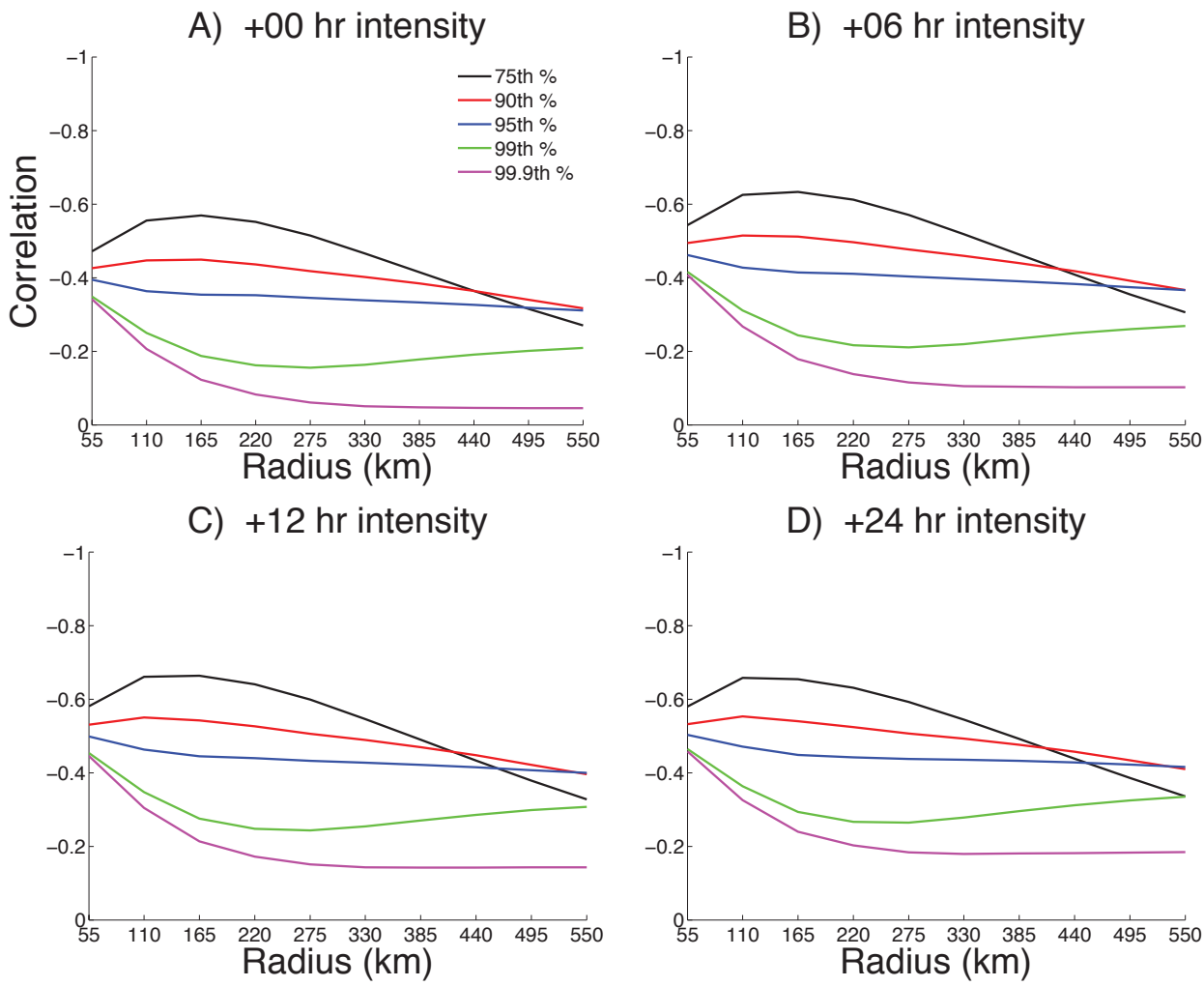

Figure 7: As in Figure 5, except for solely percentage metrics.

Brightness temperature metrics at 37 GHz perform slightly worse than those at 85 GHz (Fig. 8, 9). This is potentially a result of the offsetting influences at 37 GHz of emission by liquid water and scatter by precipitation-sized ice, in addition to the larger native footprint of the lower frequency. Increased skill is seen once more at 6 (Fig. 8b) and 12 hours (Fig. 8c) for the mean and median values at radii extending from 55 to 165 km. Behavior on the whole is extremely similar to that of 85 GHz, albeit slightly less skillful overall.

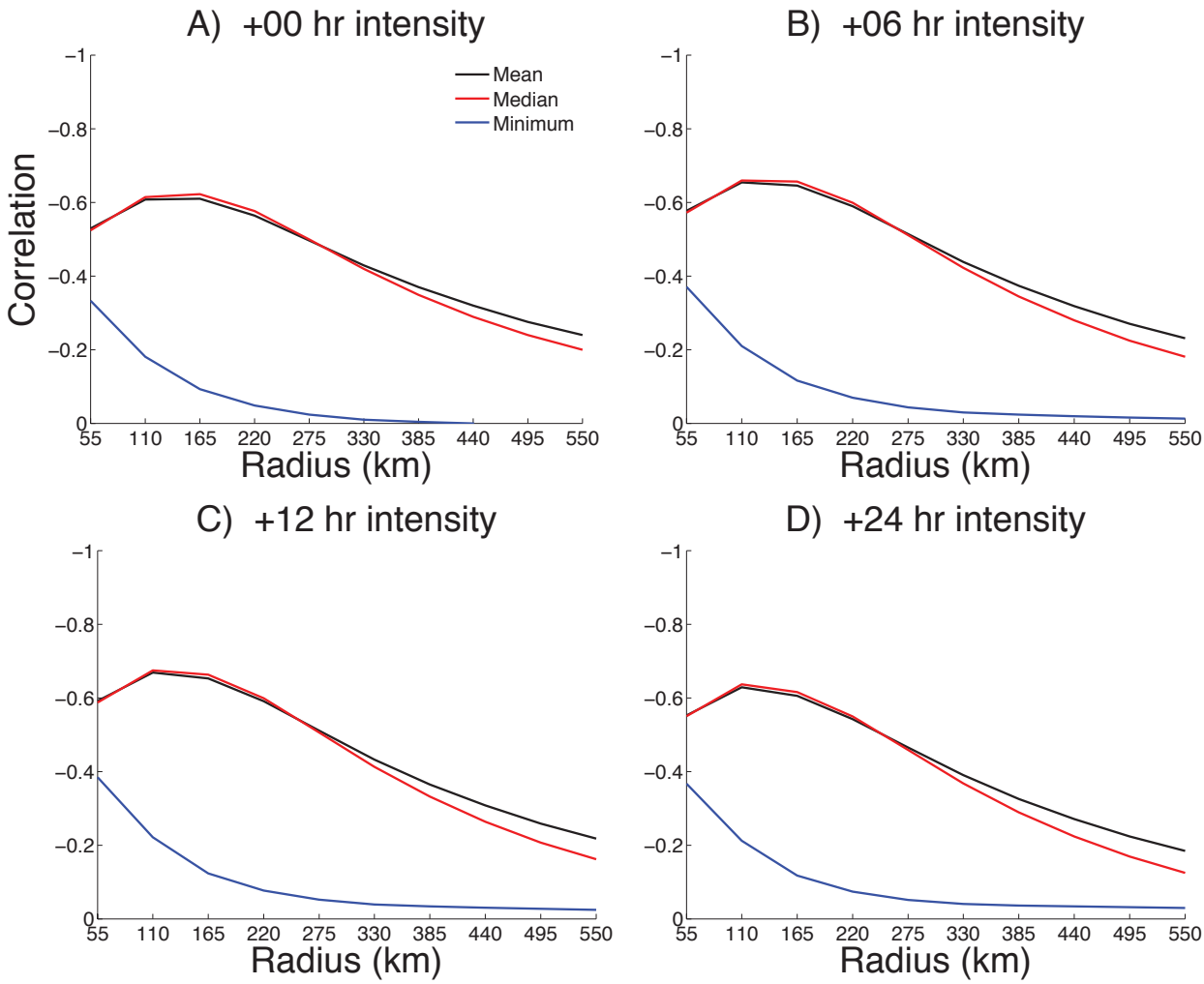

Figure 8: As in Figure 5, except for 37 GHz PCT.

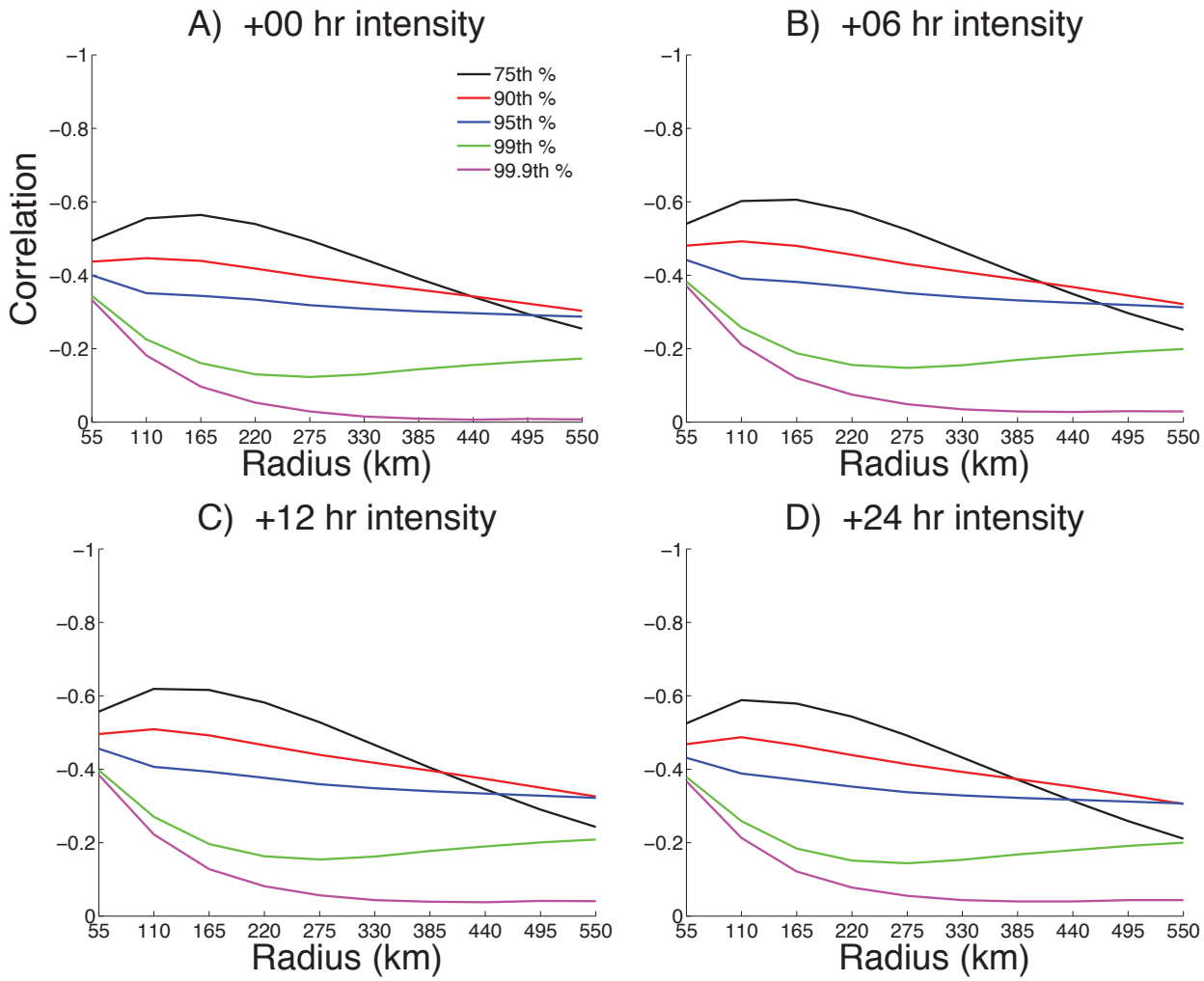

Figure 9: As in Figure 5, except for 37 GHz PCT and solely percentage metrics.

Rain rates show comparable performance to 85 GHz (Fig. 10, 11). The most skillful predictor combination is the 110 km median and 12-hour intensity (Fig. 10b) with a correlation of -0.71. The median rain rate functions show a greater rate of decline at radii $\geq$ 165 km than do the 85 GHz PCT medians (Fig. 5). Once more, measures of isolated convective rain rates prove to show less skill than the 50th percentile metric (Fig. 11).

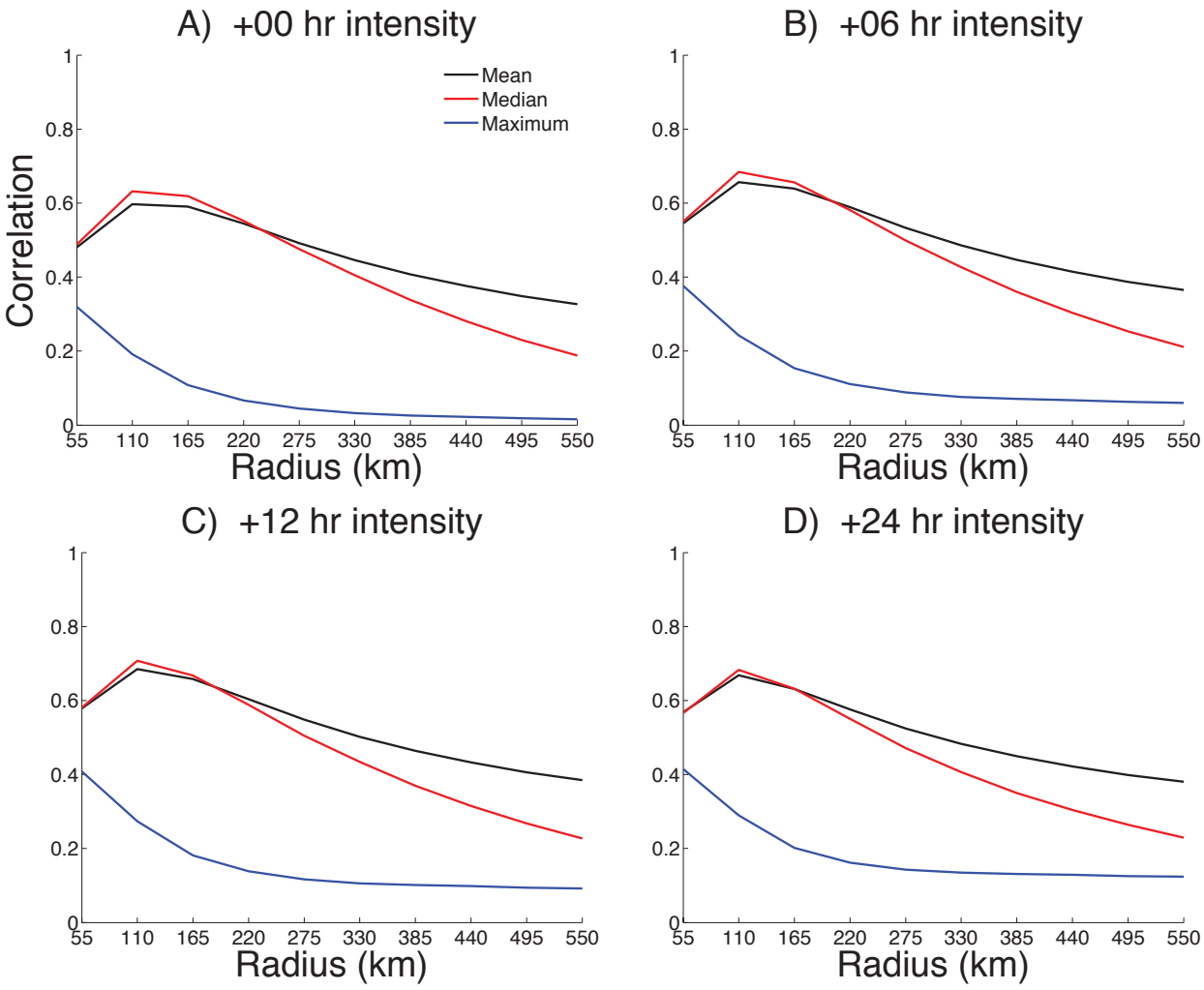

Figure 10: As in Figure 5, except for rain rates.

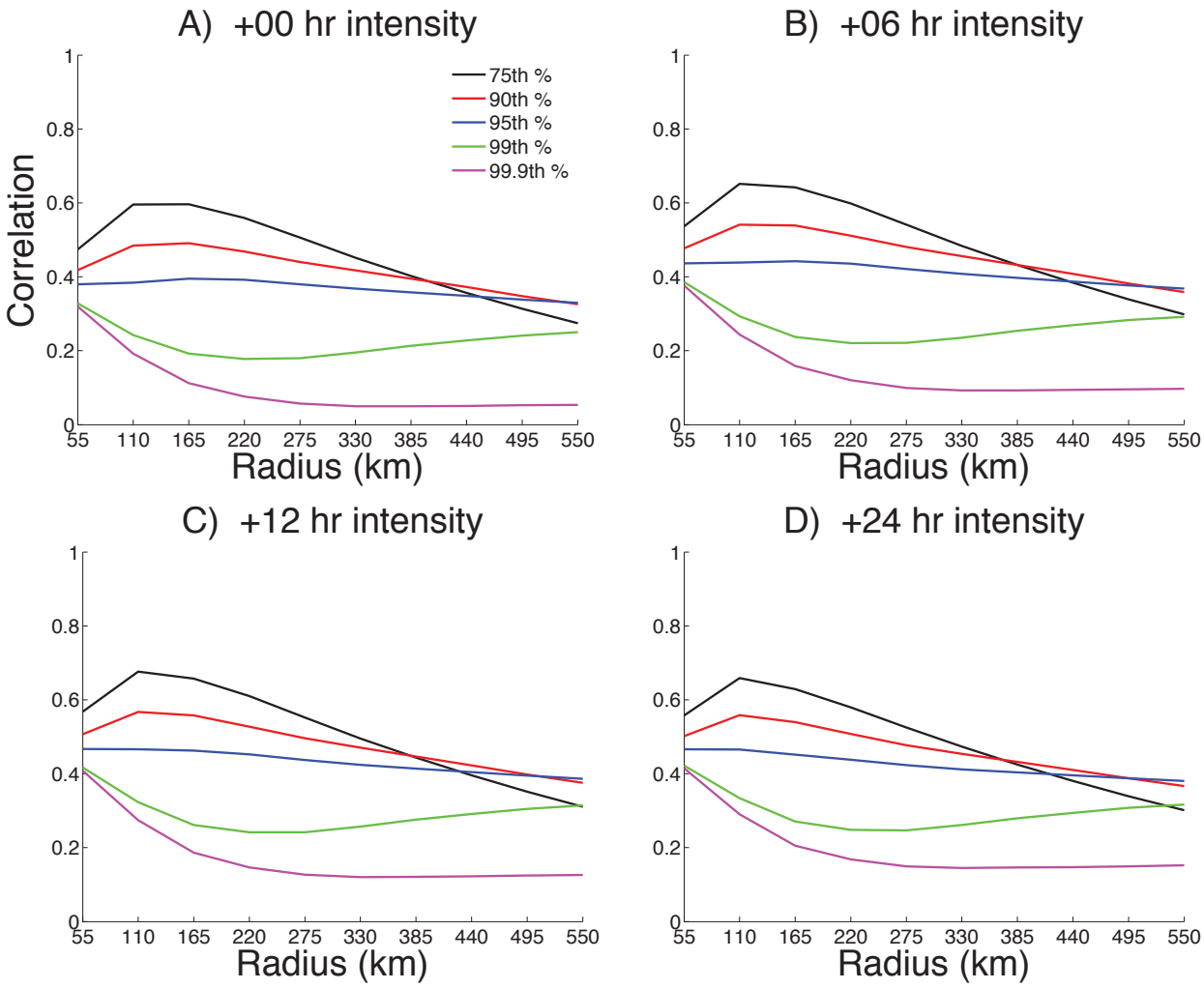

Figure 11: As in Figure 5, except for rain rates and solely percentage metrics.

To evaluate azimuthal influence in addition to variation via basin the top correlation was calculated for every 6-hour period from the time of the overpass out to 36 hours (Table 2) for every possible statistic and azimuthal coordinate combination. The top metrics were typically 85 GHz medians at 110 km for 360° surrounding the storm with the most skillful result of -0.77898 for South Indian 110 km 85 GHz median values at 18 hours following the overpass time. Examination of the scatter plot for these parameters (Fig. 12) yields a similar picture as global 110 km 85 GHz medians (Fig. 6) with a reasonable amount of scatter and a majority of more intense storms possessing lower median brightness

temperatures. The large number of storms with weak winds and high median 85 GHz PCTs is also evident here more so than in Figure 6, although this is largely due to the greater sample size depicted in the global evaluation.

Time	Statistic	Correlation
+00 hours	North Atlantic 165 km rain rate median	0.73710
+06 hours	North Atlantic 165 km 85 GHz median	-0.76064
+12 hours	South Indian 110 km 85 GHz median	-0.77233
+18 hours	South Indian 110 km 85 GHz median	-0.77898
+24 hours	South Indian 110 km 85 GHz median	-0.75962
+30 hours	South Indian 110 km 85 GHz median	-0.71874
+36 hours	South Pacific 110 km storm-relative southern 85 GHz mean	-0.67748

Table 2: Most skillful linear correlations for intensity at the times indicated after the overpass for all available combinations of brightness temperature basin, parameter, statistic, and azimuthal region. The South Atlantic basin is neglected due to its small sample size.

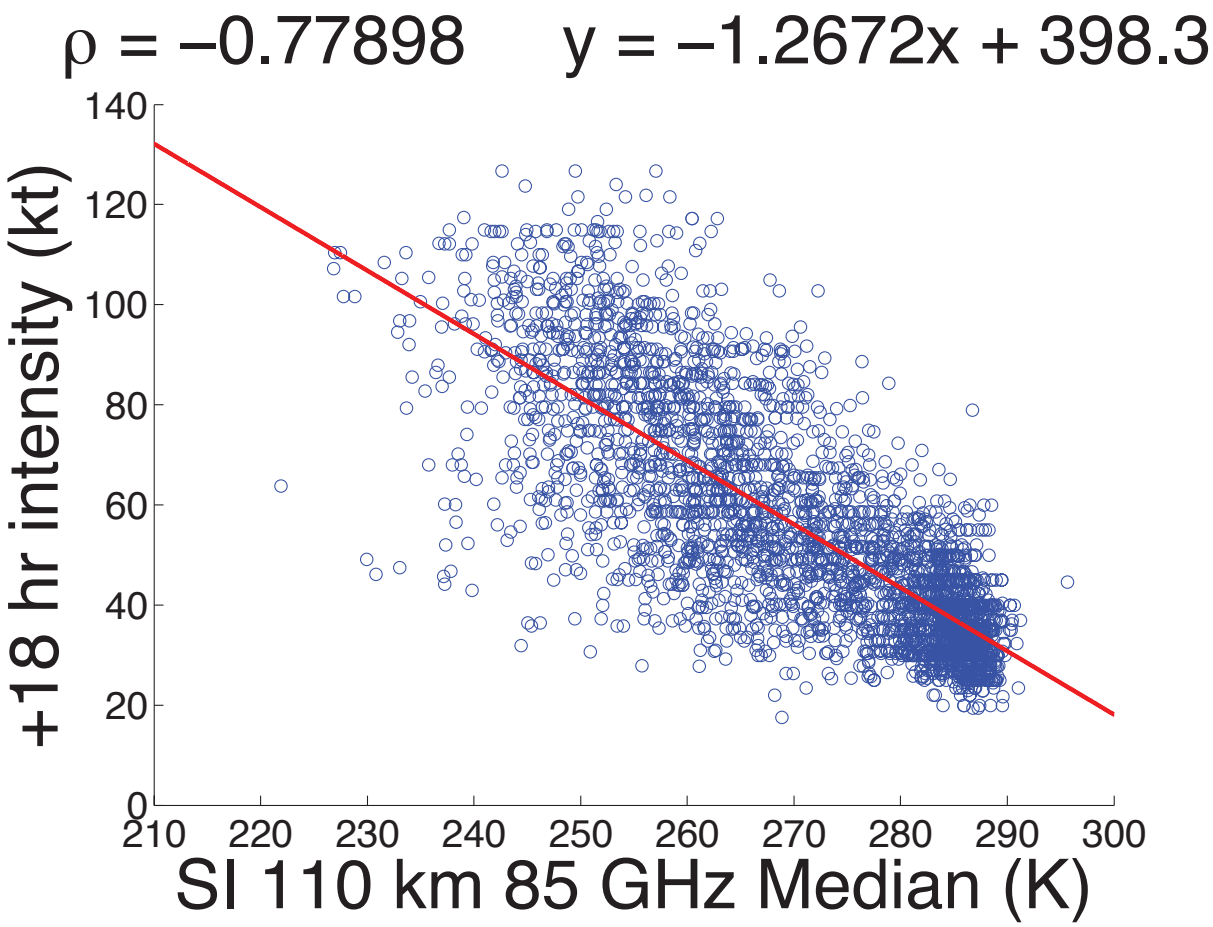

Figure 12: As in Figure 6, except for South Indian basin and intensity 18 hours after the time of overpass.

Correlation with intensity change fares much worse across all brightness temperature parameters, statistics, and annuli (Fig. 13-18). 37 GHz performs especially bad, with a sign change in the correlation coefficient seen for the mean and median values at all time steps for larger radii (Fig. 15). The most skillful statistics once again are 85 GHz means and medians at 110 km annuli for 6 and 12-hour intensity change (Fig. 13a, b). Rain rates and 37 GHz PCT perform worse than the 85 GHz statistics, suggesting the importance of scattering by small cloud ice as well as potential ambiguity introduced from emission.

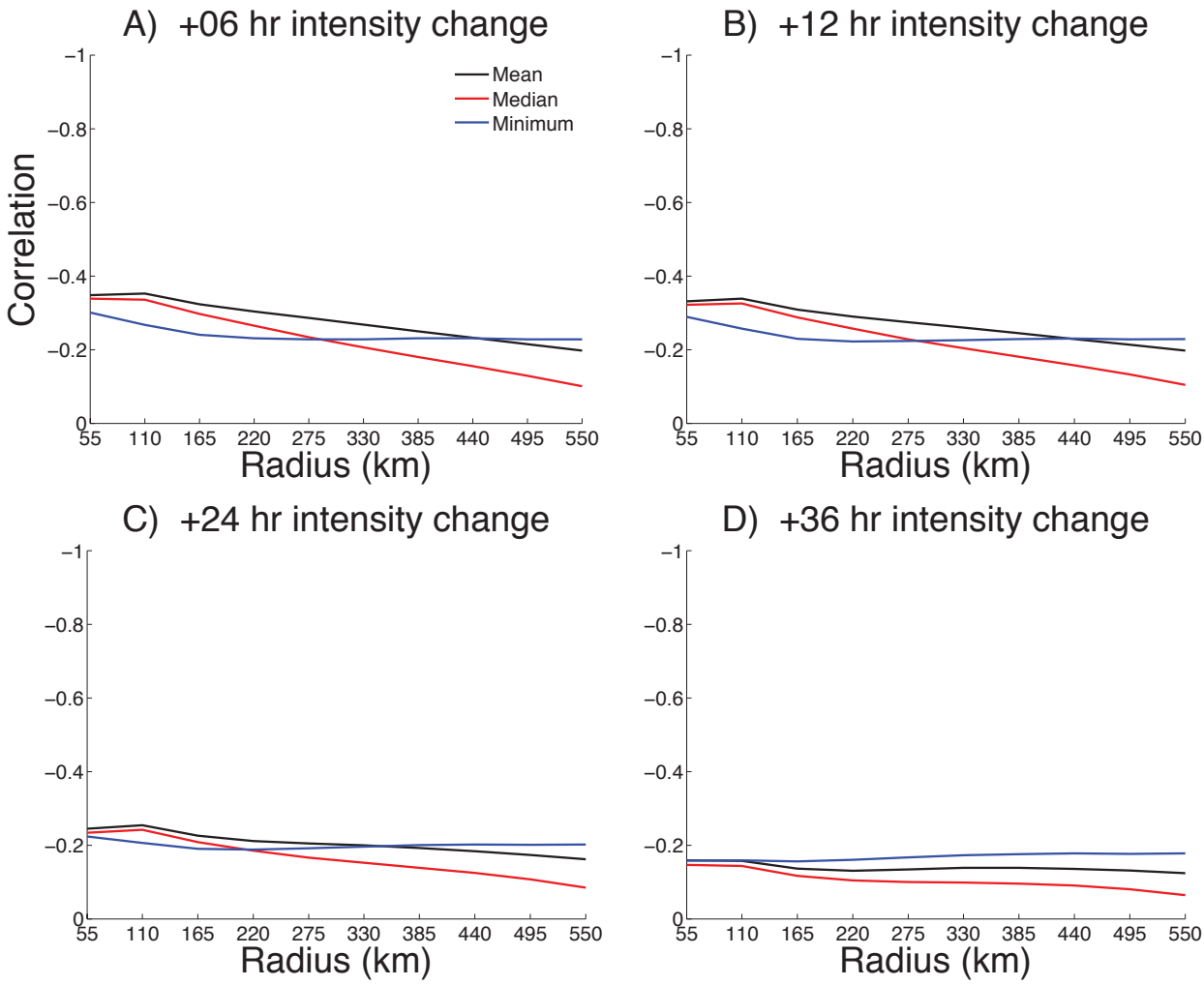

Figure 13: As in Figure 5, except for intensity change.

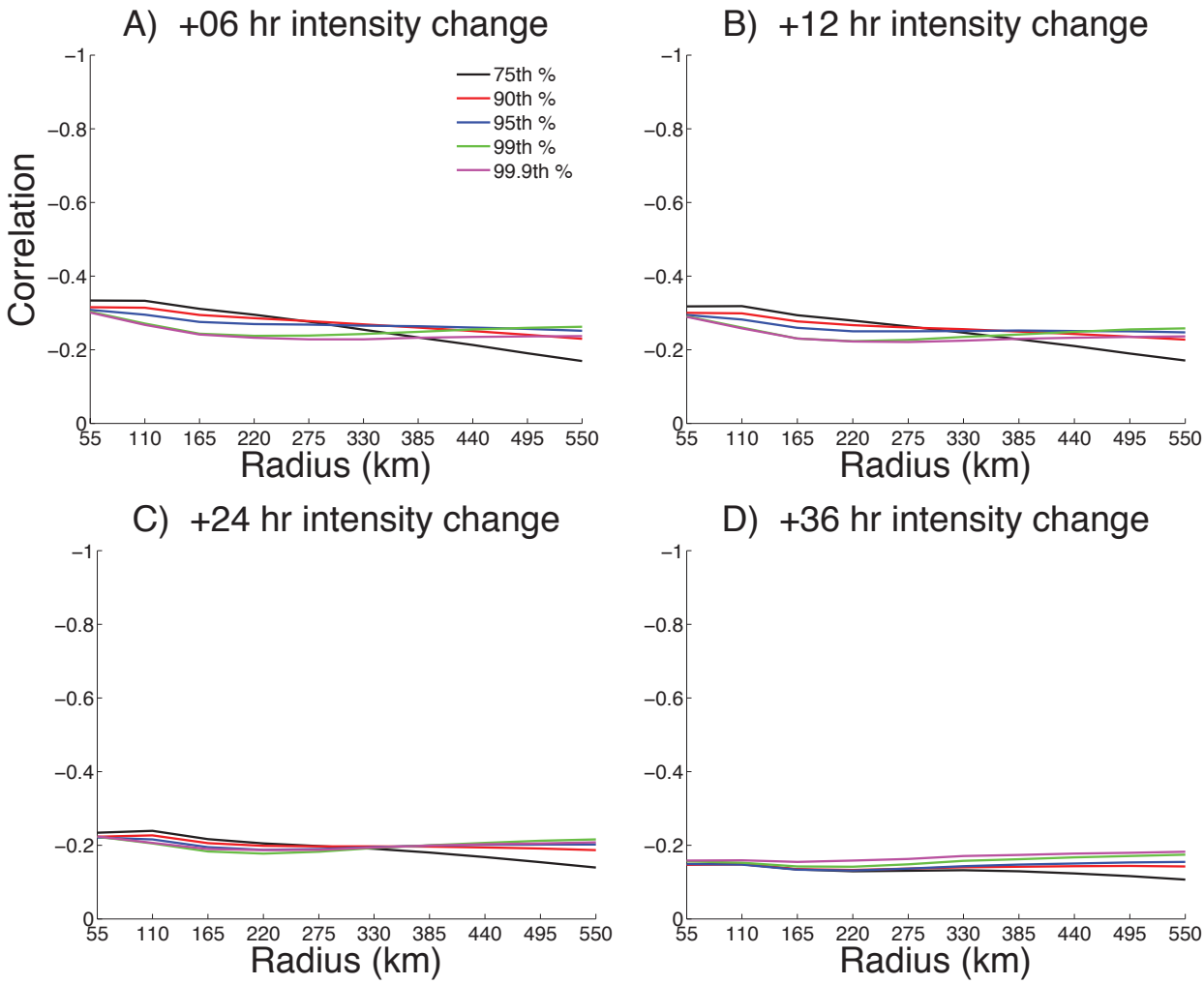

Figure 14: As in Figure 5, except for intensity change and solely percentage metrics.

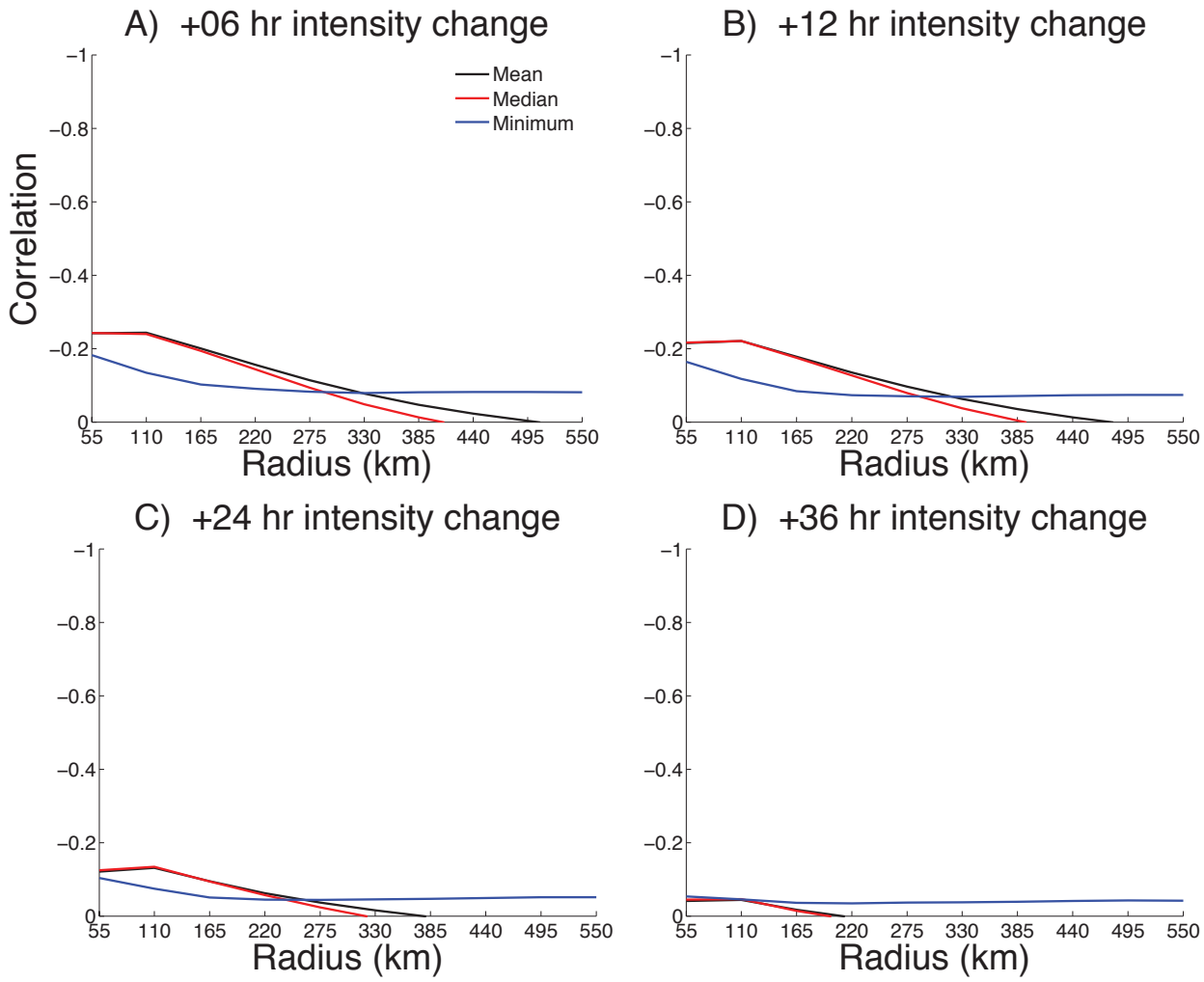

Figure 15: As in Figure 5, except for 37 GHz PCT and intensity change.

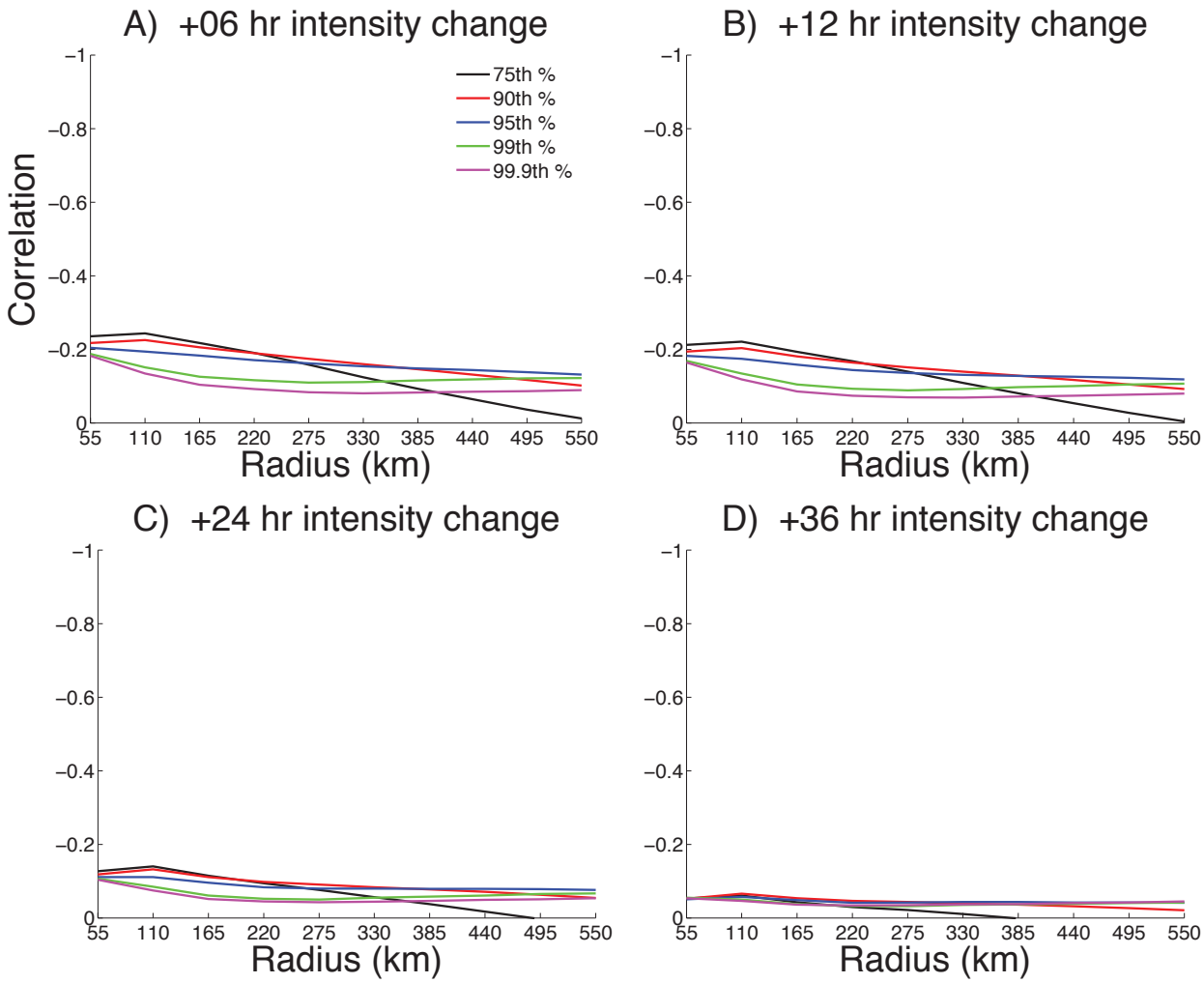

Figure 16: As in Figure 5, except for 37 GHz PCT, intensity change, and solely percentage metrics.

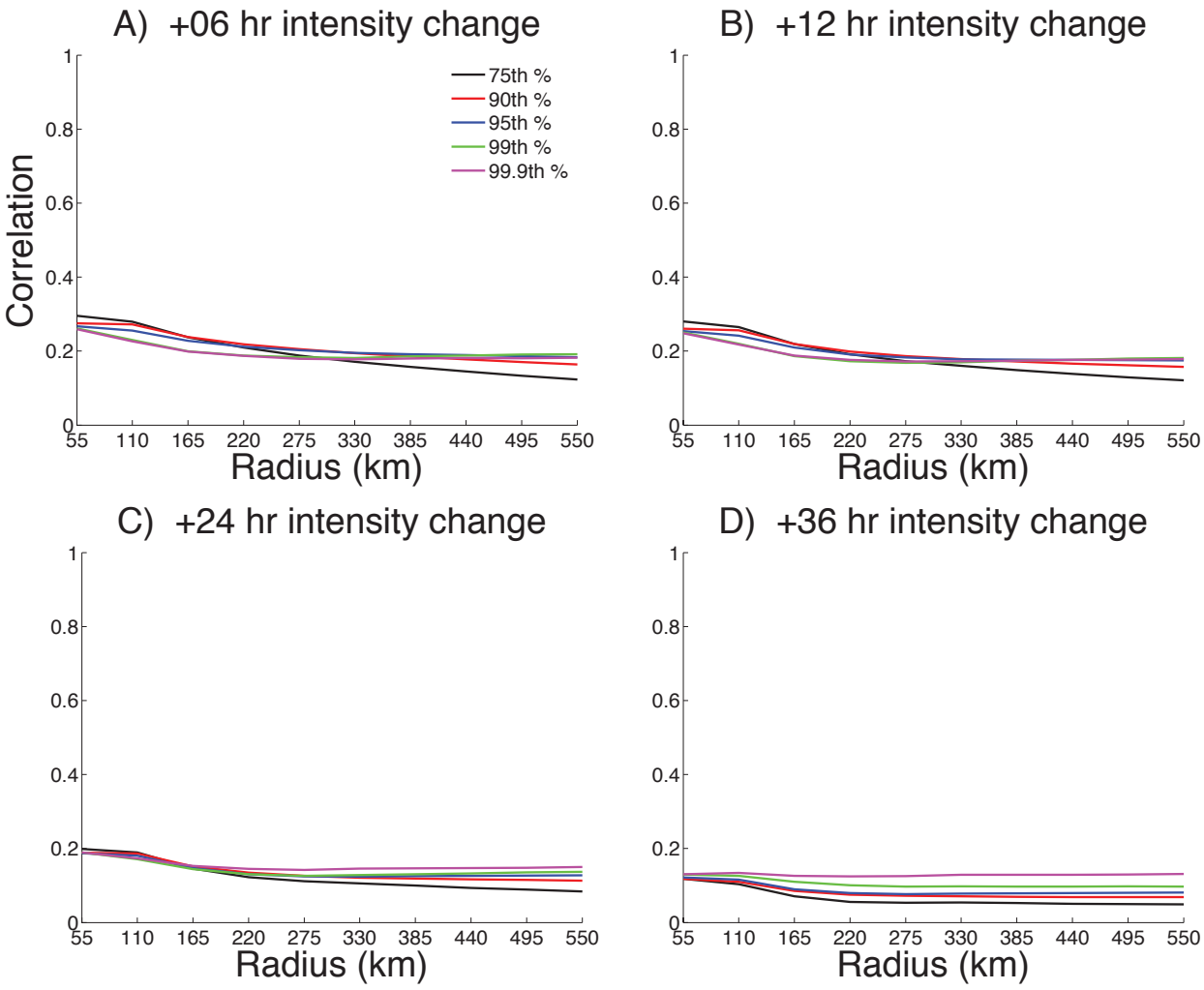

Figure 17: As in Figure 5, except for rain rates and intensity change.

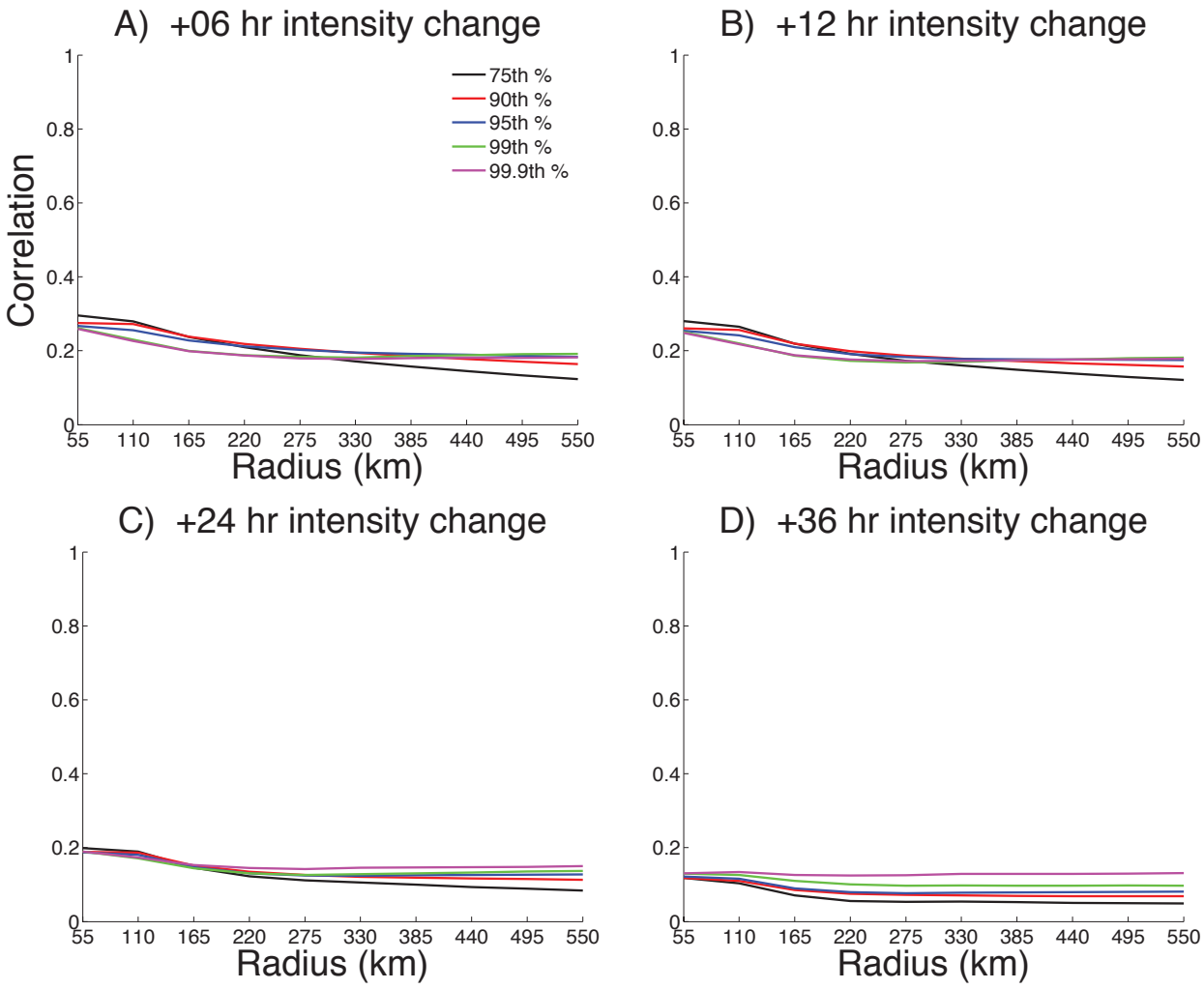

Figure 18: As in Figure 5, except for rain rates, intensity change, and solely percentage metrics.

In evaluating the top correlation via azimuth and basin for each 6 hour period the East Pacific consistently produced the top correlations with the 85 GHz true-north northern half 95th percentile at all times except for 36 hours, which was the same azimuthal orientation except for 90th percentile (Table 3). Each of these correlations is well above the typical correlations seen among other metrics globally at all radii. It is believed that the 95th percentile at large radii may effectively capture the signal of the eyewall convection. Cecil and Zipser (1999) also noted that the highest correlations for intensity change in their data were for the East Pacific basin with their top-performing statistic being

85 GHz minimum brightness temperatures. It must be noted that their sample size is two orders of magnitude smaller for the East Pacific than in this study, which may yield these discrepancies.

ΔTime	Statistic	Correlation
+06 hours	East Pacific 550 km true-north northern 85 GHz 95th percentile	-0.48628
+12 hours	East Pacific 550 km true-north northern 85 GHz 95th percentile	-0.48730
+18 hours	East Pacific 550 km true-north northern 85 GHz 95th percentile	-0.46999
+24 hours	East Pacific 550 km true-north northern 85 GHz 95th percentile	-0.44571
+30 hours	East Pacific 550 km true-north northern 85 GHz 95th percentile	-0.42633
+36 hours	East Pacific 550 km true-north northern 85 GHz 90th percentile	-0.39599

Table 3: As in Table 2, except for intensity change.

Figure 19 examines the relationship between the 85 GHz true-north northern half 95th percentiles for this basin. Evidence of a linear relationship is clearly present, despite the large spread in values. Most of the skill comes from storms that are steady state with moderate ice scattering and weakening storms with low 95th percentile values. The outlier points with wind change values of nearly -100 kts/24 hrs illustrate issues presented by landfall on a metric such as this. Storms undergoing RI over this 24-hour span fare poorly as well, however it does not seem this metric is ideal, as it does not focus solely on the TC core.

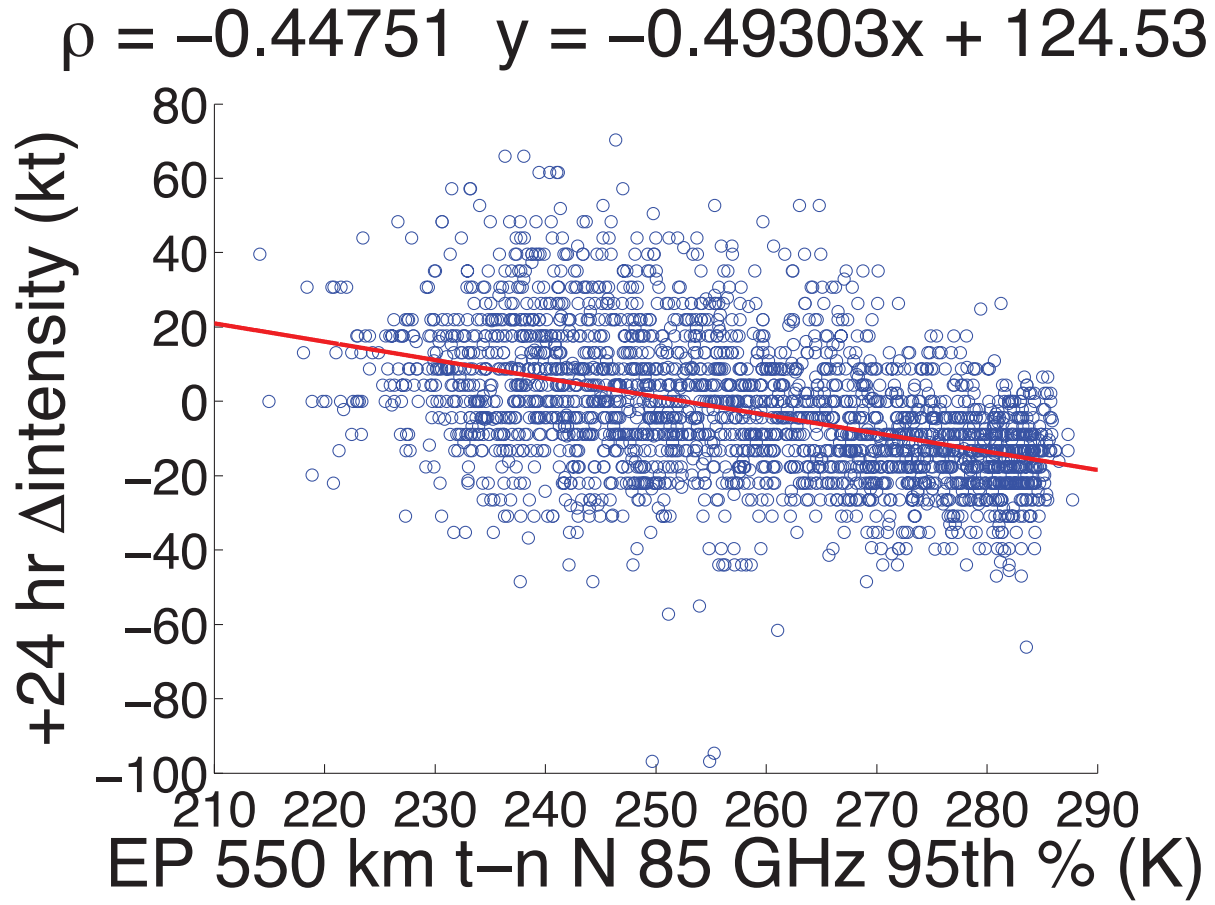

Figure 19: As in Figure 6, except for East Pacific basin true-north northern half 95th percentile 85 GHz PCTs and 24-hour intensity change.

3.2 - TC structural variations by intensity change

Now that the predictive capability of PM data has been demonstrated, evaluation of TC structure can be further evaluated by stratifying results via intensity change classes and seeking the distinguishing factors between them through the distributions of brightness temperature features. Doing this for the various brightness temperature metrics and rain rate estimates reveal primary structural differences between different classes of storms occur near at smaller radii, as a result of the manifestation of core processes. Figure 20 displays an example of this prevalence as at larger radii the probability density functions (PDFs) for TCs undergoing RI, and those that are not, become increasingly similar in

contrast to the two distinct peaks for each class at smaller radii. Accordingly, further evaluation will focus on the innermost regions of 55 and 110 km from the estimated storm center.

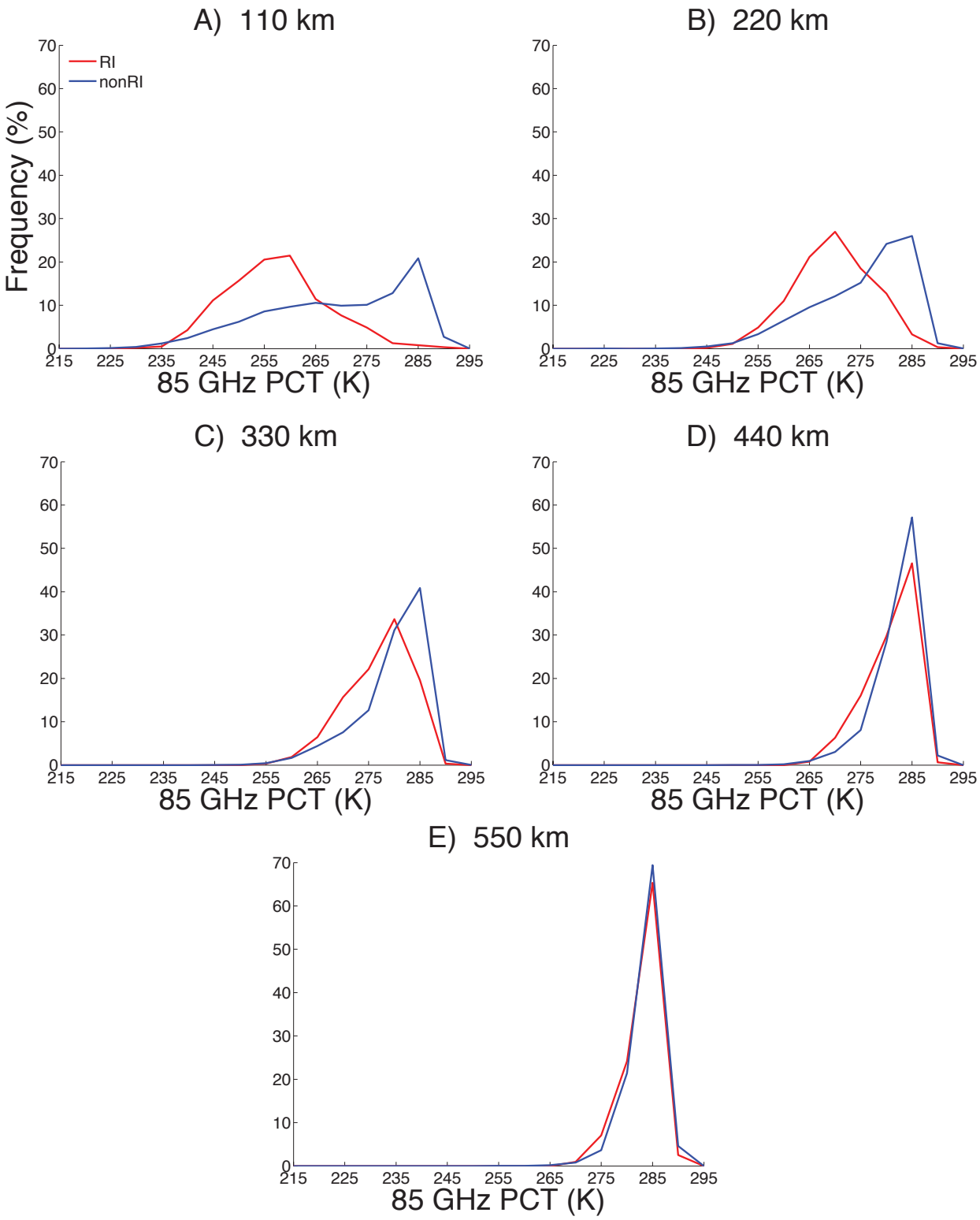

Figure 20: PDFs for 85 GHz PCT median values for the estimated storm center to radii of (a) 110 km, (b) 220 km, (c) 330 km, (d) 440 km, (e) 550 km for all oceanic basins. Bin width is 5 K.

In Figure 21 comparisons between the distributions of mean and median PM values are examined. Noteworthy are these differences, such as the distinct peaks evident in the 85 GHz median PDF (Fig. 21d) for each the RI and nonRI subset, whereas in the 85 GHz mean PDF (Fig. 21a) the RI subset have a distinct peak but the nonRI storms have a rather broad maxima. Similar behavior exists for the rain rate PDFs where the median (Fig. 21f) for nonRI storms is maximized near 0 mm/hr before a sharp decline, whereas the nonRI rain rate means (Fig. 21c) for are relatively broad with a slow decline. Both of these fields, and the increased discrepancies between the RI and nonRI median values compared to the means lend to suggest that areal coverage of PCTs is more critical to storms undergoing RI than mean values, which are easily biased by extreme values.

Also noteworthy is the lack of variance between RI and nonRI storms for the 37 GHz PCTs, as the distributions of the means (Fig. 21b) both peak at 275 K with approximately a 15% difference between the two functions. The 37 GHz medians (Fig. 21e) fare little better, with the maxima between the functions only 1 bin apart with a difference of similar magnitude to that seen with the means. Both of these suggest limited utility and cautious usage of 37 GHz PCT as a predictor of RI due to the minor differences between the two subsets in comparison to the other brightness temperature products examined.

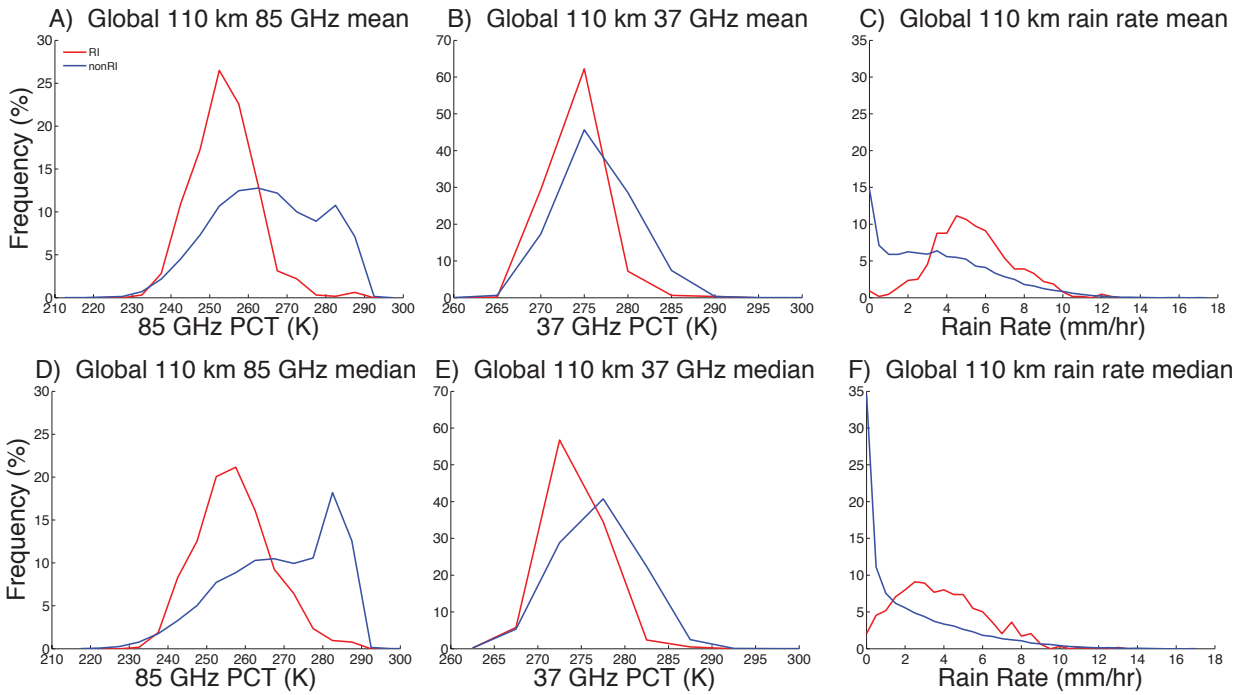

Figure 21: PDFs for global (a) 85 GHz PCT means, (b) 37 GHz PCT means, (c) rain rate means, (d) 85 GHz PCT medians (e) 37 GHz PCT medians, and (f) rain rate medians. Bin width is 5K for PCT fields and ½ mm/hr for rain rates.

In an effort to further examine the influence of extreme PCT and rain rate values, Figure 22a-c displays the 90th percentiles are broken down into PDFs. At a percentage this high only relatively strong convection within the system can have influence on the metric, and any influence of broad features, such as the moat or eye regions is removed. 37 GHz (Fig. 22b) once again shows little ambiguity between storms undergoing RI and those that are not, however 85 GHz and rain rate depict notable differences between the subsets. The lack of distinction between the means and medians is likely the reason that the correlations for each with TC intensity overlap in Figure 8. The 85 GHz PDF (Fig. 22a) yields peaks in both functions at 230K with a much narrower distribution for the RI subset. Noise in the rain rate PDF (Fig. 22c) due to the ½ mm/hr bins makes analysis difficult but the RI function has more pronounced maxima in the values 10-20 mm/hr associated with convective rainfall. Also of note is the propensity of nonRI storms to have extremely low

90th percentile rain rates near 0 mm/hr however these values hardly ever occur for RI systems.

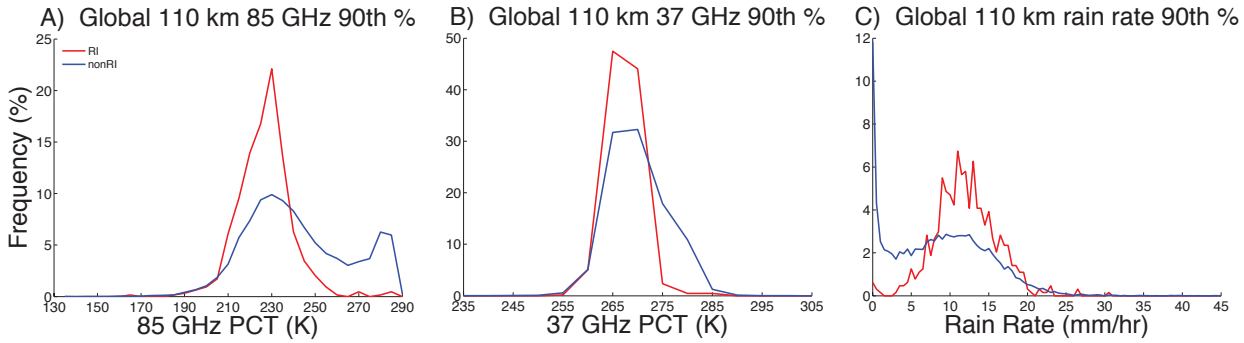

Figure 22: PDFs for global (a) 85 GHz PCT 90th percentiles, (b) 37 GHz PCT 90th percentiles, (c) rain rate 90th percentiles. Bin width is 5K for PCT fields and ½ mm/hr for rain rates.

For one final examination of the importance of extreme convective values on the role of RI initiation PDFs are created for the 99.9th percentile for each field (Fig. 23). This has the dual benefit of depicting the potential role of convective bursts in the occurrence, as well as the spatial importance of convection on the whole. At 85 GHz (Fig. 23a) the RI distributions are shifted slightly towards lower values but of note are that the lowest observed values are mixed between storms undergoing RI and those that do not. RI TCs have nearly twice as high of a frequency however for PCTs between 150-200K than those that are not, suggesting that a small amount of strong convection may persist prior to RI, but rarely on an extreme scale. 37 GHz (Fig. 23b) once more shows little distinction between intensity change classifications. The rain rate function (Fig. 23c) is extremely noisy yet again from the small bin width, with the RI curve shifted slightly higher towards some more intense convective rainfall rates. This lack of distinction between the functions, along with that seen from the 90th percentile functions, seems to indicate a minor role for convective bursts and extreme PCTs/rain rates in the process of rapid intensification

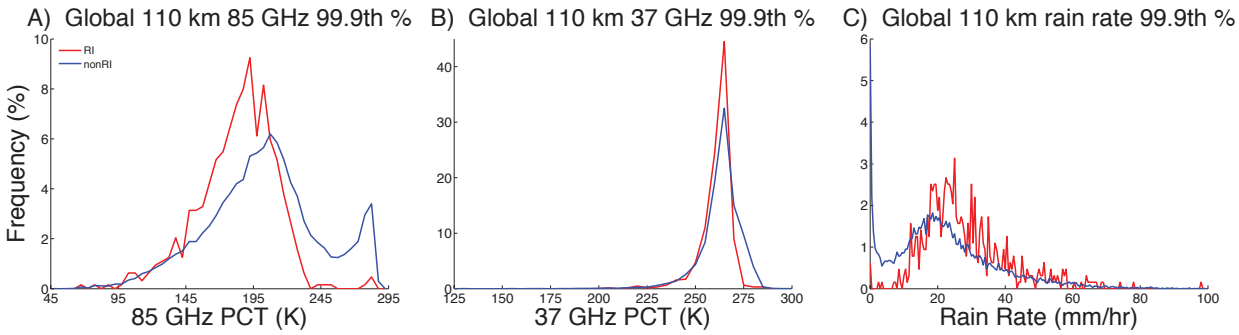

Figure 23: As in Figure 7, except for 99.9th percentiles.

In an effort to further understand the importance of spatial coverage of convection in storms undergoing RI and those that do not the area below specific PCT thresholds at 85 GHz is evaluated (Fig. 24). The threshold for shallow convection is chosen as 250 K (statistically related to reflectivity values of 31-38 dBZ at a height of 2 km from Cecil and Zipser, 2002) with values 220 K and lower denoting moderate convection, similar to the 225 K indicator of deep convection from Cecil and Zipser (1999). For the 0-55 annuli region (Fig. 24a) the moderate convection area shows only a slight contribution to RI storms with a maximum nonzero frequency of around 20% for 10% area below that value and little contribution beyond 45% areal coverage. Storms not undergoing RI show a preference for no moderate convection in the inner ½° with a near 60% frequency of storms falling into the 0% bin. At 110 km (Fig. 24b) this frequency increases to 80%, with little difference in the 220 K functions for each intensity change classification. For area below 250 K the distributions are broad for both classes in the 55 km region (Fig. 24a) but shrink towards low values for each at 110 km (Fig. 24b). The RI subset peaks with a 30% frequency for 10% area below 250 K whereas the nonRI PDF decreases steadily throughout. Less than 10% of the storms undergoing RI have their area fall into the 0% bin, whereas nearly 45% of the nonRI storms do.

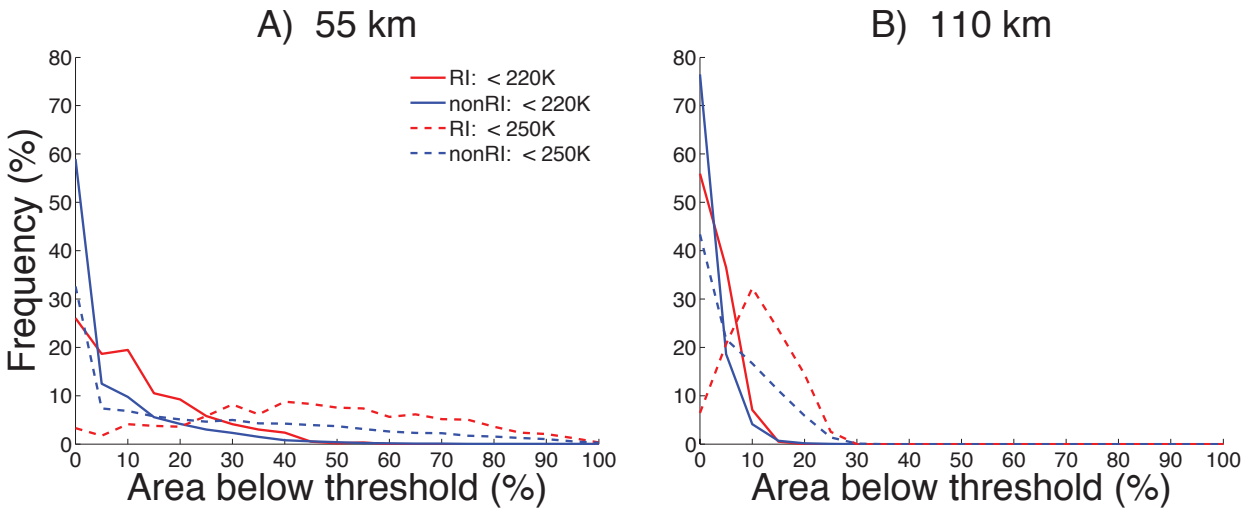

Figure 24: PDFs for global 85 GHz PCT areas below the thresholds listed at (a) 0-55 km and (b) 0-110 km. Bin width is 5%.

With the distinctions between the areal coverage becoming apparent, in addition to the lack of influence of more extreme convective values, the median values of Figure 10d-f nonRI subset are broken down into intensifying (IN), steady state (SS), and weakening (WE) classifications described earlier for Figure 25. Of note: in each of these PDFs is the near identical nature of the distributions for TCs that are of a steady state nature or weakening. Recalling Figure 21, the nonRI distributions also appear similar to these two, seemingly due to the large contribution of these two classes to the combined nonRI classification. A distinct signal persists however of storms which are intensifying and undergoing RI. At 85 GHz (Fig. 25a) the intensifying PDF has a Gaussian appearance with a maximum of 15% near 260 K. The storms that are intensifying have rain rates slightly less frequent intense values than those that are undergoing RI. At 37 GHz (Fig. 25b) once more there is little separation between the classes, with the intensifying function straddling the RI and near identical steady state and weakening functions.

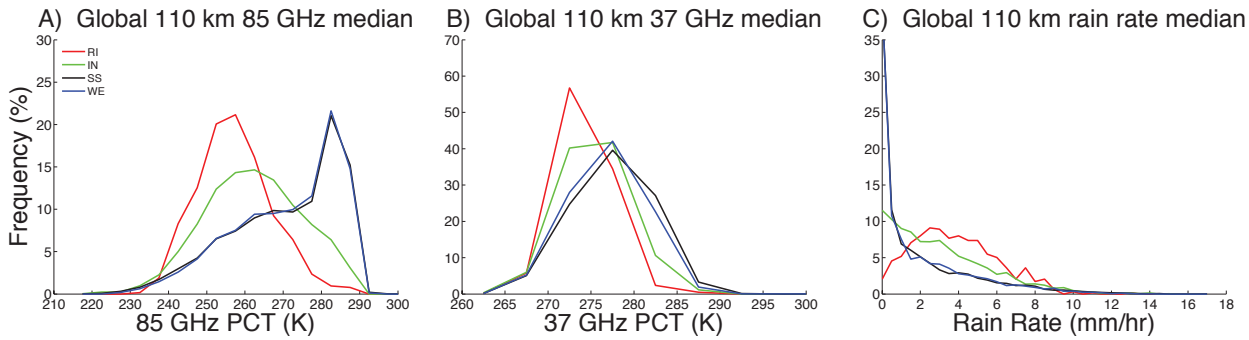

Figure 25: As in Figure 6d-f, except for nonRI broke down into intensifying (IN), steady state (SS), and weakening (WE).

Figures 26-29 further delineate the variations seen in the 85 GHz PCT and rain rate median fields by azimuth via a quadrant analysis in the storm-relative and shear-relative coordinate systems. At small annuli the RI systems have average medians on the order of 10-25 K below the nonRI systems, with the differences becoming smaller as radius increases. In the storm-relative coordinates RI systems for all northern hemisphere basins exhibit the most depressed 85 GHz PCTs near the system core to the right of the storm motion (Fig. 26b, d, f), with this signal also evident in the global data (Fig. 26a). Generally the RI observations cluster together, with the exceptions being for the East Pacific (Fig. 26b) with strongest ice scattering taking place to the right of storm motion and South Indian (Fig. 26c) with it occurring towards the front portion of the storm. North Atlantic storms have lower average 110 km median 85 GHz PCT values (Fig. 25d) than the other oceanic basins, which may be a byproduct of the direct aircraft observations taking place in that basin versus largely Dvorak satellite-based analyses elsewhere. Overall the greatest discrepancy between RI and nonRI is seen in the South Pacific with differences from 25-30 K seen at 55 and 110 km between the subsets.

Rain rate average median values (Fig. 27) provides similar information to that of the ice scattering data, underscoring the influence of active convective processes (as indicated

by enhanced ice scattering signatures) in the variation between storms experiencing RI and those that are not. Once more the North Atlantic (Fig. 26d) basin produced a weaker signal for RI storms, with quadrant rain rates at 55 km between 4 and 5 mm/hr and at 110 km. The South Pacific (Fig. 27e) also sees the largest difference between RI and nonRI systems yet again.

For a shear-relative coordinate system additional differences become apparent for the average median by radius analysis. RI storms in the southern hemisphere exhibit the lowest 85 GHz median values downshear at small radii (Fig. 28c, e). For RI systems the northern hemisphere basins (Fig. 28b, d, f) average medians are more tightly clustered at all radii than the southern hemisphere (Fig. 28a, c, e) or the storm-relative versions (Fig. 26b, d, f). Global quadrant shear-relative average median rain rates (Fig. 25) for RI systems are consistently twice the magnitude at 55 and 110 km than the nonRI values, again illustrating the disparity in precipitation intensity of storms which undergo RI and those that do not.

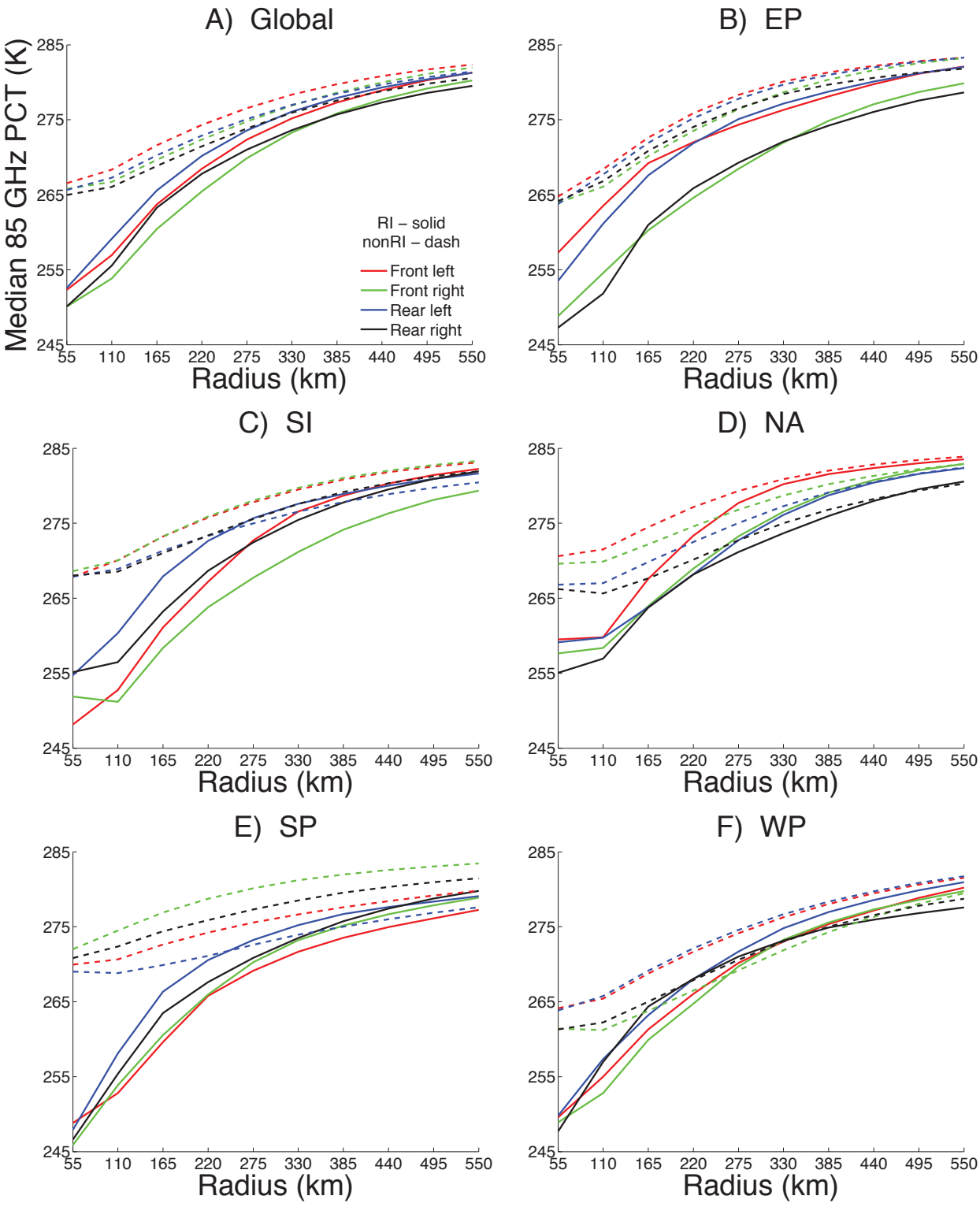

Figure 26: 85 GHz PCT medians via storm-relative motion quadrant for (a) all oceanic basins (b) East Pacific (c) South Indian (d) North Atlantic (e) South Pacific (f) West Pacific.

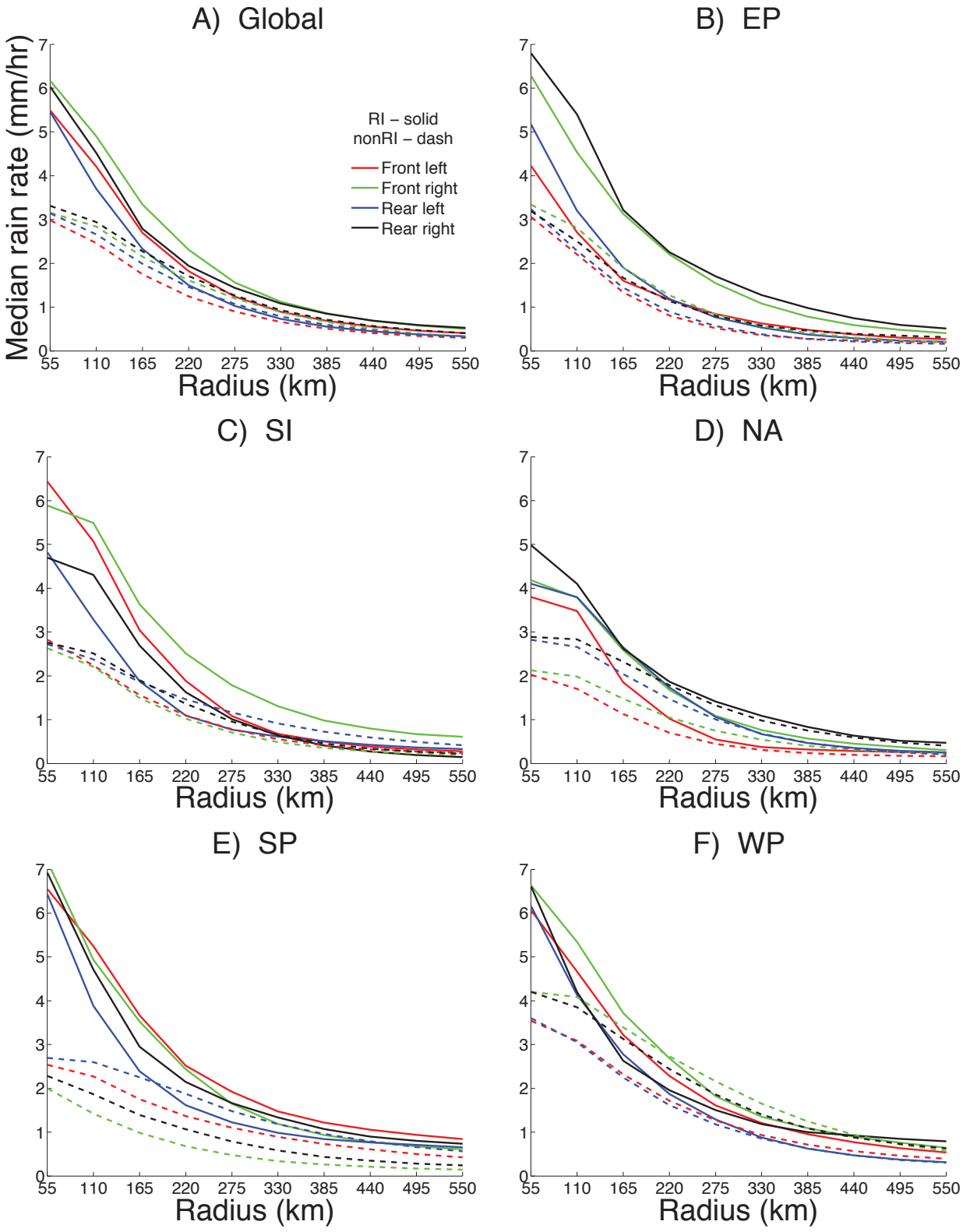

Figure 27: As in Figure 26, except for rain rates.

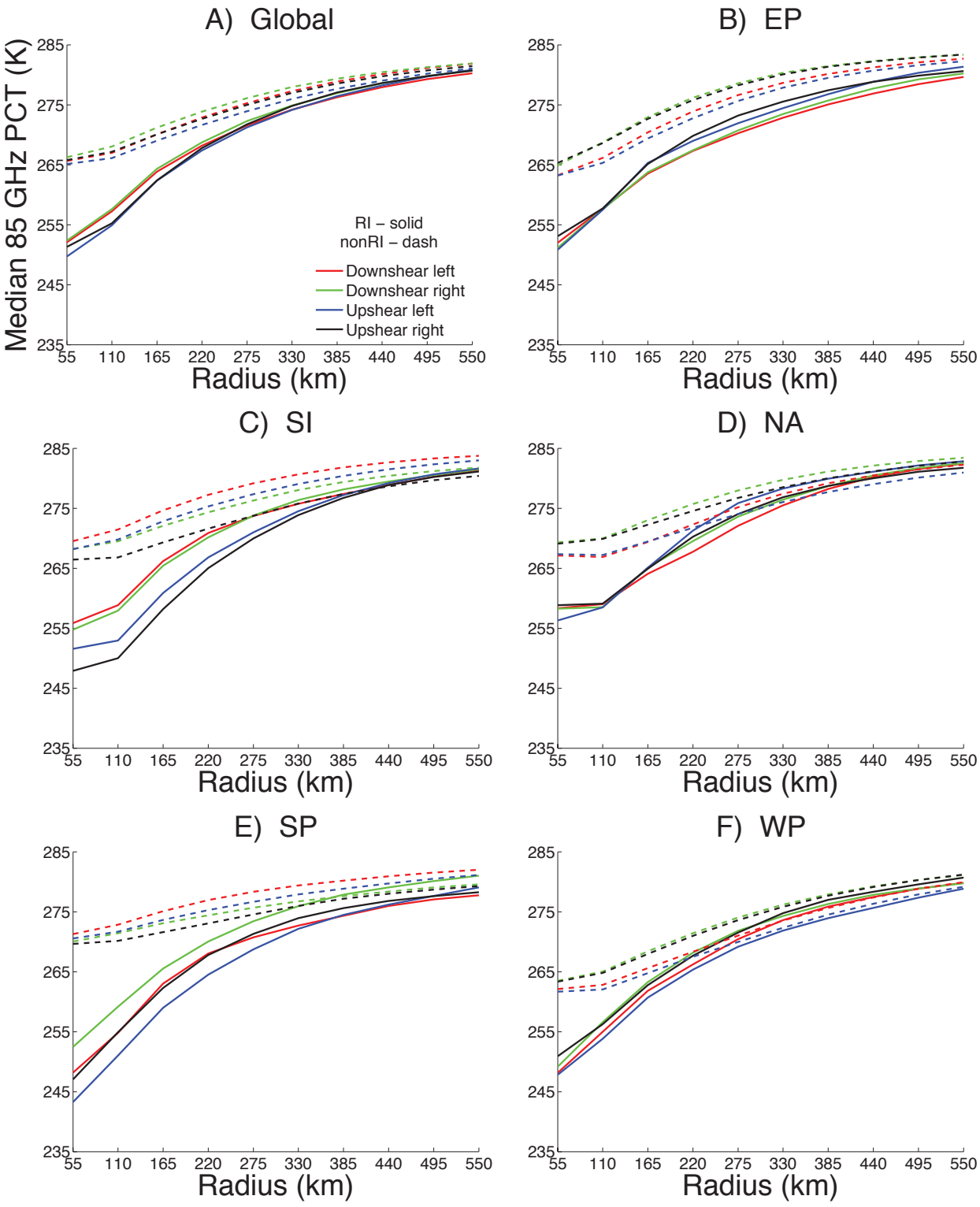

Figure 28: As in Figure 26, except for shear-relative coordinate system

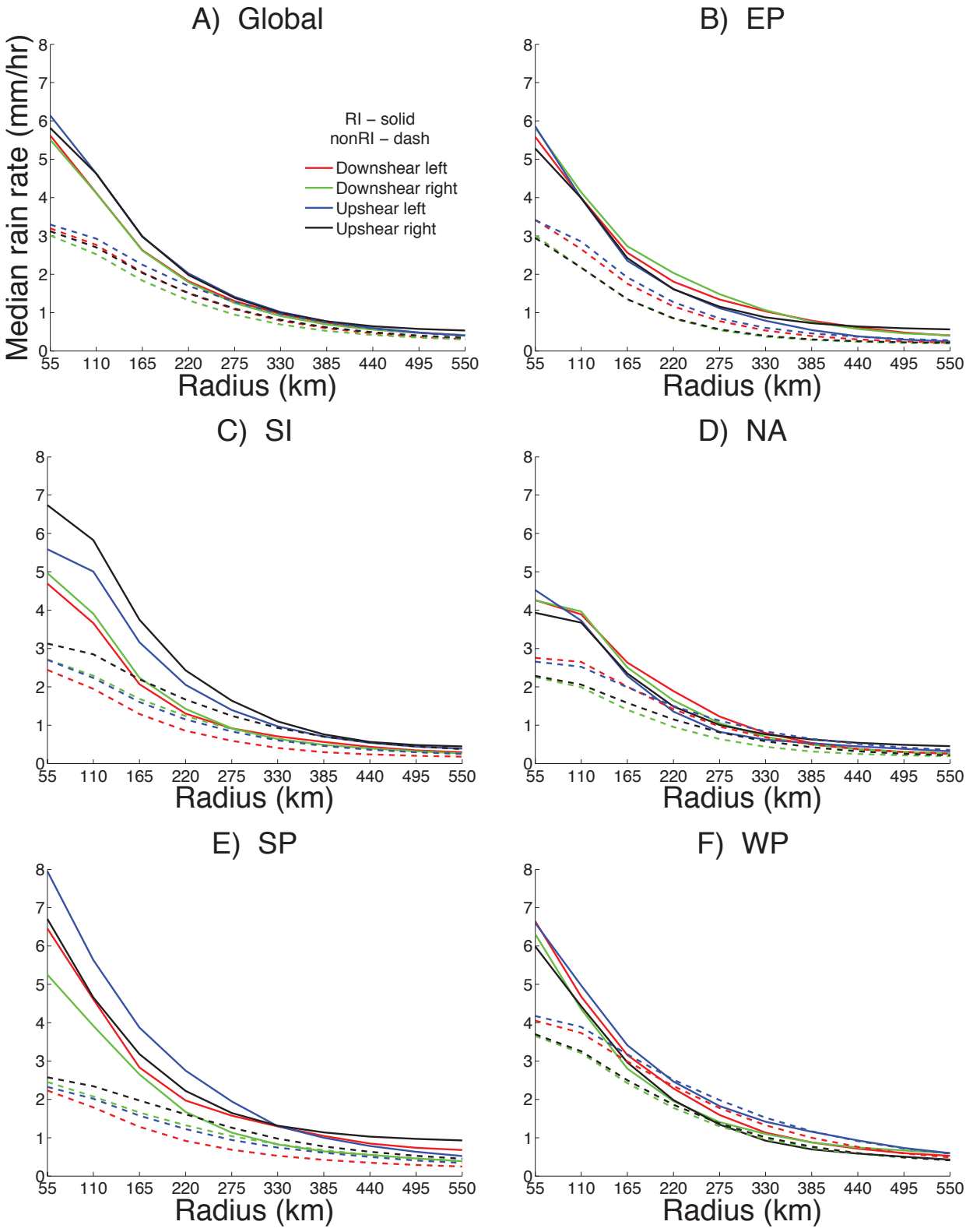

Figure 29: As in Figure 26, except for shear-relative coordinate system rain rates.

Axisymmetric interpolations back to the native data resolution of 8 km were performed linearly on the data for RI and nonRI storms to determine any radial variation in location of structural features or their intensities (Fig. 30). Globally RI systems have an axisymmetric minimum 85 GHz PCT near 50 km from the system core of 266 K, while those not undergoing it have a brightness temperature of 271 K which also happens to be the minimum value for those systems (Fig. 30a). Rain rates also peak at this distance, with a value of 2.75 mm/hr for RI systems and 1.75 for nonRI storms. The 37 GHz data is ambiguous with minimal difference seen between the RI and nonRI systems.

For individual basins the axisymmetric features show a great deal of variation. The North Atlantic (Fig. 30d) is the most ambiguous basin, with the weakest characteristics of all basins for RI storms with a minimum 85 GHz PCT and maximum rain rate of 270 K and 2.25 mm/hr respectively, opposed to 272 and 1.75 mm/hr for nonRI systems. The source of this variation in relation to the other basins is believed to be the impact of direct aircraft observation on intensity classifications. Each of the other basins however shows a clear distinction in precipitation rates and 85 GHz brightness temperatures at radii 150 km and below between the two storm classifications. Behavior at 37 GHz is erratic, as for the East Pacific (Fig. 30b) RI storms have depressed temperatures throughout compared to those not undergoing RI, while in the North Atlantic the RI system brightness temperatures are higher throughout the entire profile compared to the nonRI systems. In the other basins the 37 GHz effects switch dominance at radii between 100 and 250 km of the storm center. The South Indian ocean (Fig. 30d) contains the strongest axisymmetric rain rate (3.5 mm/hr) and coldest 85 GHz brightness temperature (264 K) of any basin, at 40 km from the estimated center. Loosely defined as the region with elevated rain rates and depressed

85 GHz brightness temperatures, the eyewall's signal is typically evident from around 25 km out through 100 km as RI takes place.

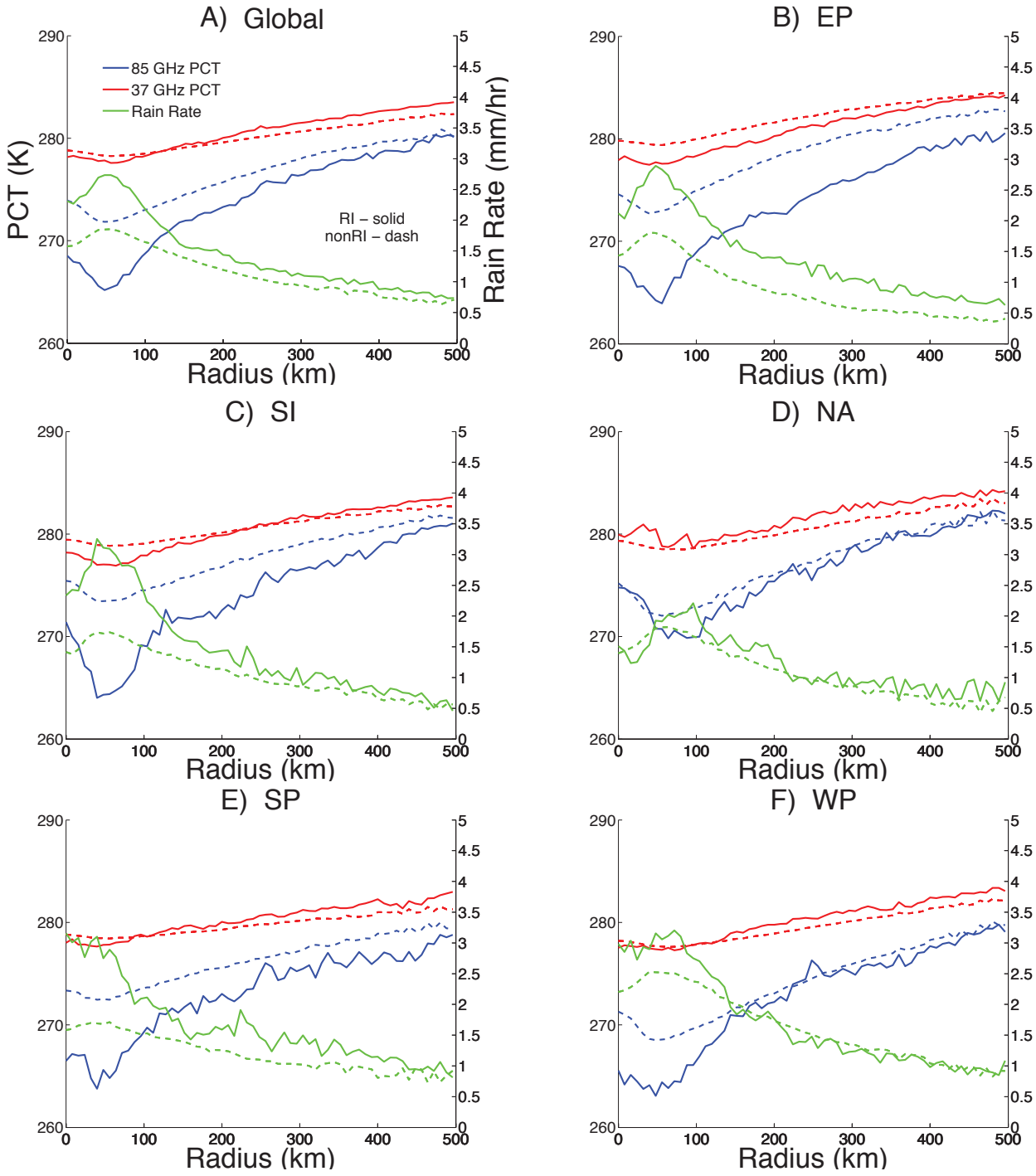

Figure 30: Axisymmetric interpolations at 8 km resolution for (a) all basins (b) East Pacific, (c) South Indian (d) North Atlantic, (e) South Pacific, and (f) West Pacific.

3.3 - Evolution of TC structure during RI

With the focus throughout being on storms undergoing rapid intensification, it is natural to evaluate the structural evolution to determine what changes take place during the 24-hour window used here for RI. The basis for much of this section lies in composite plan view plots constructed by rotating the gridded satellite data by either storm motion or wind shear orientation and averaging the net product of each of the overpasses added together. As a result of the rotation the grids do not align perfectly on all occasions, and accordingly at times two grid points may be interpolated into one in the composite development, however the averaging algorithm compensates for this issue.

Figure 31 and 32 present global 85 GHz PCT composites for each of the intensity change definitions in the database in a storm-relative motion and shear-relative coordinate systems respectively. As expected, ice-scatter is most intense in storms beginning to undergo RI with decreasing scatter as intensity change values decline for each coordinate system. A ring feature is evident at a radius of around 55 km in each plot, likely depicting the developing eyewall in RI and intensifying storms, and the decaying eyewall in weakening systems. The minimum value associated with the eyewall in the storm-relative RI composite (Fig. 31b) is 241 K and located in a region of depressed PCTs to the right of storm motion at this stage. This region of most intense ice scatter lessens with decreasing intensity change and rotates counterclockwise around the system, being situated to the rear of storm motion as weakening phases ensue (Fig. 31d).

The shear-relative plots portray a similar picture at 85 GHz (Fig. 32). The minimum PCT region shifts from upshear at RI inception (Fig. 32a) and rotates to the right of the shear vector prior to the intensifying phase (Fig. 32b). The steady state (Fig. 32c) and

weakening (Fig. 32d) plots are nearly indistinguishable in this coordinate system. Yet again a ring-like structure is evident across all intensity change composites and is most pronounced for storms beginning RI (Fig. 32a).

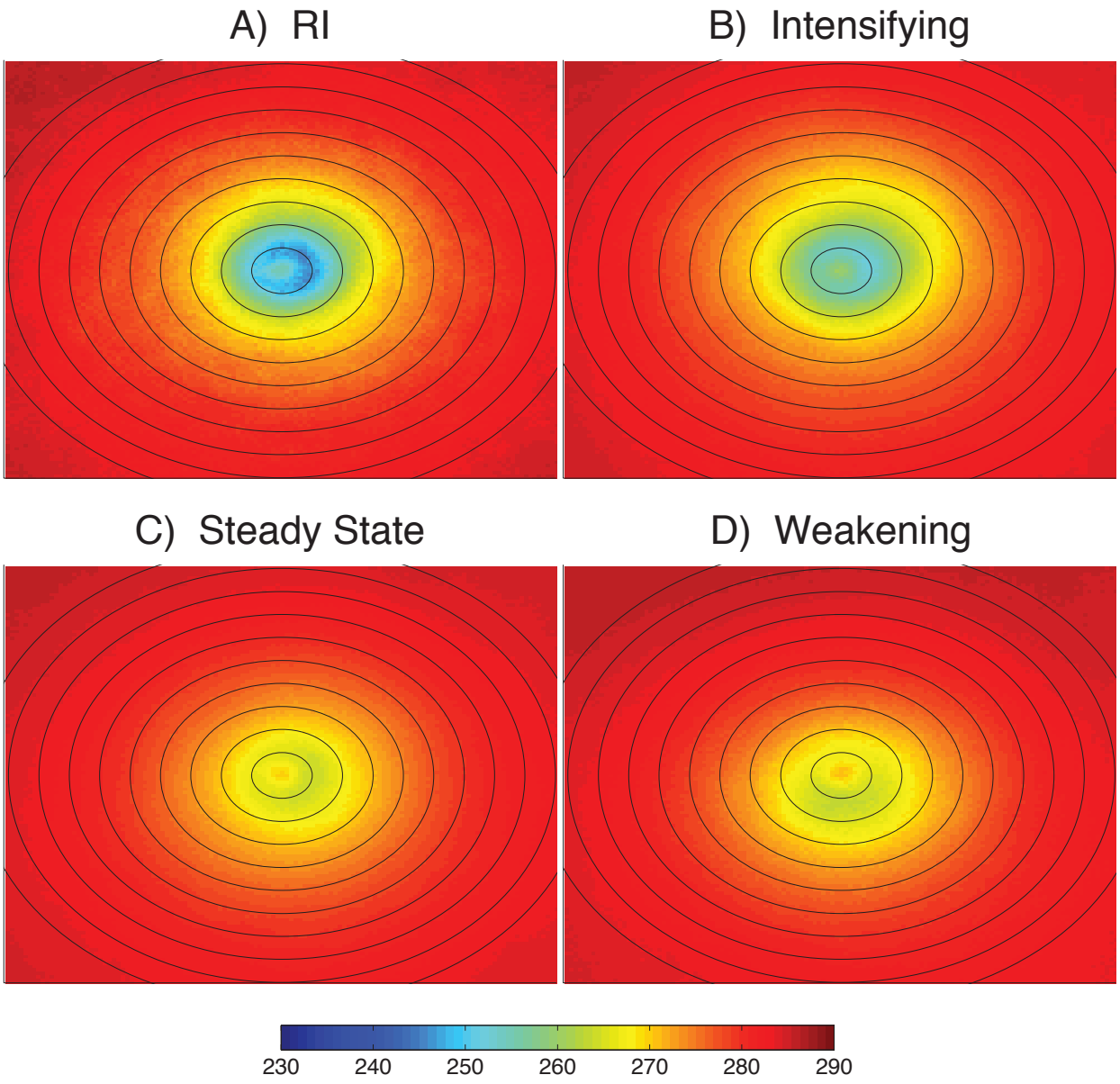

Figure 31: Composite 85 GHz plots (K) for a storm-relative motion coordinate system for all basins globally of TCs undergoing (a) RI, (b) intensifying, (c) steady state, (d) weakening. Storm motion vector is oriented towards the top of the page. Range rings are 55 km.

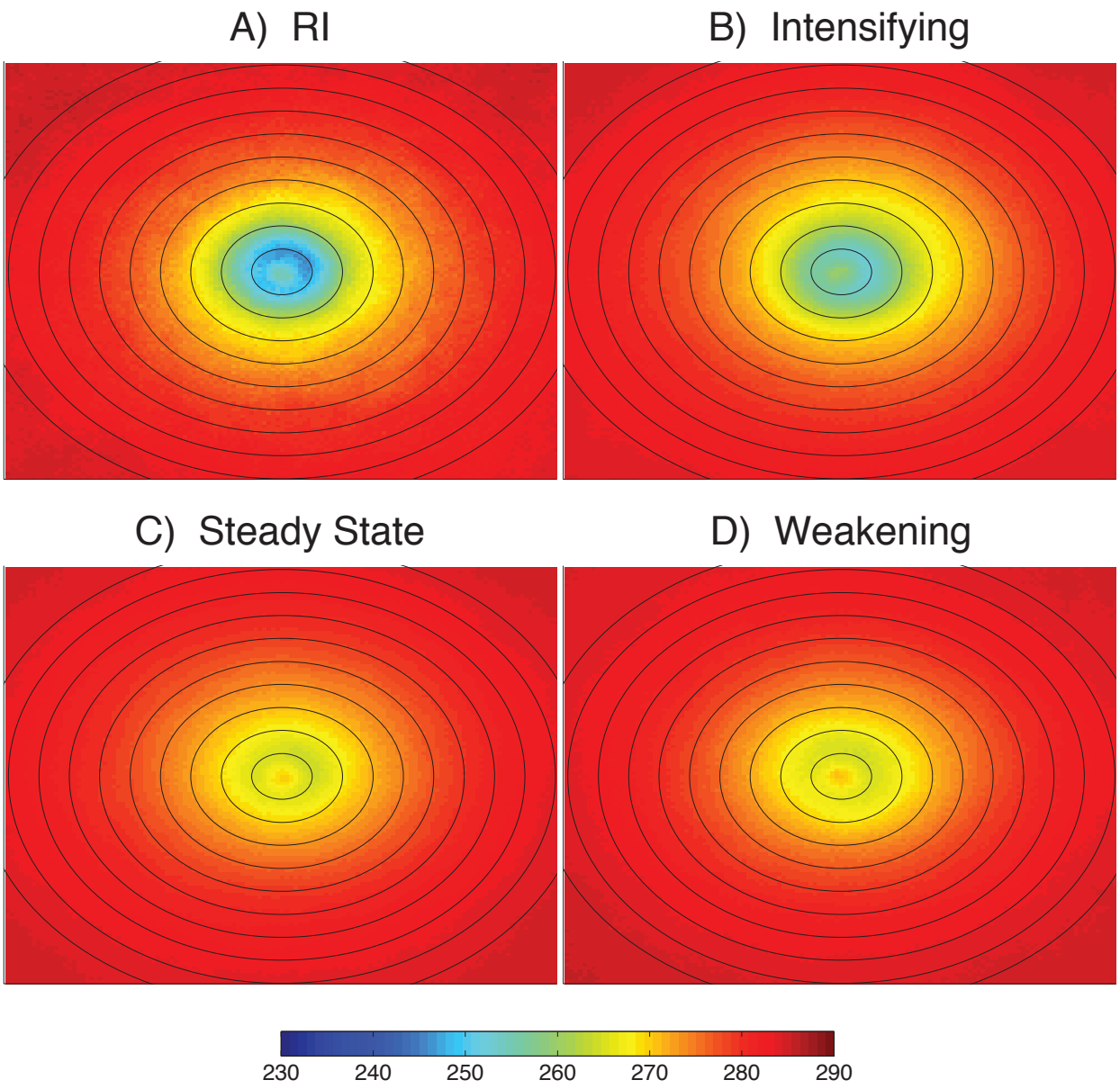

Figure 32: As in Figure 31, except for a shear-relative coordinate system. Shear vector is oriented towards the top of the page.

As has been consistently seen up until this point, 37 GHz portrays little signal once more in the composite plots (Fig. 33, 34). Patterns of the scattering maxima rotating counterclockwise with decreasing intensity change appear in the 37 GHz composites are similar to those seen at 85 GHz. A hint of a ring feature is evident in all of the intensity changes in both coordinate systems but lacks definition with brightness temperatures only

marginally different than the surrounding regions. This is in stark contrast to the findings of Kieper (2008) and Velden et al. (2010) who advocate the use of ring features in 37 GHz data for prediction of periods of RI. The 37 GHz RI composites (Fig. 33a, 34a) show much less distinction in their ring structures than those seen at 85 GHz (Fig. 31a, 32a).

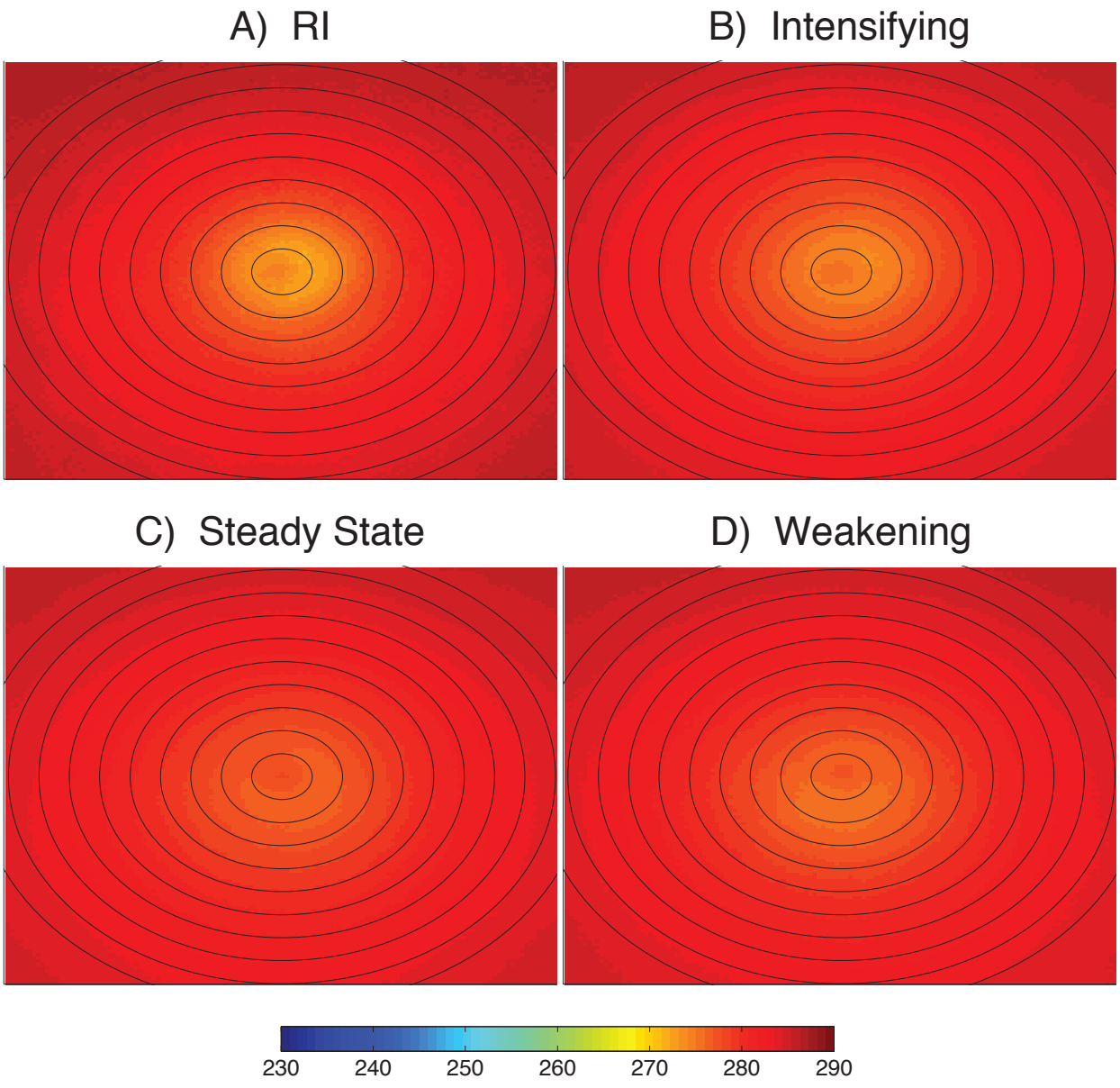

Figure 33: As in Figure 31, except for 37 GHz PCT (K).

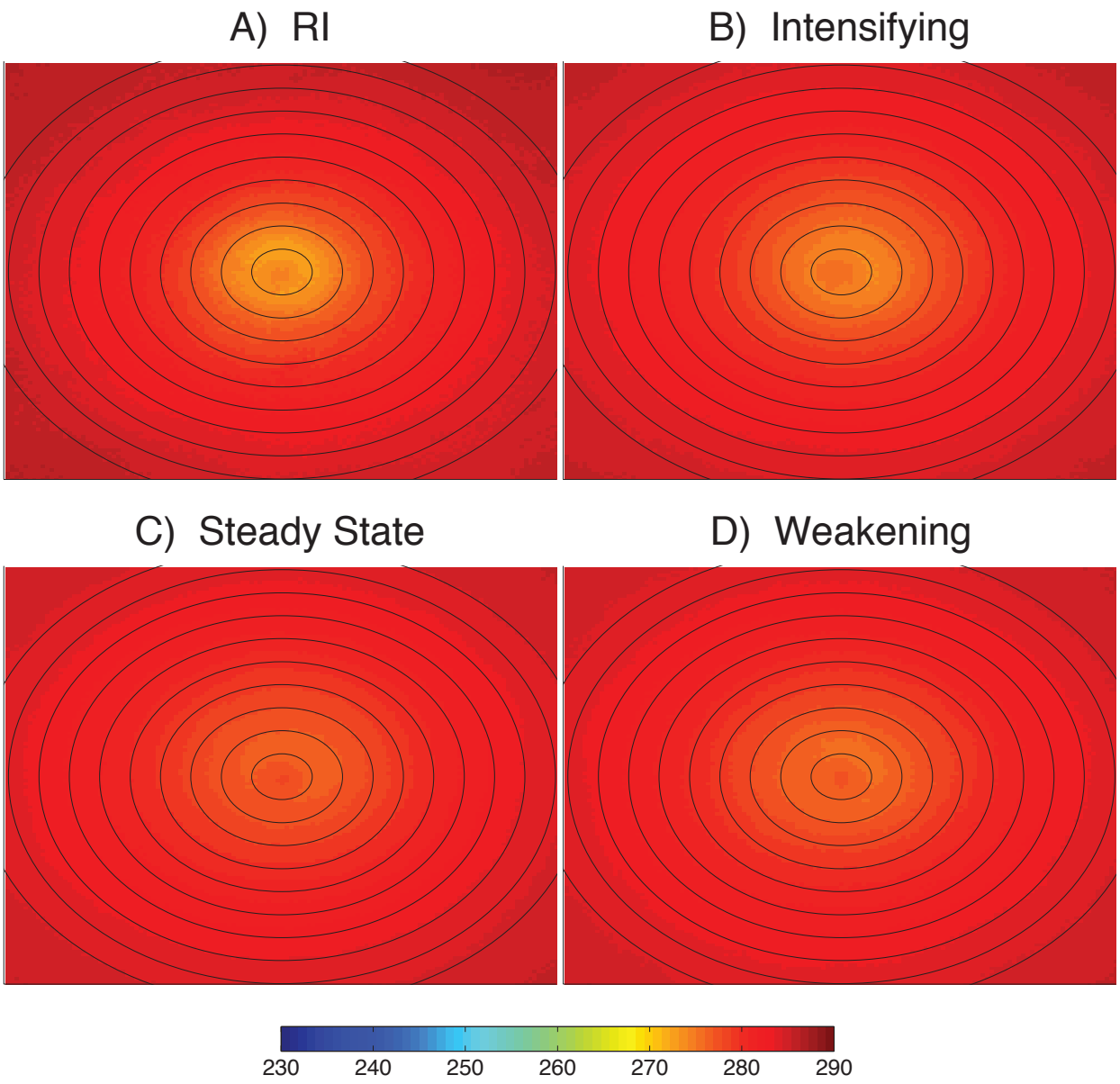

Figure 34: As in Figure 31, except for 37 GHz PCT (K) and shear-relative coordinate system. Shear vector is oriented towards the top of the page.

Composite rain rate plots (Fig. 35, 36) show shallow convective rain rates approaching 10 mm/hr to the right of storm motion in the RI storm-relative composite (Fig. 35a). These are collocated with the regions of strongest depressed PCTs seen at 85 GHz (Fig. 31a) and 37 GHz (Fig. 33a). Intensifying storms (Fig. 35b) hold a strong rainfall signal to the right of storm motion as well. The most evident feature, however, is the near

total apparent lack of rainfall structure evident in the steady state (Fig. 35c) and weakening plots (Fig. 35d) with rainfall below 4 mm/hr throughout the entire 500 x 500 km domain. A hint of a ring structure is apparent although ill defined, which may be a byproduct of the coarse native resolution of the 19 GHz brightness temperatures utilized in the rain rate algorithm. The shear-relative rain rates have the precipitation maxima rotate from upshear for RI systems (Fig. 36a) to the right of the shear vector for intensifying systems (Fig. 36b). Once more the steady state and weakening plots show little signal overall (Fig. 36c, 36d).

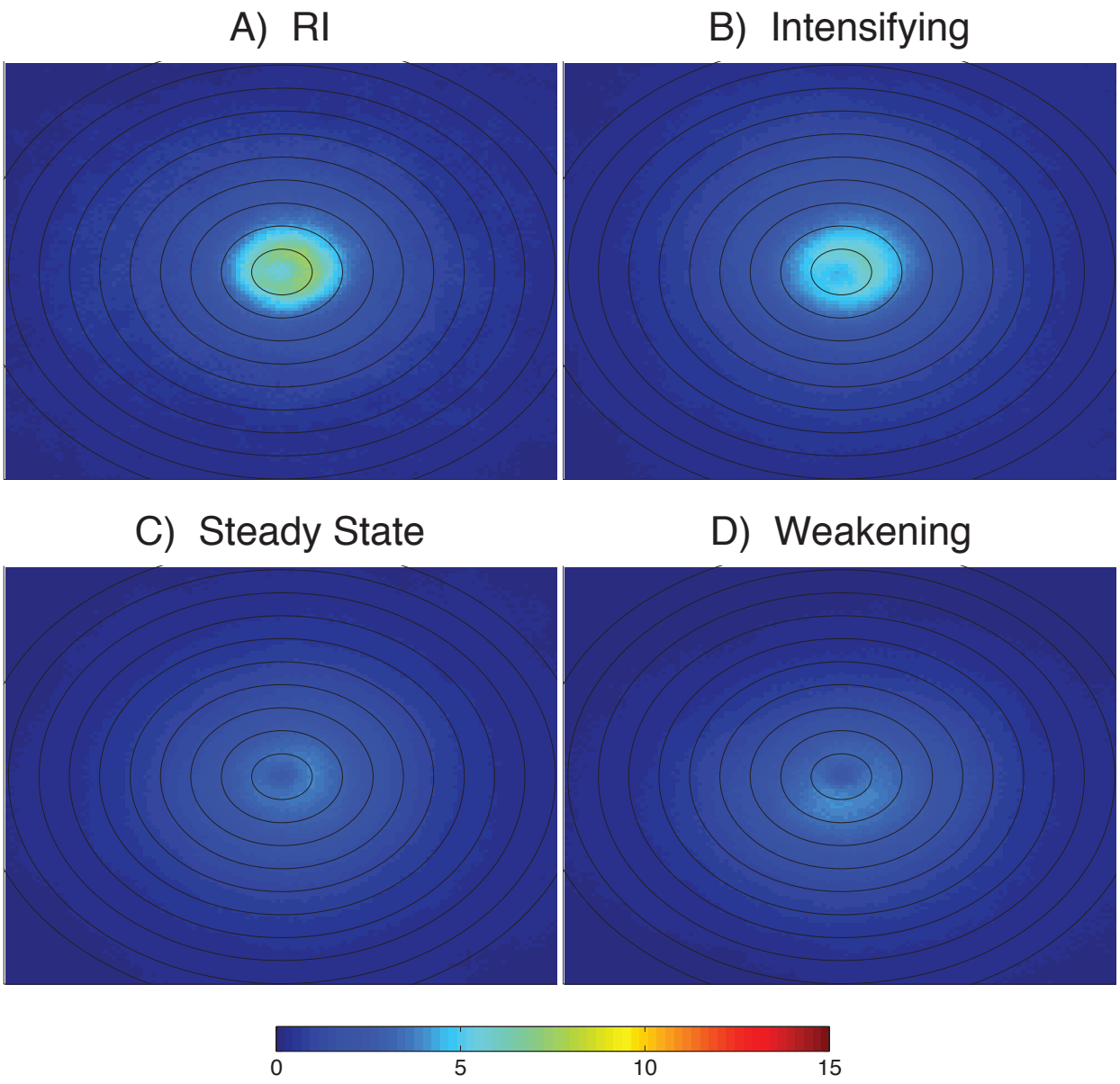

Figure 35: As in Figure 31, except for rain rates (mm/hr).

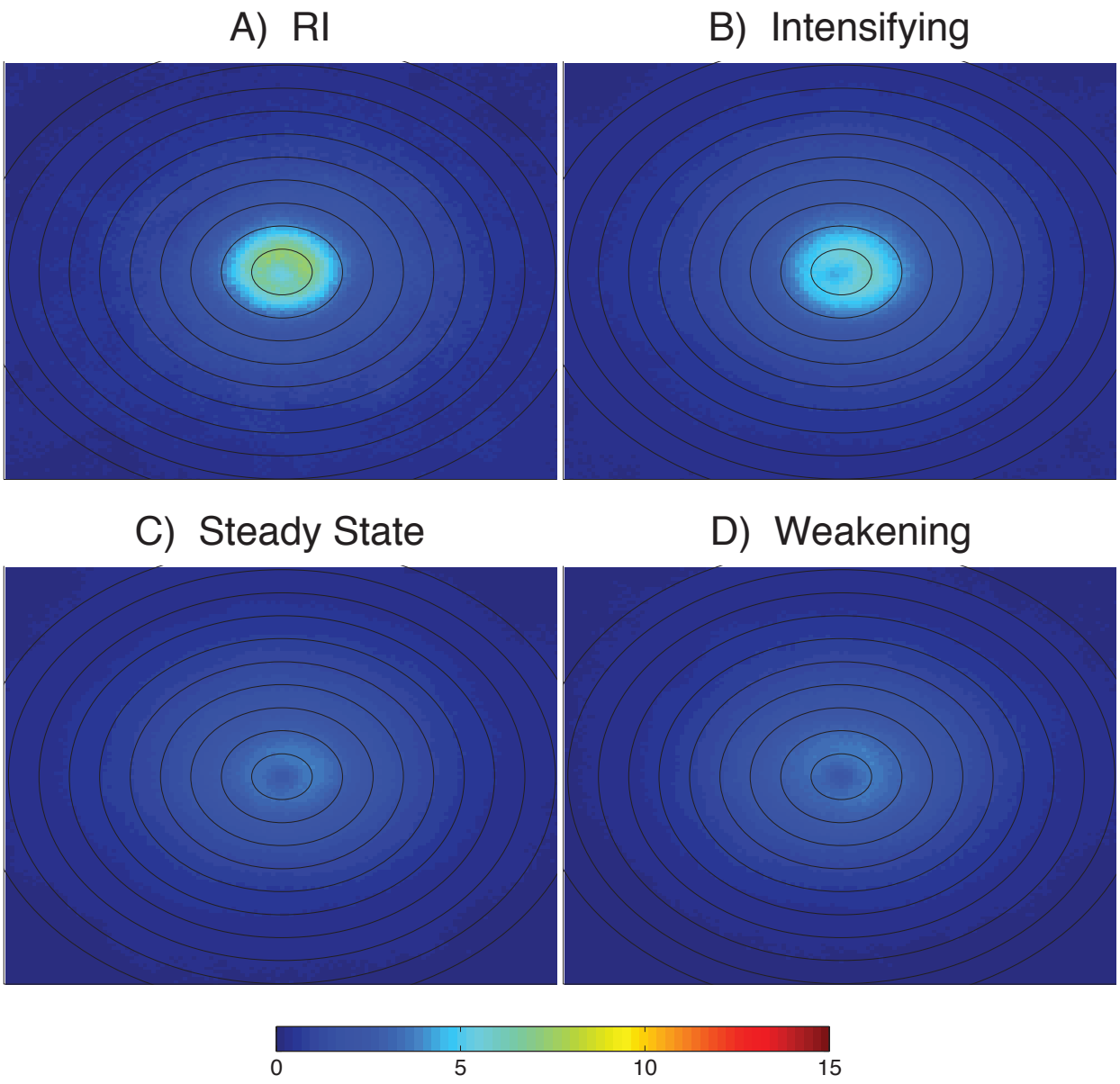

Figure 36: As in Figure 31, except for rain rates (mm/hr) and shear-relative coordinate system. Shear vector is oriented towards the top of the page.

Due to the nature of composite plots, more intense convective features are smoothed and it is possible that the ring structures that are well pronounced in the RI stage (and others) may be a byproduct of the superposition of intense convective maxima at multiple azimuths near the TC core, and in fact not of a true ring-like structure. To evaluate

this possibility, standard deviations (σ) are created for each point on the composites using the following equation:

$$\sigma = \sqrt{\frac{1}{N-1}\left[\sum_{i=0}^{N-1} x_i^2 - \frac{1}{N}\left(\sum_{i=0}^{N-1} x_i\right)^2\right]}$$

85 GHz standard deviations for the storm-relative (Fig. 37) and shear-relative coordinate systems (Fig. 38) appear largely similar to one another. For systems experiencing RI the highest standard deviations are found within 55 km of the TC center (Fig. 37a, 38a). Causes for this can be byproducts of the developing eyewall at varying radii or cases of RI similar to those noted by Molinari and Vollaro (2010) in a supercellular environment. The locations of the ring features with maximum ice-scatter at 85 GHz in the composite plots (Fig. 31a, 32a) exist at larger radii than these maximum values. Intensifying TCs hold the highest standard deviations among all intensity changes (Fig. 37b, 38b) with standard deviations reaching values near 30 K over the innermost ½°. Steady state (Fig. 37c, 38c) and weakening systems (Fig. 37d, 38d) produce weaker standard deviation values than RI or intensifying TCs with values on the order of 20K for much of the 110 km annuli and its interior.

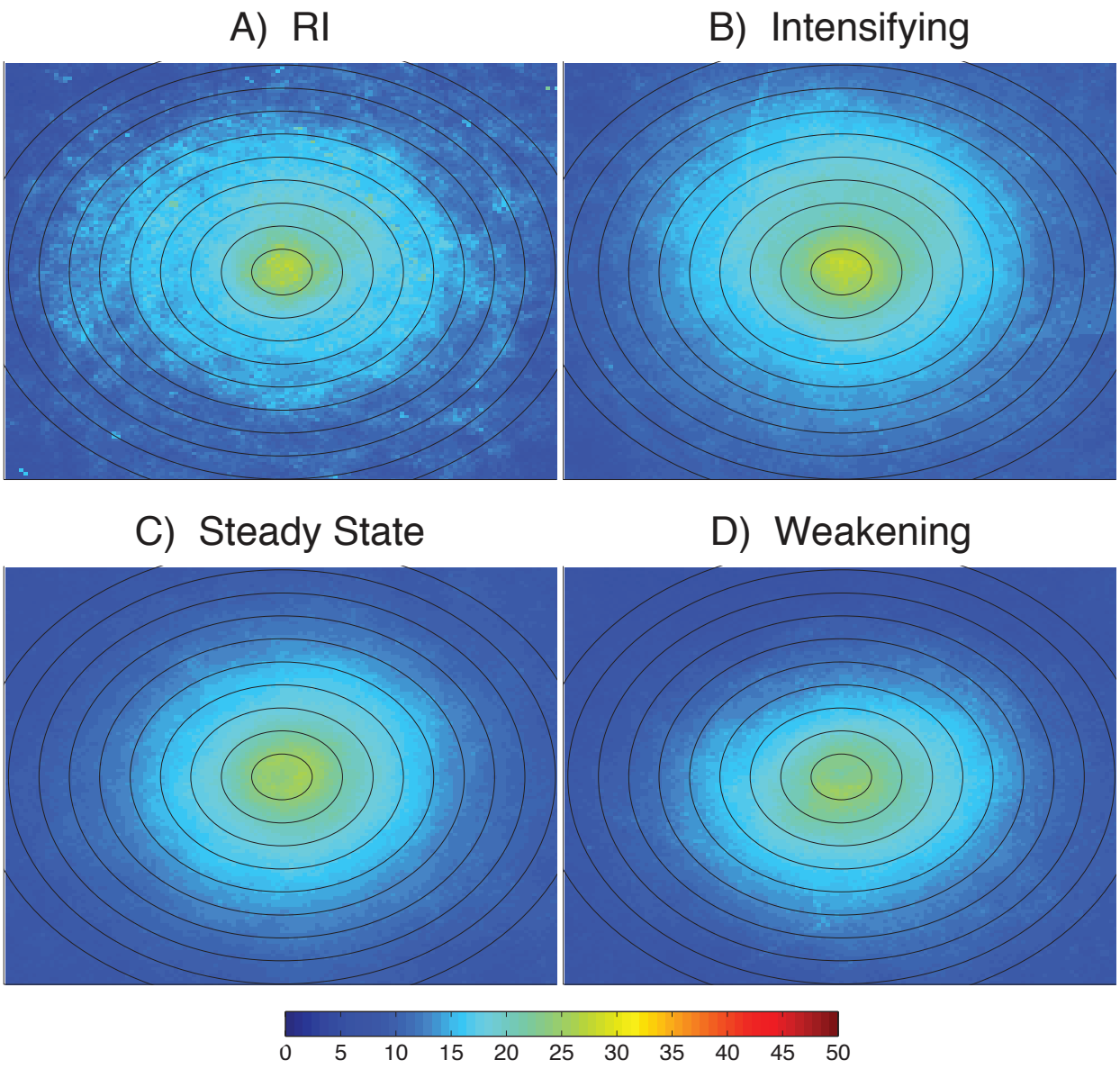

Figure 37: Standard deviation values (K) for each 8 km grid point of composite 85 GHz plots (K) for a storm-relative coordinate system for all basins globally of TCs undergoing (a) RI, (b) intensifying, (c) steady state, (d) weakening. Storm motion vector is oriented towards the top of the page. Range rings are 55 km.

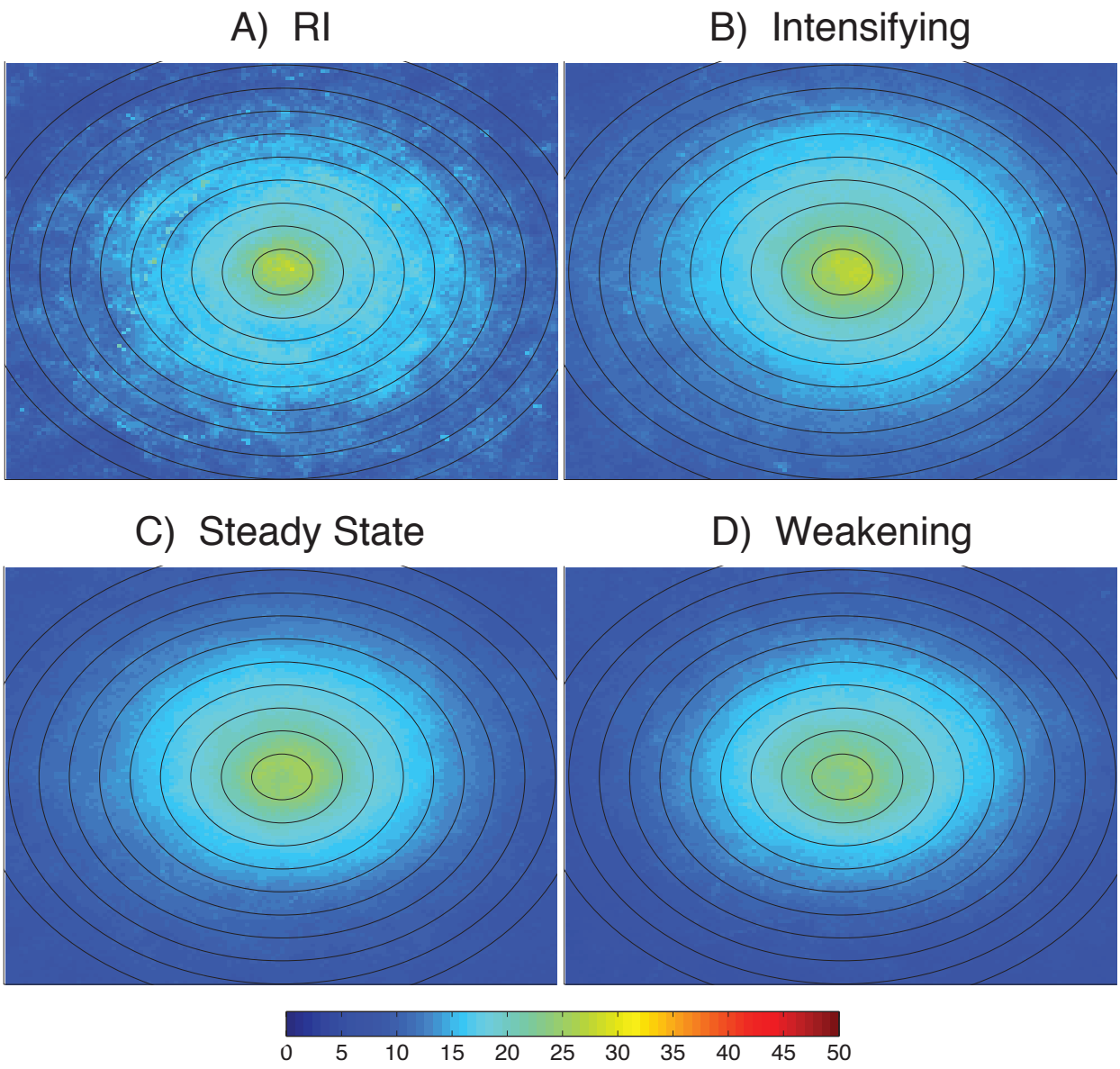

Figure 38: As in Figure 37, except for a shear-relative coordinate system. Shear vector is oriented towards the top of the page.

Standard deviations for the rain rates (Fig. 39, 40) are on the order of the magnitude of the composite plots they are meant to evaluate. The spatial coverage of standard deviations > 5 mm/hr increases with weakening intensity change classification, most notable in the storm-relative weakening rain rates (Fig. 39d). Maximum standard deviations are roughly 7 mm/hr in the core for RI systems in each coordinate (Fig. 39a,

40a). Once more these are inside the ring of highest rain rates in the composite plots (Fig. 35a, 36a) and are potentially a byproduct of the varying radii of a ring feature in RI systems or another mode of RI. Due to the little variation seen in the 37 GHz composites their standard deviations are not shown, as all values were < 5 K for all intensity changes and coordinates.

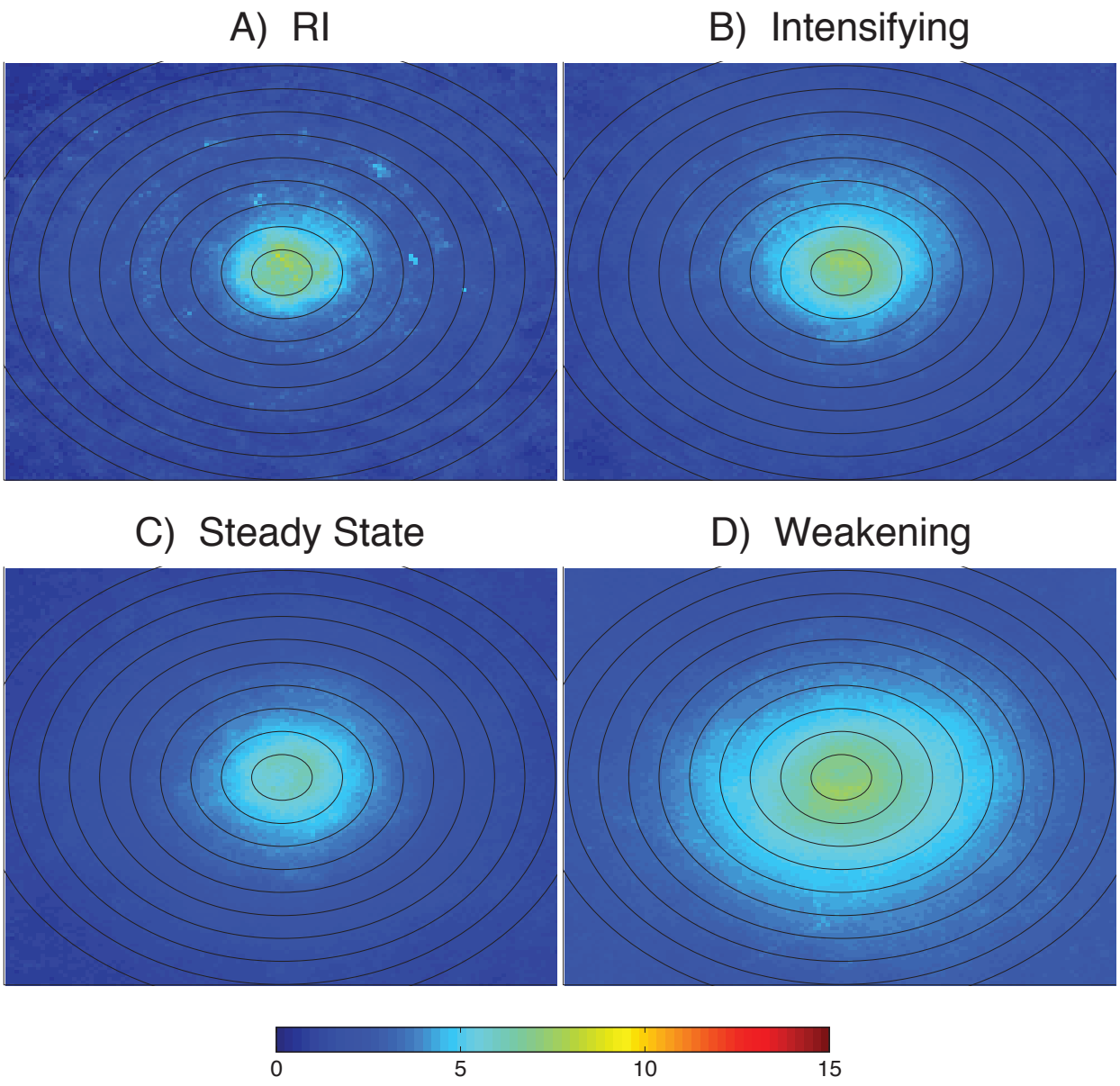

Figure 39: As in Figure 37, except for a rain rates standard deviations (mm/hr).

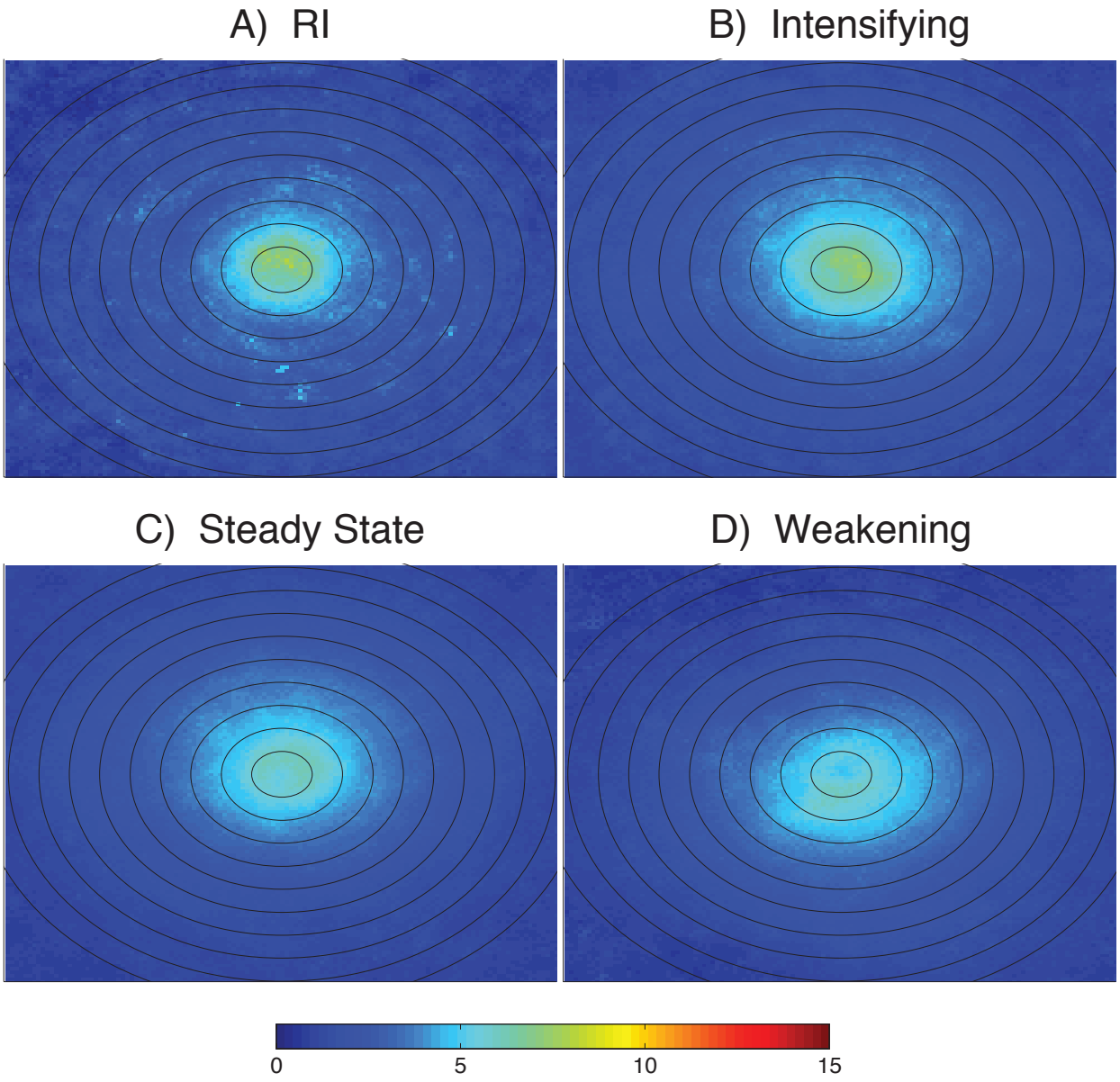

Figure 40: As in Figure 37, except for rain rate standard deviations (mm/hr) a shear-relative coordinate system. Shear vector is oriented towards the top of the page.

To evaluate the structural evolution over the 24-hour period defined for the RI lifecycle in this study, we create similar composite plots of all SSM/I or TMI overpasses of the storm in question during that window. These overpasses are interpolated to the nearest 6-hour time step for use in the composites, therefore errors of up to 3 hours may

be present. The sample sizes utilized in each composite for each of the basins and time steps are listed in Table 4.

	+00 hours	+06 hours	+12 hours	+18 hours	+24 hours
Global	555	454	752	485	706
E. Pacific	156	146	153	96	167
N. Atlantic	75	72	107	52	92
S. Indian	107	76	83	144	89
S. Pacific	73	50	89	57	65
W. Pacific	126	101	199	106	178

Table 4: Sample sizes used in the creation of the RI evolution composite plots for each basin and time step.

Figure 41 depicts the 24-hour evolution of TCs undergoing RI at 85 GHz in this manner. Initially the region of brightness temperatures < 245 K is constrained to the right of the storm motion near 55 km (Fig. 41a) before covering all but the western side 6 hours later (Fig. 41b). By 12 hours after initiation of RI this region fully encompasses the TC core (Fig. 41c). Over the next 12 hours (Fig. 41d, e) this ring of convection intensifies with brightness temperatures another 10 K as the convection increases its spatial coverage inward and 24 hours after RI began, the hole in the middle of the ring is barely evident. Figure 42 displays the same data in a shear-relative coordinate system with similar results; the main exception being at 6 hours after RI (Fig. 42b) the ring of brightness temperatures < 245 K is fully circular but fairly ragged and then proceeds to become axisymmetricized over the next 6 hours (Fig. 42c).

37 GHz RI evolution composites were created but are not shown here due to lack of notable structure throughout. In the innermost ½° brightness temperatures were depressed on the order of an additional 5 K but the pattern is simply reminiscent of a

bullseye with no convective ring or other distinguishing features. Standard deviations were also low (< 5K) throughout all times after RI initiation.

Figures 43 and 44 display the RI evolutionary composites for storm-relative and shear-relative rain rates respectively. In the storm-relative coordinate system a developing ring of rain rates > 9 mm/hr begins appearing 6 hours after initiation of RI (Fig. 43b) with a lack of definition to the left of storm motion through 18 hours (Fig. 43d) despite increases on the right in locations up to 12 mm/hr. By the end of the RI cycle (Fig. 43e) the 9 mm/hr ring encircles the core with the maximum values having rotated to the left of storm motion. As in the 85 GHz data (Fig. 41, 42) the ring feature's interior compresses as the ring's width expands inward over the RI process. The shear-relative precipitation rate composites (Fig. 44) display a ragged ring of shallow convection for the first 12 hours of RI that becomes well defined by 18 hours (Fig. 44c). Between 18 (Fig. 44d) and 24 (Fig. 44e) hours after initiation the 55 km annuli is nearly completely filled with rain rates > 9 mm/hr with only a small region of 7 mm/hr rates in the mean storm center which shrinks over this 6 hour period.

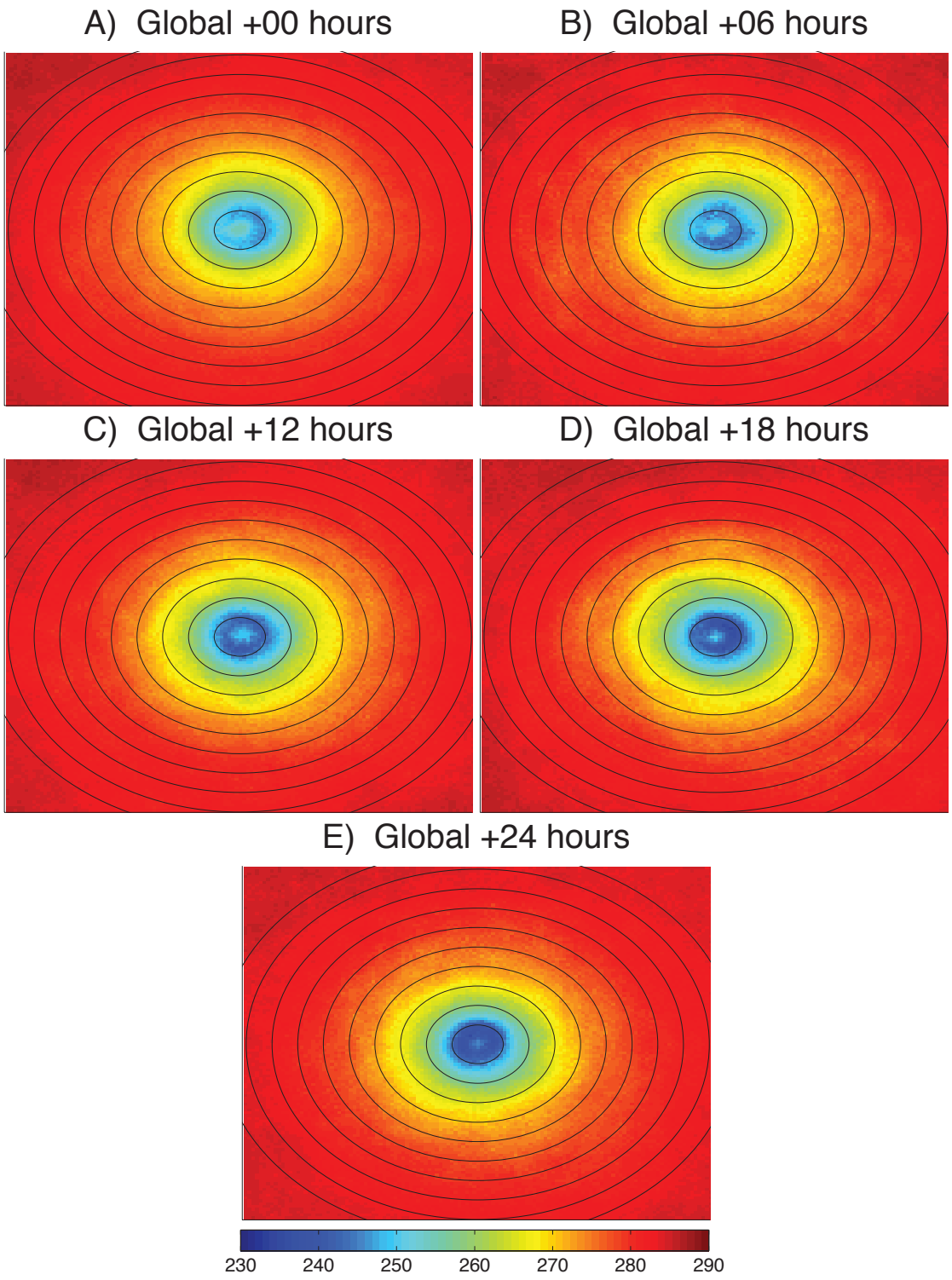

Figure 41: Composite 85 GHz PCT (K) for a storm-relative motion coordinate system for all basins globally of TCs undergoing RI and their structure throughout the 24 hour period at (a) time of initial overpass, (b) 6 hours after overpass, (c) 12 hours after overpass, (d) 18 hours after overpass, and (e) 24 hours after overpass. Storm motion vector is oriented towards the top of the page. Range rings are 55 km.

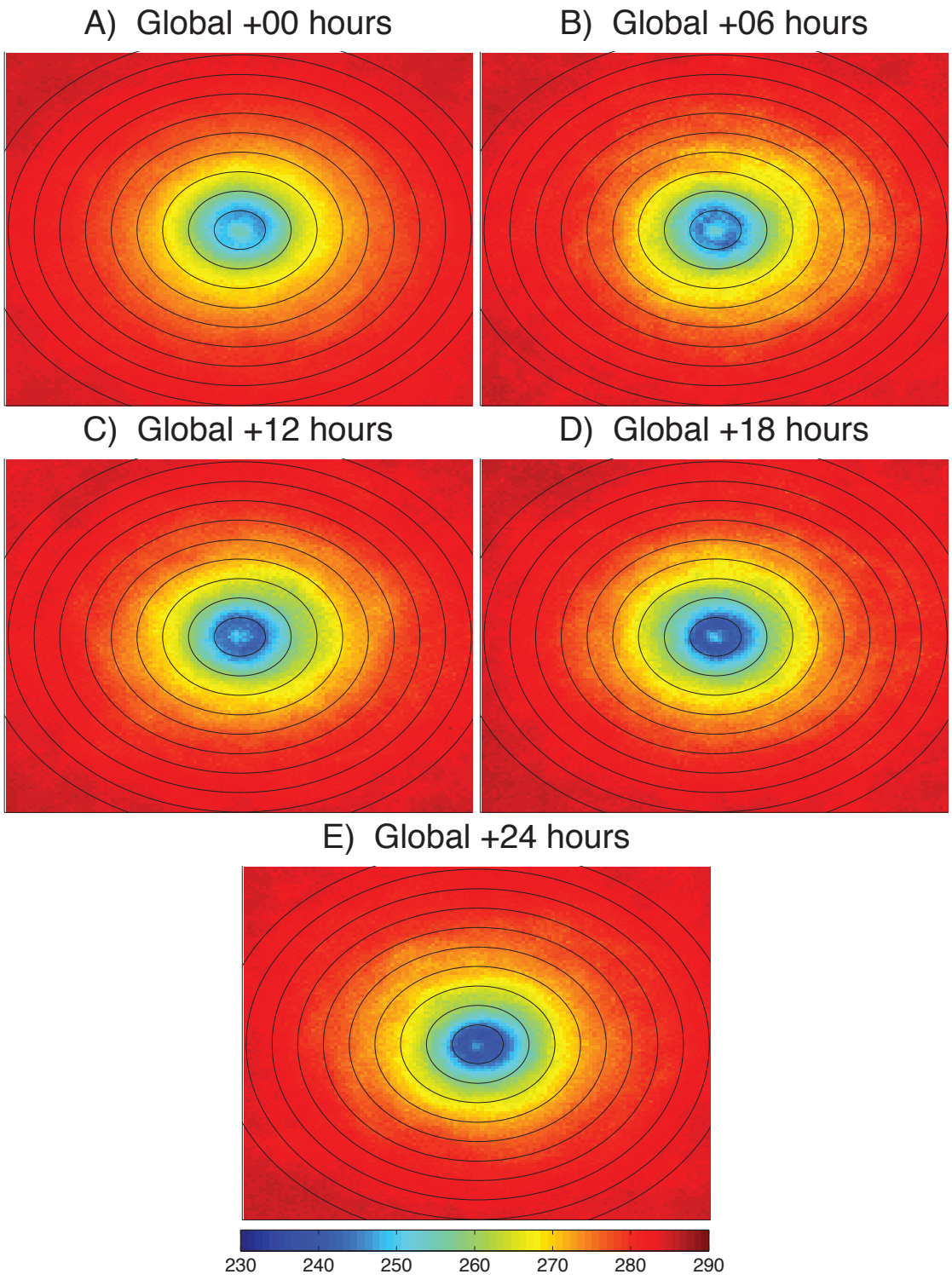

Figure 42: As in Figure 41, except for a shear-relative coordinate system. Shear vector is oriented towards the top of the page.

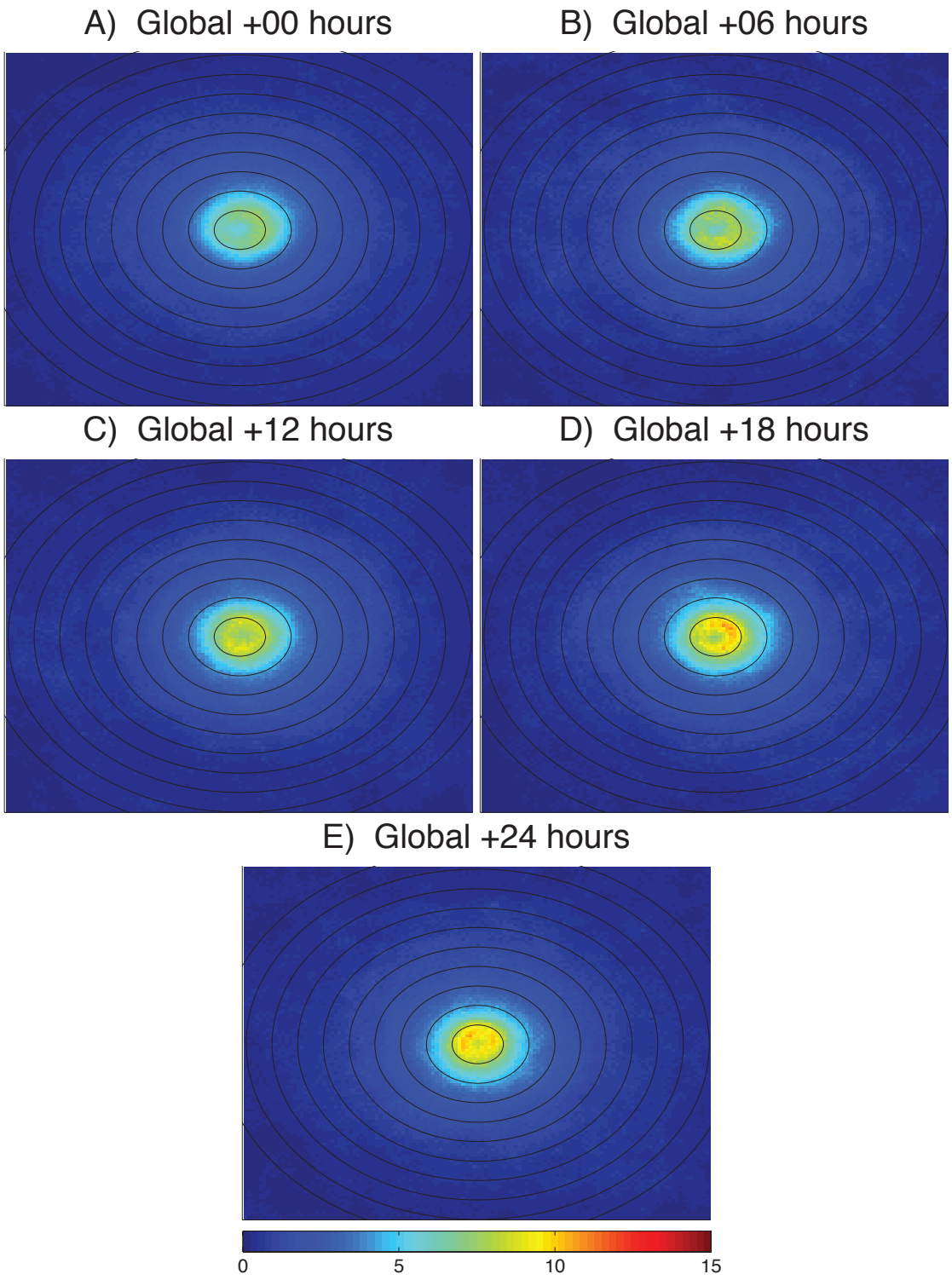

Figure 43: As in Figure 41, except for rain rates (mm/hr).

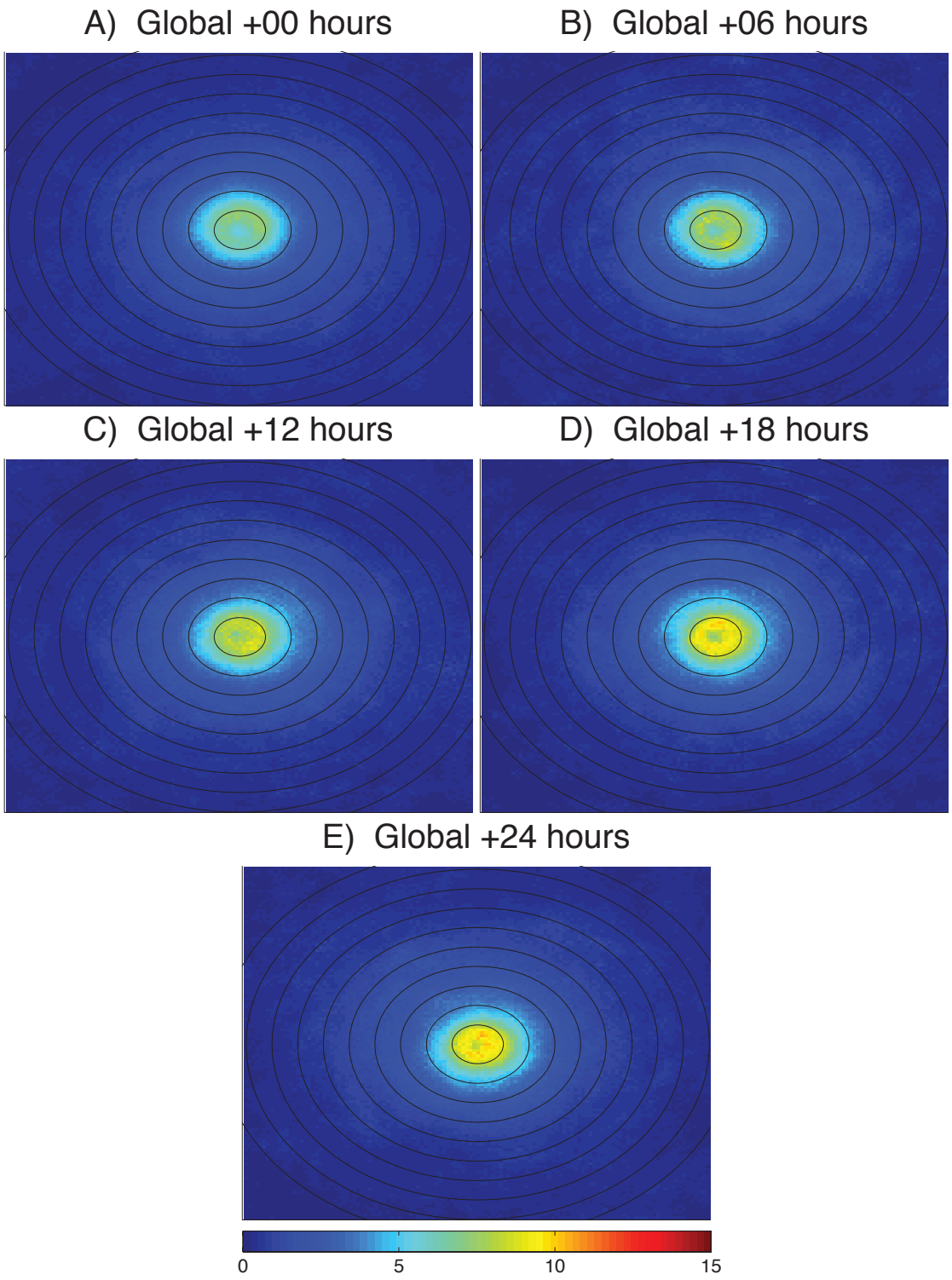

Figure 44: As in Figure 41, except for shear-relative coordinate system rain rates (mm/hr). Shear vector is oriented towards the top of the page.

As done with the composites for all intensity changes, standard deviations are evaluated for each pixel in the evolution composite plots (Fig. 45-48). For standard deviations of 85 GHz PCT values increase over time throughout the core in both coordinate systems, suggesting that convective variability (i.e., convective bursts) is a byproduct of the RI process, not a source of it. More analysis of this is planned by extending the RI evolution period back 24 hours prior to the initiation of RI. Over time these high values become increasingly focused in the core and by 24 hours (Fig. 45e, 46e) are focused in a region only 30-40 km from the storm center. Another source of these variations once again may be the ring structure appearing at varying radii.

Rain rate standard deviations (Fig. 47, 48) increase over time in both coordinate systems and also become more focuses, with the exception of the transition from RI initiation (Fig. 47a) to 6 hours afterward (Fig. 47b) in the storm-relative coordinate system. Here the standard deviations increase slightly and expand outward from the initial overpass but by 12 hours (Fig. 47c) retract inward. The highest standard deviations are consistently around 7 mm/hr and appear to the interior of the maximum rain rate ring structure seen earlier (Fig. 43, 44).

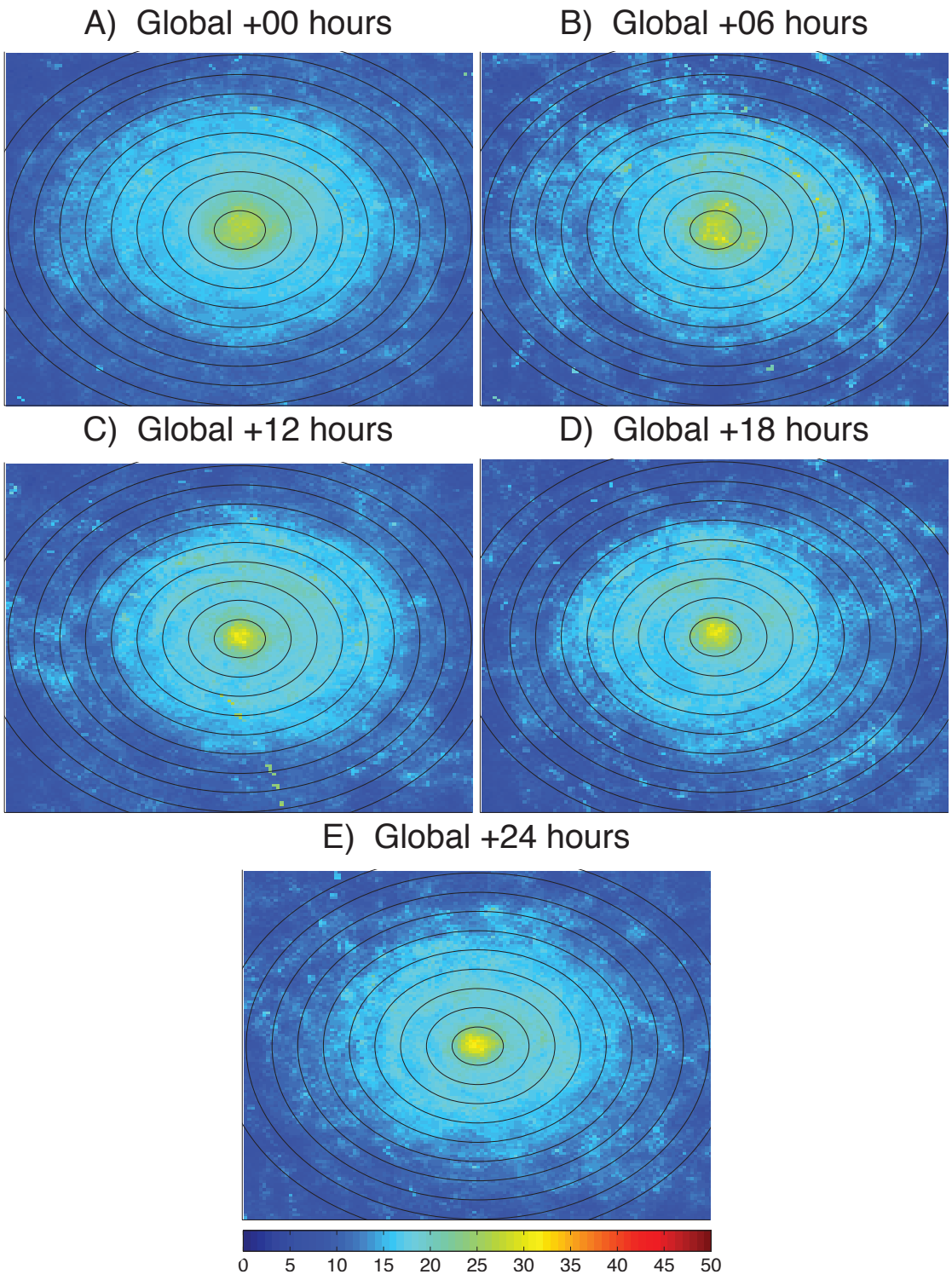

Figure 45: Composite 85 GHz standard deviation (K) for a storm-relative coordinate system for all basins globally of TCs undergoing RI and their structure throughout the 24 hour period at (a) time of overpass, (b) 6 hours after overpass, (c) 12 hours after overpass, (d) 18 hours after overpass, and (e) 24 hours after overpass. Storm motion vector is oriented towards the top of the page. Range rings are 55 km.

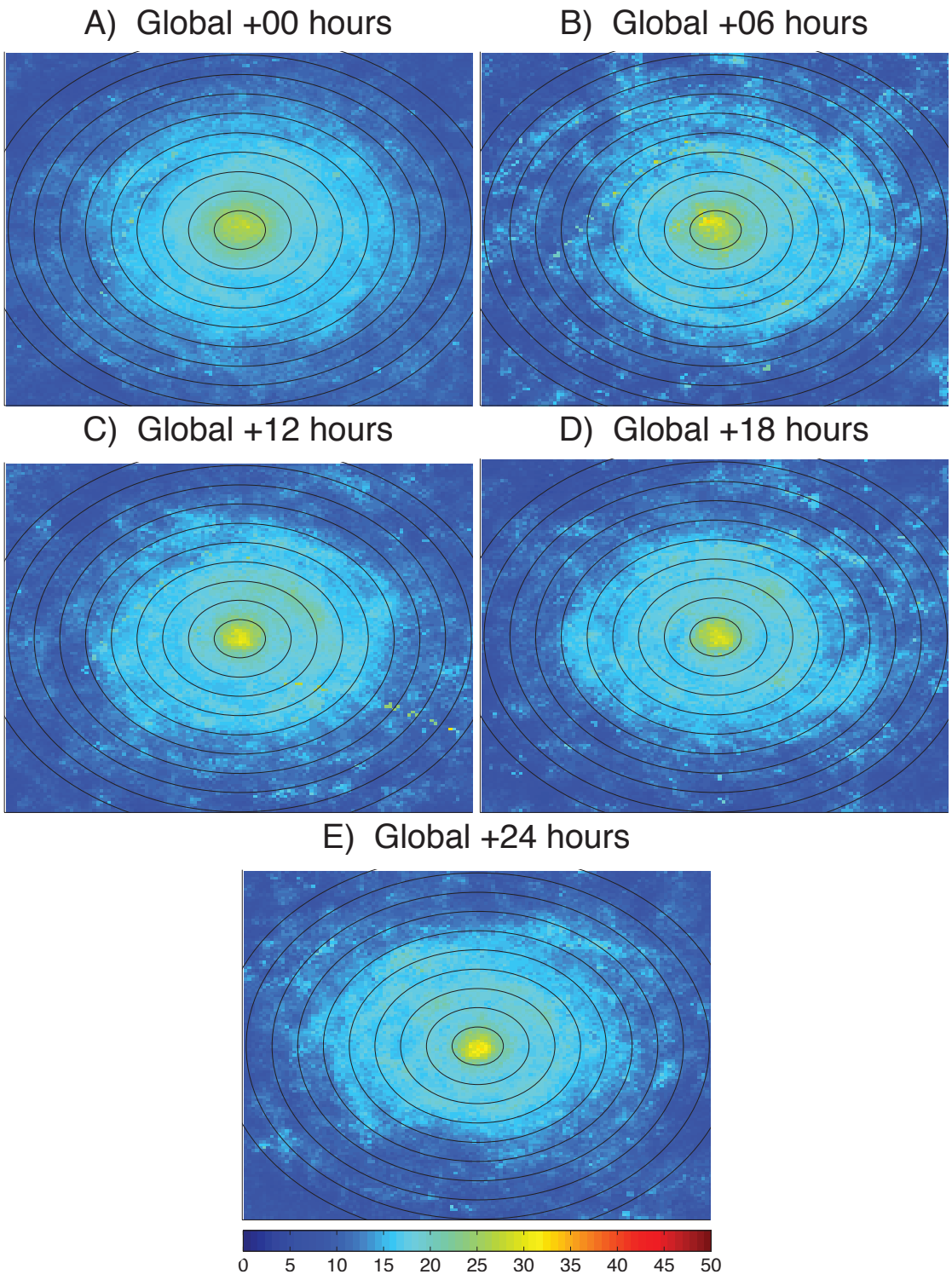

Figure 46: As in Figure 45, except for a shear-relative coordinate system. Shear vector is oriented towards the top of the page.

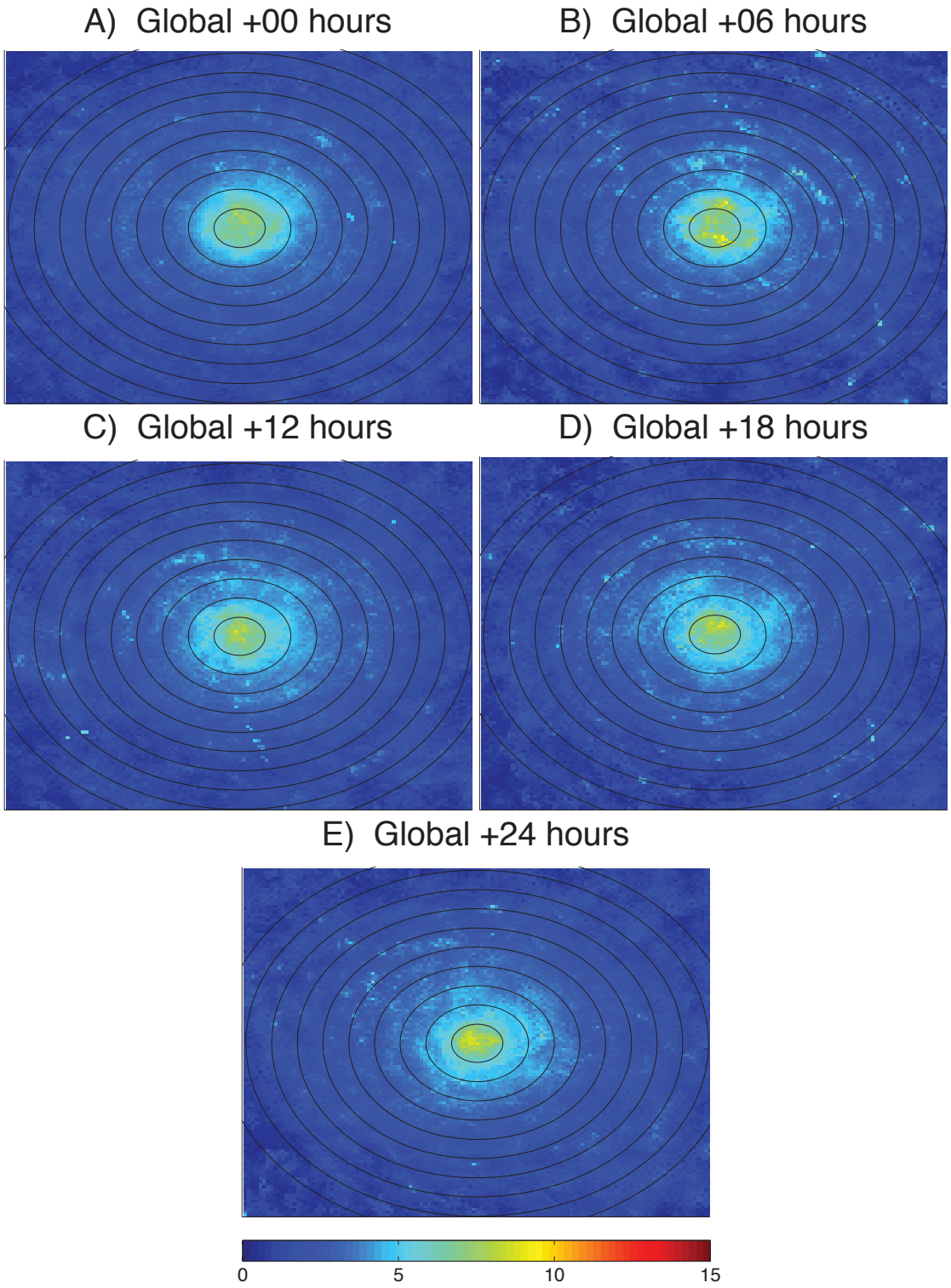

Figure 47: As in Figure 45, except for rain rate standard deviations (mm/hr).

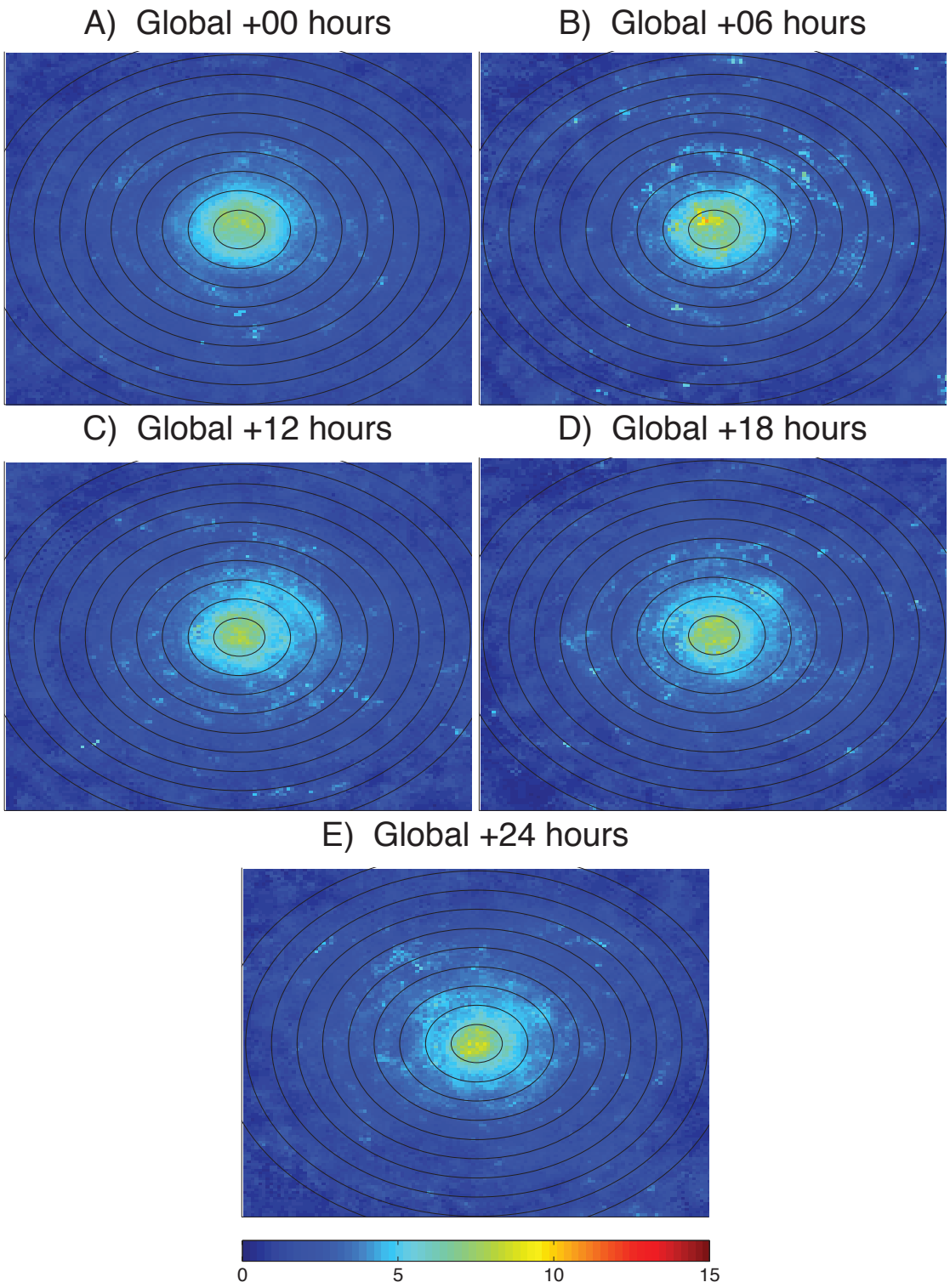

Figure 48: As in Figure 45, except for rain rate standard deviations (mm/hr) and shear-relative coordinate system. Shear vector is oriented towards the top of the page.

Evolution composites are also created of 85 GHz PCT and rain rates in shear-relative and storm-relative coordinates for the 5 oceanic basins with > 70 overpasses of RI being initiated: the East Pacific, North Atlantic, South Indian, South Pacific, and West Pacific. Across these basins large structural differences throughout the RI process are evident.

East Pacific 85 GHz PCT is shown in Figures 49 and 50. In the storm-relative coordinate system, a region of depressed PCTs on the order of 240 K at RI initiation (Fig. 49a) is to the right of the storm center. Six hours later (Fig. 49b) the increased ice-scatter signature has spread some towards the rear left of the system and after 12 hours (Fig. 49c) they nearly fully encompass the TC core. At 18 hours after RI begins the convection in this region has intensified and expanded inwards towards the storm center. Finally at 24 hours these depressed PCT values fully encircle the TC core with a region of 15-25 km in their midst with warmer values.

In the shear-relative coordinate system the composites appear very different (Fig. 50). A ring feature that intensifies and grows towards the TC center throughout the RI cycle is prominent at all time steps. Little directional dependence is seen in the area of lowest PCTs at all periods, with the exception of an upshear region of high depression 12 hours after RI inception (Fig. 50c).

The rain rate composites (Fig. 51, 52) depict on marginal differences for the East Pacific than the 85 GHz PCT composites. In the storm-relative coordinates (Fig. 51) a region of 8 mm/hr is collocated with the region of 85 GHz PCT < 240 K (Fig. 49). Initially in the shear-relative coordinates little structure is evident as RI is initiated (Fig. 52a) with a region of rain rates > 7 mm/hr extending to approximately 60 km with a hint of a ring in its middle. The ring does not become clearly apparent until 18 hours after RI begins (Fig. 52c)

at which time it is surrounded by rain rates of 9 mm/hr. As the 24-hour RI examination period finishes the maximum rain rates are biased towards the upshear side of the TC core but a distinct ring of elevated precipitation rates remains (Fig. 52d).

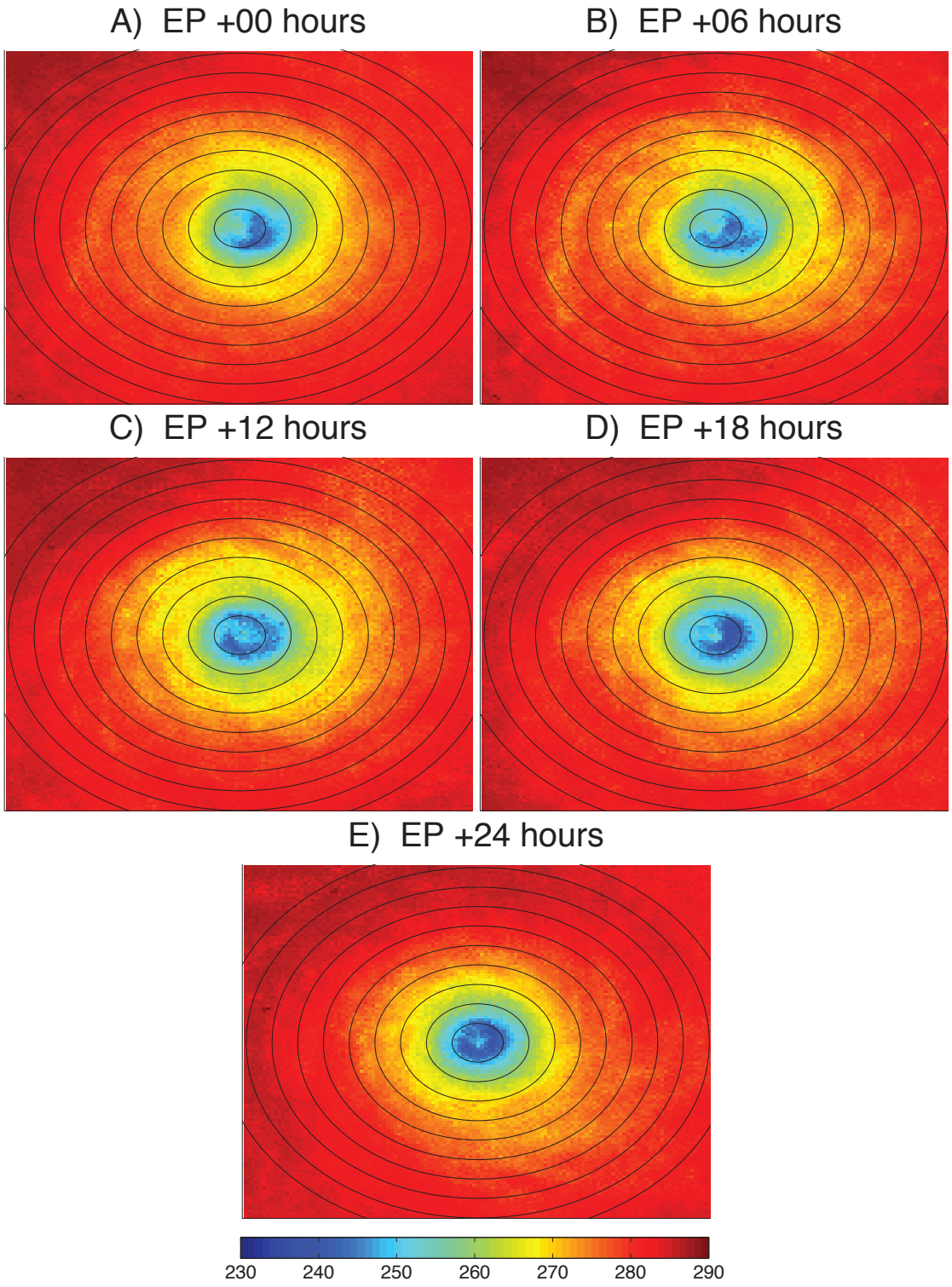

Figure 49: As in Figure 45, except for the East Pacific.

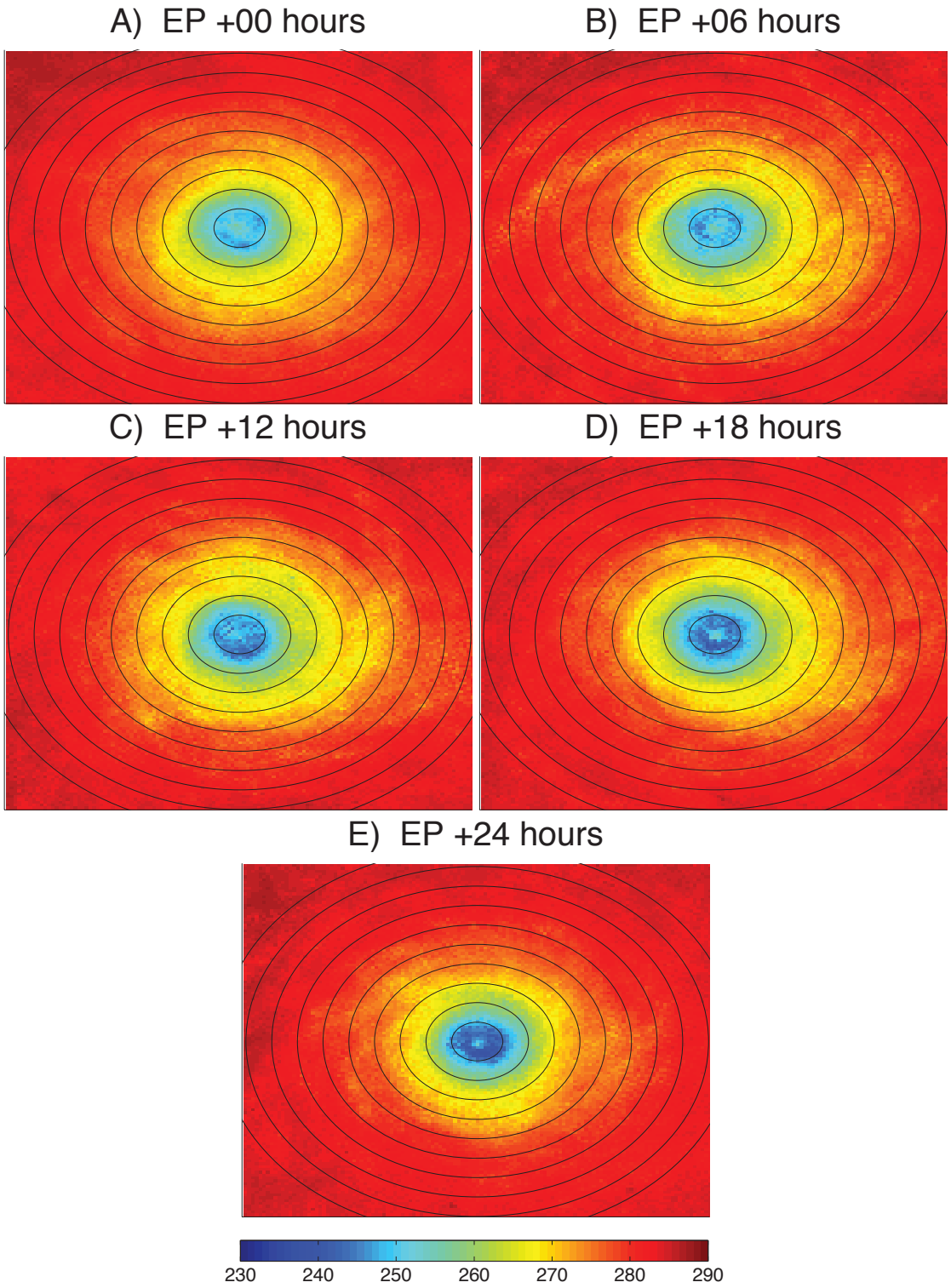

Figure 50: As in Figure 45, except for the East Pacific in a shear-relative coordinate system. Shear vector is oriented towards the top of the page.

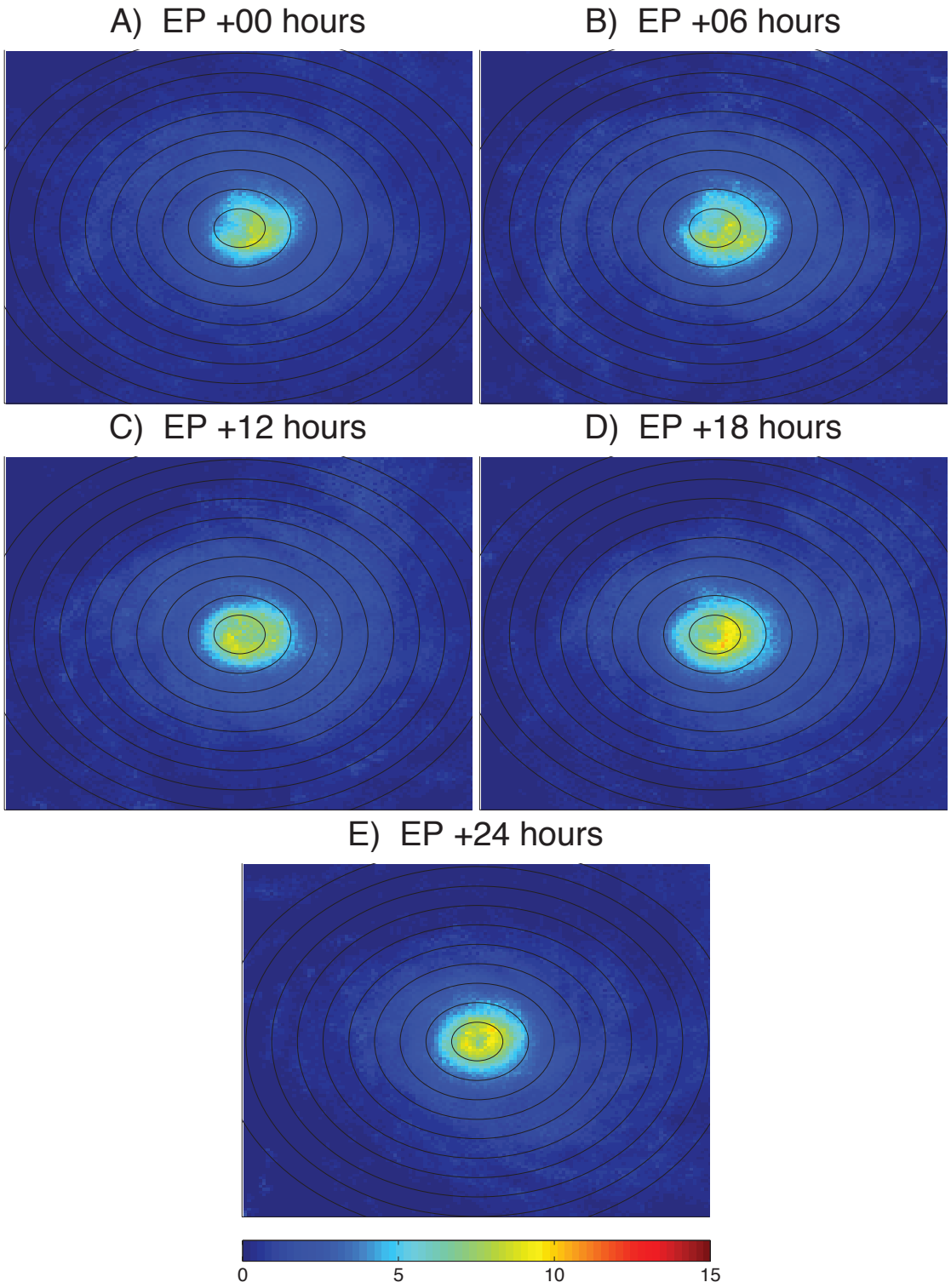

Figure 51: As in Figure 45, except for the East Pacific rain rates (mm/hr)

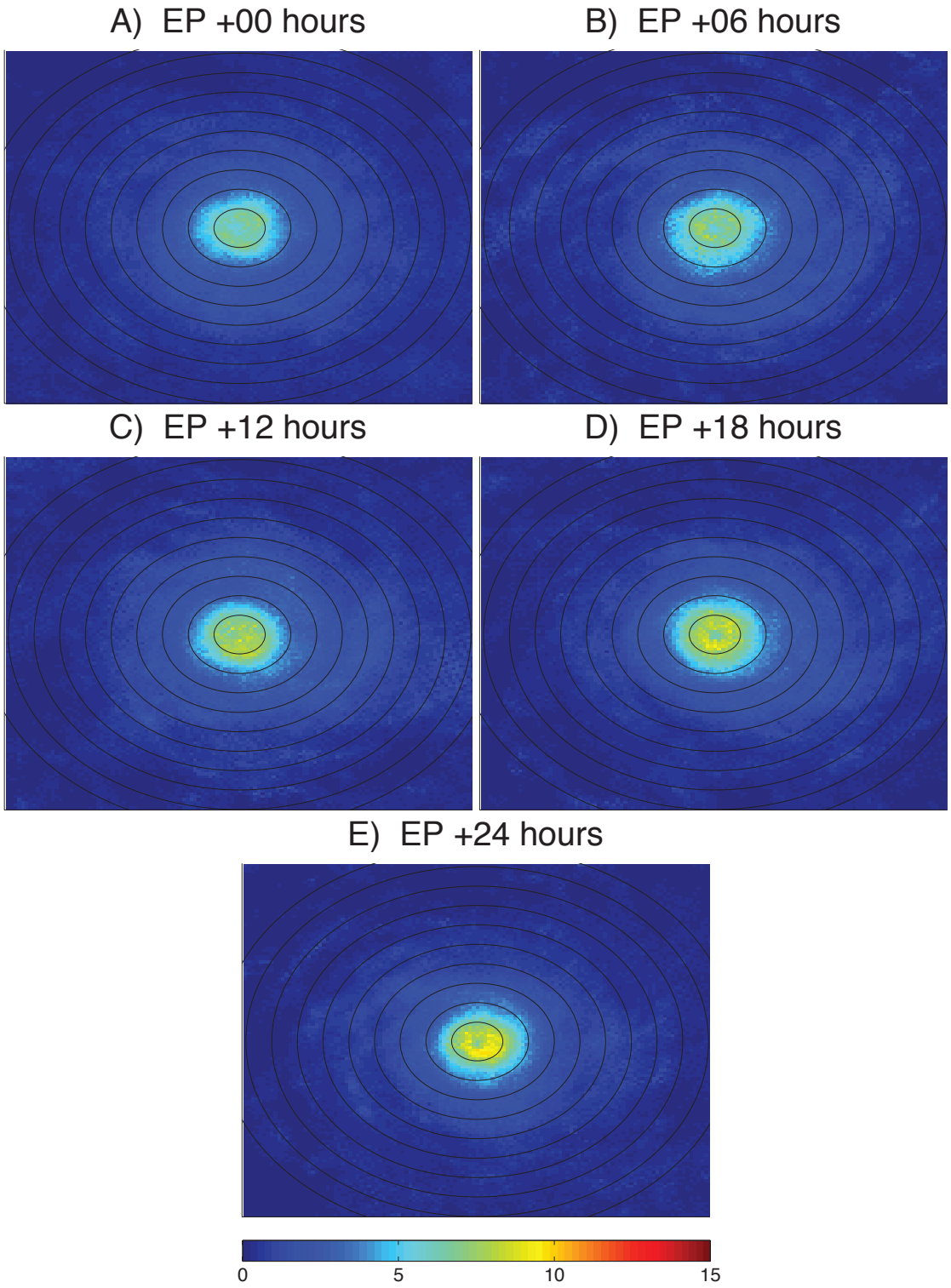

Figure 52: As in Figure 45, except for the East Pacific in a shear-relative coordinate system. Shear vector is oriented towards the top of the page.

The North Atlantic displays a less cohesive structure typically for RI systems, with asymmetries evident in the ring structure throughout. Throughout the first 18 hours of the RI cycle the depressed storm-relative 85 GHz PCTs are biased high towards the rear of the system before shifting to its left side as the RI examination period ends (Fig. 53). An eye-like structure is evident throughout the storm-relative PCT plots with a fairly consistent radius of approximately 30 km. The shear-relative brightness temperatures are fairly similar with the depressed PCTs biased to the right of the shear vector throughout the RI cycle. The ring and eye structures are apparent again, however it appears the maximum intensity of the ice scattering signature occurs 18 hours after RI begins (Fig. 54d) with the greatest spatial coverage of PCTs < 240 K and several embedded pixels approaching 230 K.

Evolution composites for rain rate estimates in the North Atlantic show the ring and eye structure throughout their evolution at all times (Fig. 55, 56). For the storm-relative coordinate system (Fig. 55) the precipitation maxima is consistently located to the rear of the system, with the exception of at 24 hours (Fig. 55e) where it is to the left of the storm's track. These maxima are found upshear in the shear-relative coordinates before shifting to the right of the shear at 18 (Fig. 56d) and 24 hours (Fig. 56e). At 24 hours the convection in the eyewall of the composites are asymmetric, with the rain rates at the 55 km distance to the right of storm-motion being 6 mm/hr and to its left being 9-11 mm/hr (Fig. 55e). These same magnitudes occur in the shear-relative system composite at 24 hours (Fig 56e), but with the 6 mm/hr values sited downshear and the 9-11 mm/hr values upshear.

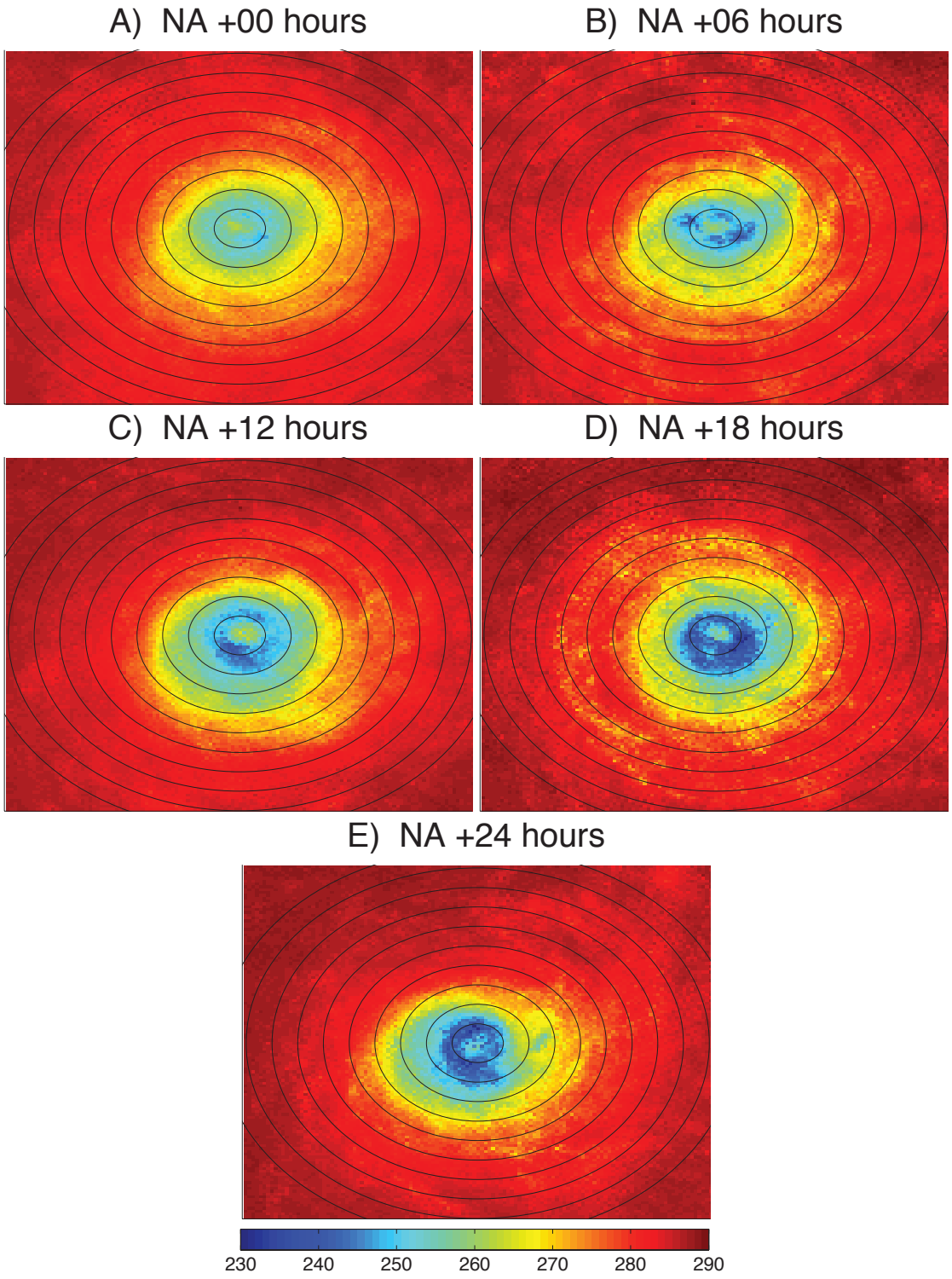

Figure 53: As in Figure 45, except for the North Atlantic.

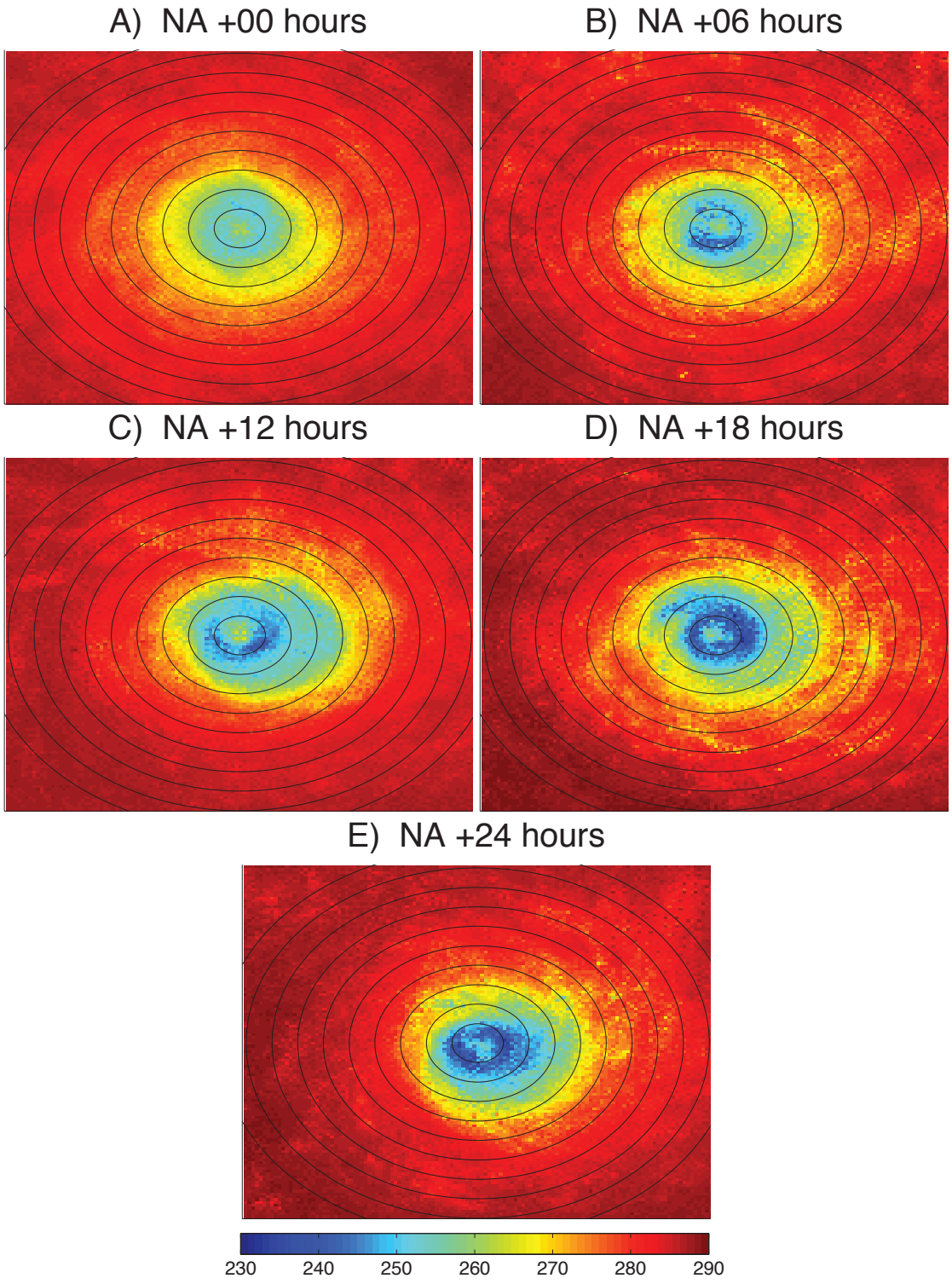

Figure 54: As in Figure 45, except for the North Atlantic in a shear-relative coordinate system. Shear vector is oriented towards the top of the page.

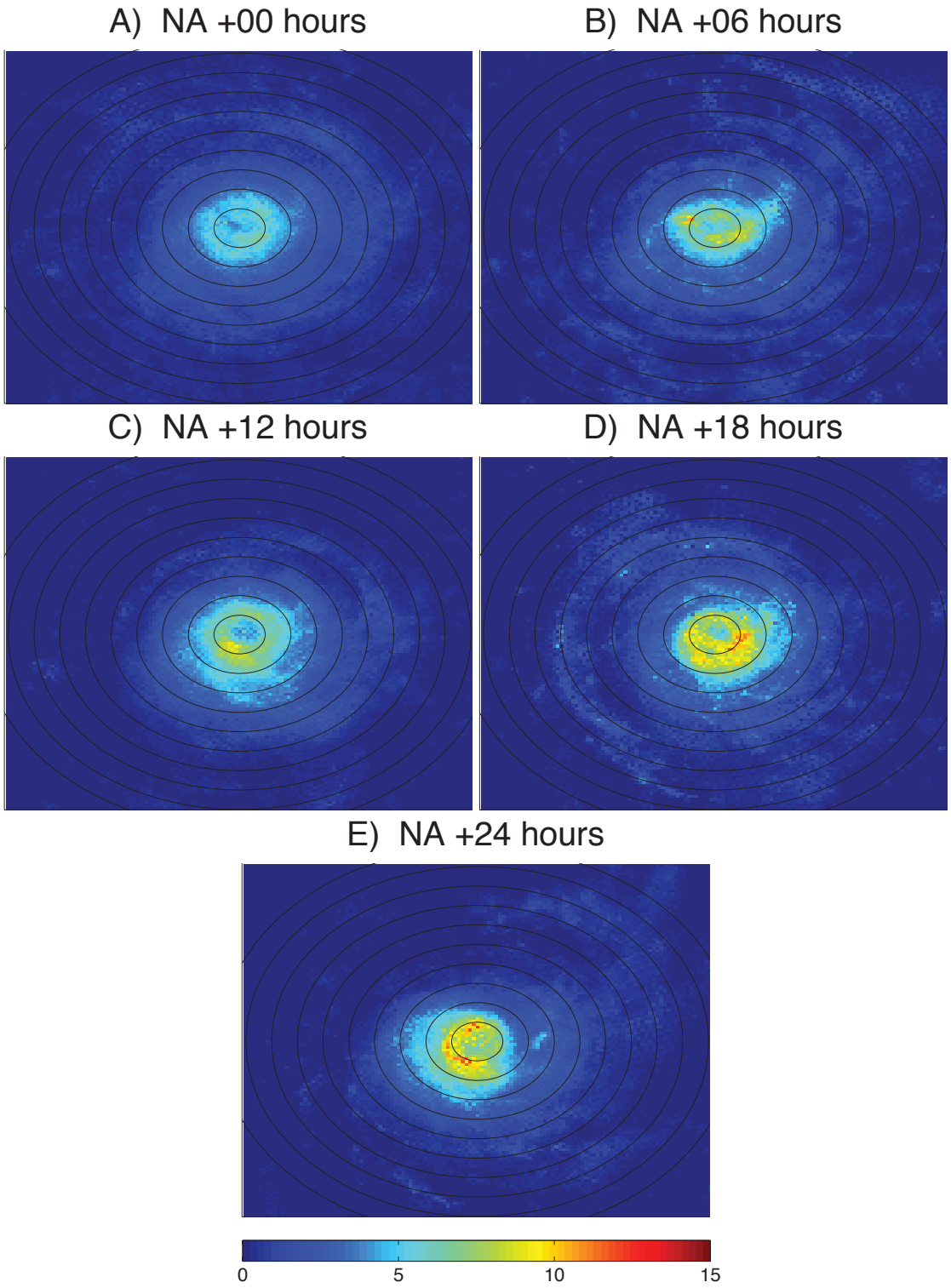

Figure 55: As in Figure 45, except rain rates (mm/hr) for the North Atlantic.

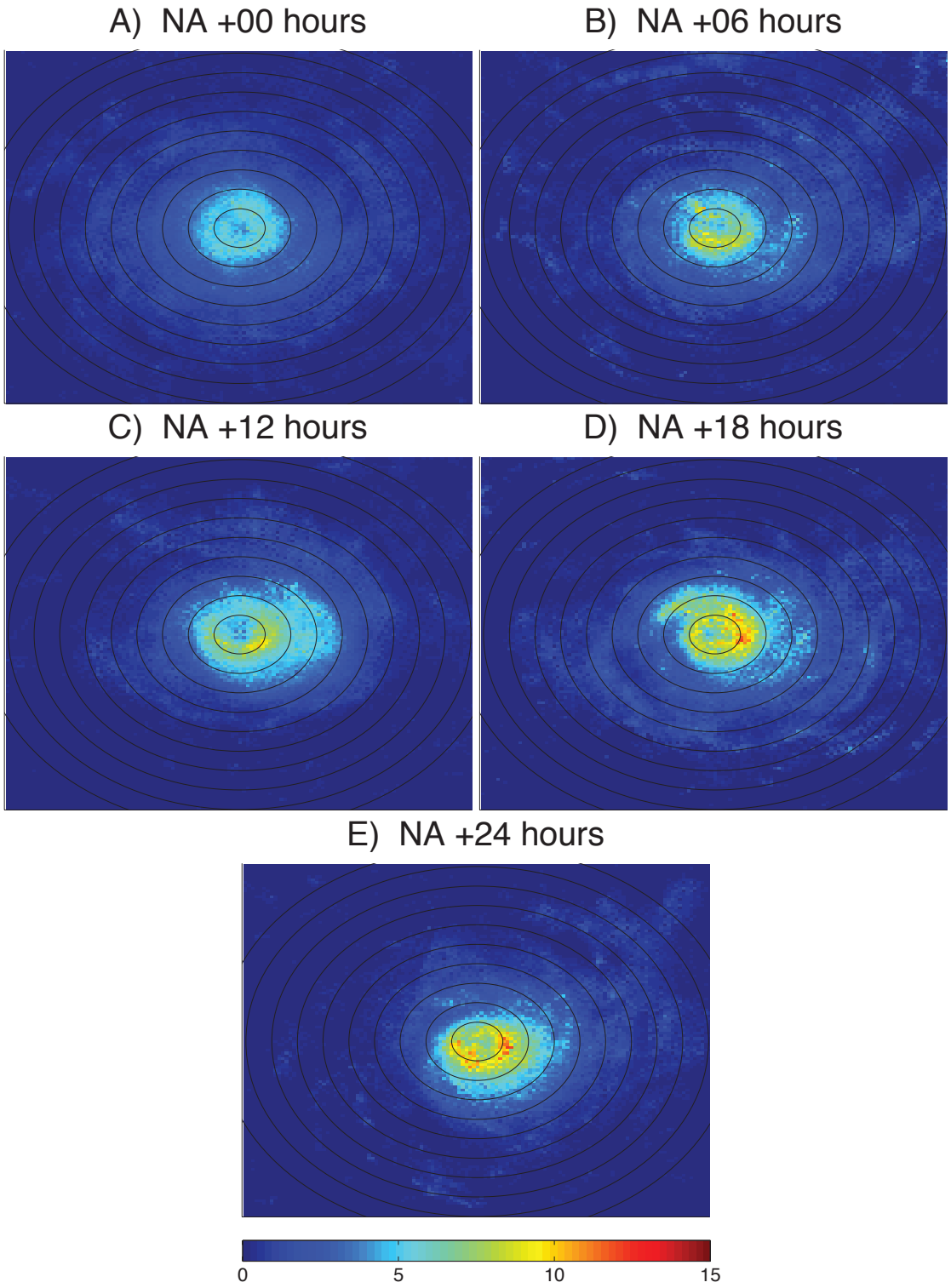

Figure 56: As in Figure 45, except rain rates (mm/hr) for the North Atlantic in a shear-relative coordinate system. Shear vector is oriented towards the top of the page.

The South Indian basin composites (Fig. 57-61) display a much different perspective of RI, with the development and intensification of an eyewall which contracts to show a pinhole eye in the composites 24 hours after initiation. Storm-relative 85 GHz PCTs are initially minimized in the eyewall to the front of the system (Fig. 57a) and begin filling in counterclockwise before a distinct ring of < 245 K convection encircles the core 12 hours later (Fig. 57c). Over the final 12 hours of RI the eyewall intensifies and contracts eventually forming the pinhole eye at the end of the RI cycle, with maximum ice scattering occurring to the front left of the storm motion (Fig. 57e). The shear-relative plots are nearly identical, with the PCTs at a minimum downshear initially (Fig. 58a) and fully encompassing the eye by 12 hours (Fig. 58c) followed by the pinhole eye development as the convection intensifies and consolidates around the core (Fig. 58e).

Rain rate composites for the South Indian Ocean depict an initial convective maxima of 9-11 mm/hr to the front of storm-motion and downshear, embedded in a ring of more shallow convection with rates of 5-7 mm/hr (Fig. 59a, 60a). At 12 hours this ring has intensified to a consistent value of 9 mm/hr at around 55 km from the storm center, with embedded maxima remaining to the front and downshear (Fig. 59c, 60c). By the 24-hour period in the RI lifespan the pinhole eye has formed with rain rates there of 6 mm/hr surrounded by rain rates of 13 and 14 mm/hr on all sides (Fig. 59e, 60e). The convection here overall is much more symmetric throughout the process than the East Pacific with a smaller eye seen at the conclusion of RI than either of the prior basins.

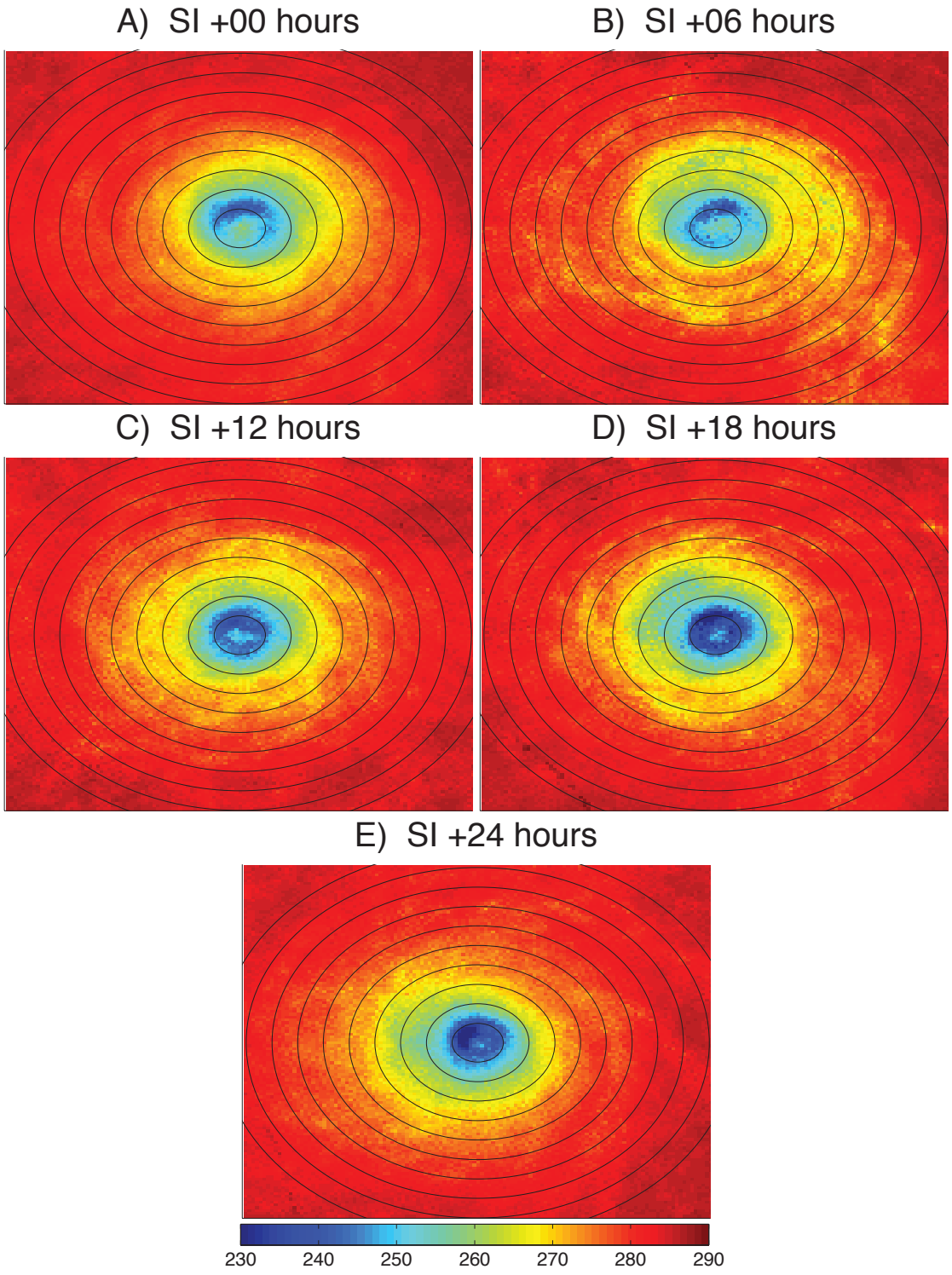

Figure 57: As in Figure 45, except for the South Indian basin.

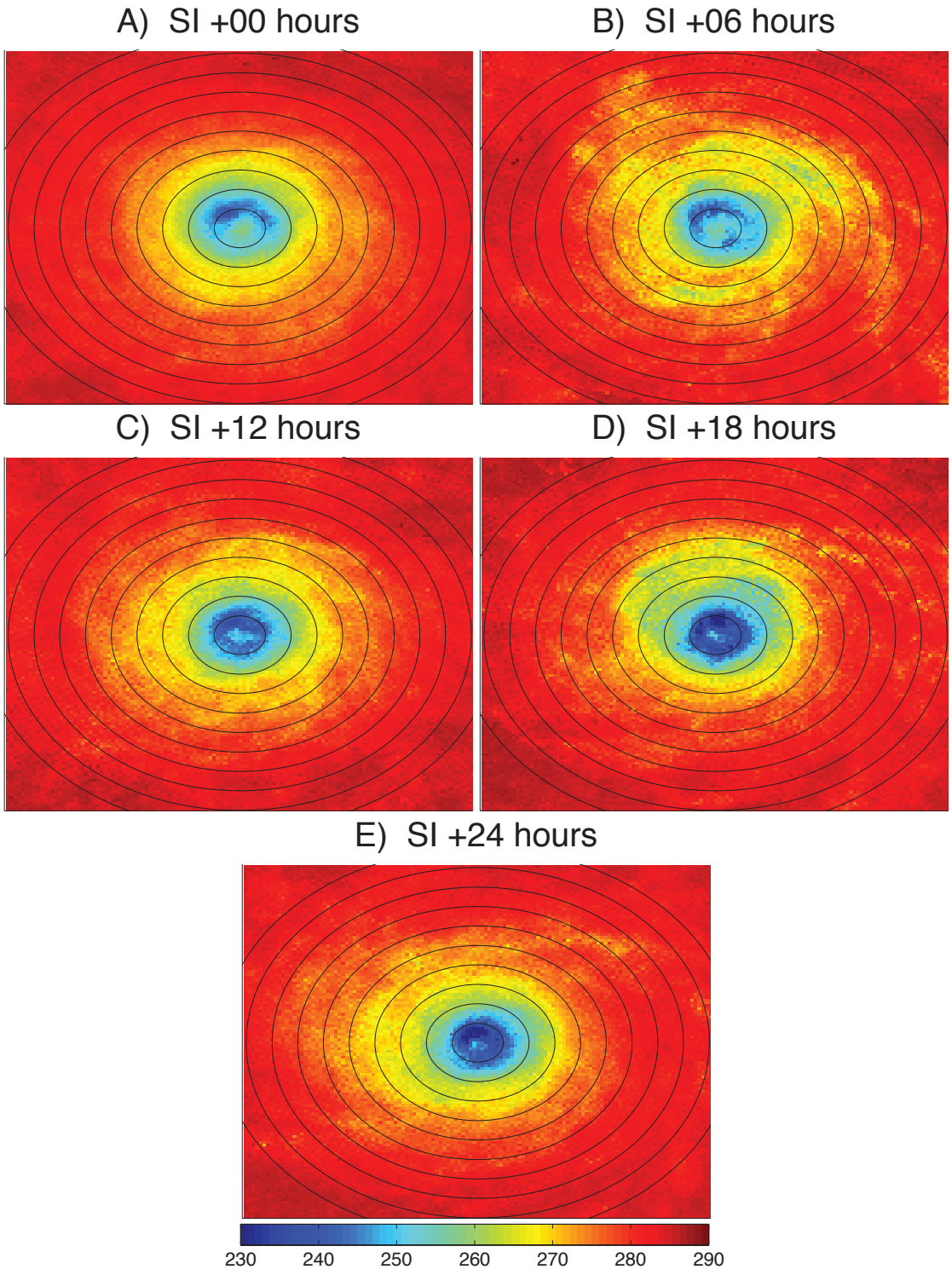

Figure 58: As in Figure 45, except for the South Indian in a shear-relative coordinate system. Shear vector is oriented towards the top of the page.

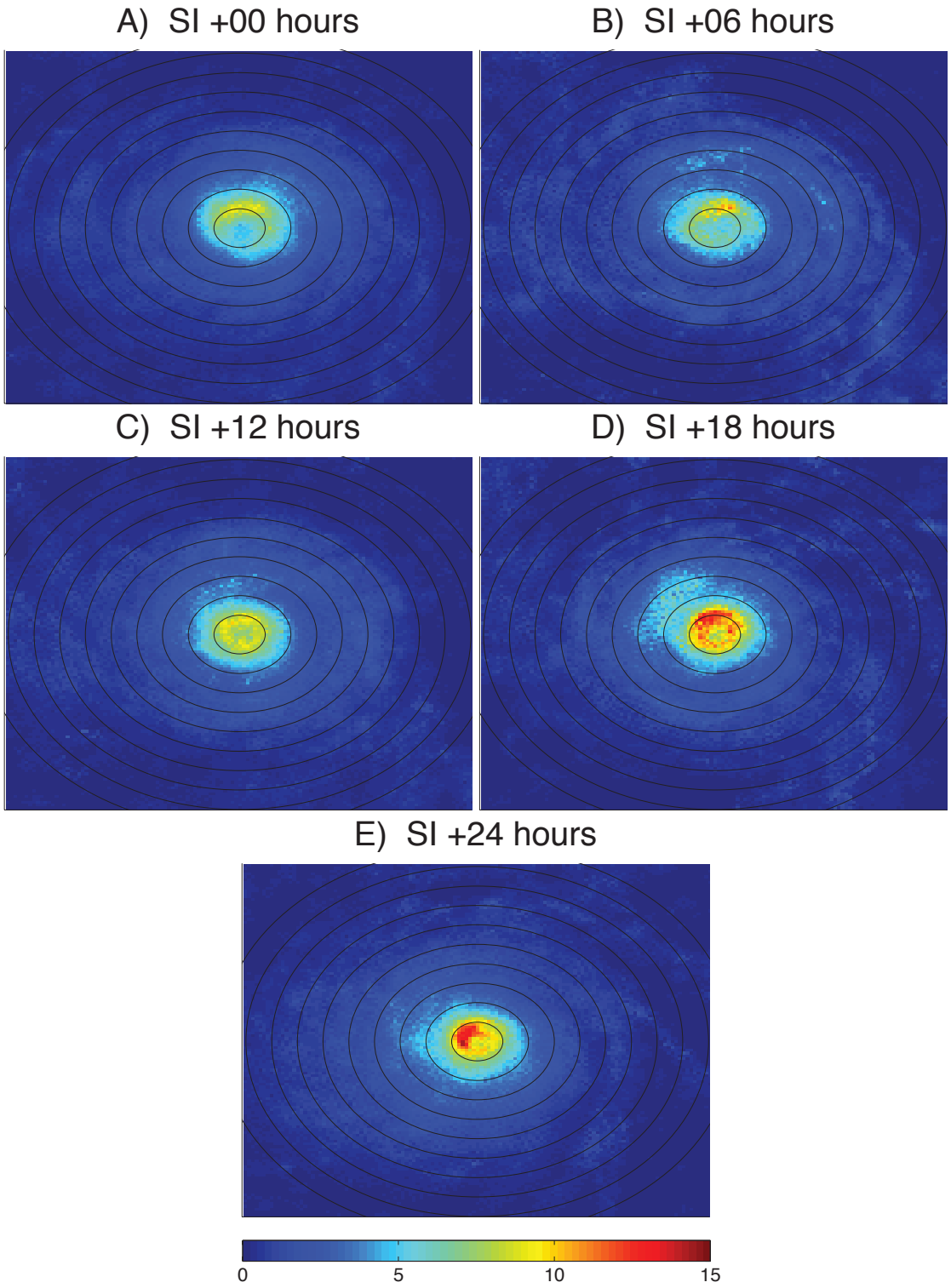

Figure 59: As in Figure 45, except rain rates (mm/hr) for the South Indian.

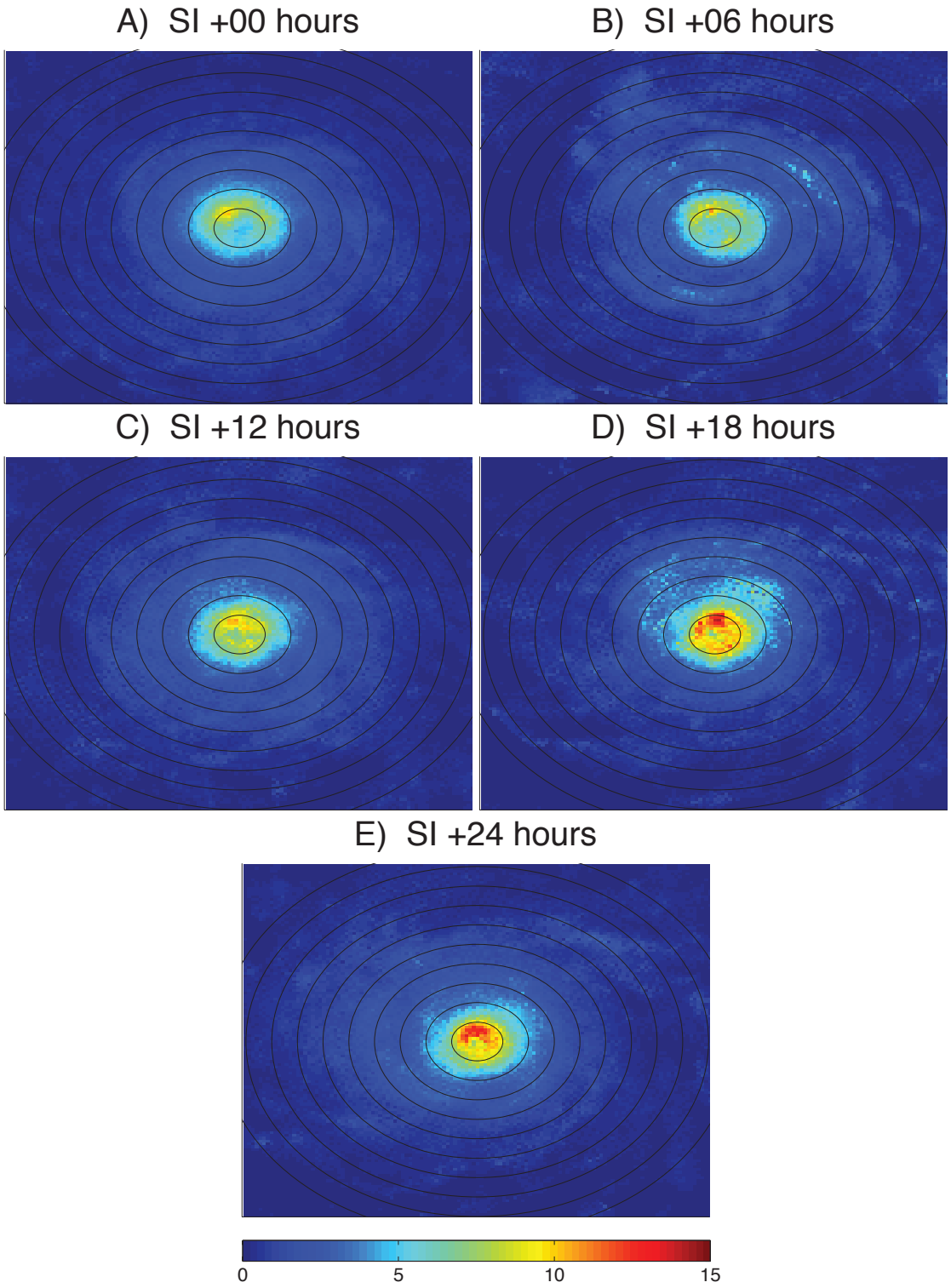

Figure 60: As in Figure 45, except rain rates (mm/hr) for the South Indian in a shear-relative coordinate system. Shear vector is oriented towards the top of the page.

The South Pacific composites provide the most striking and rapid evolution of deep convection in the eyewall with no hint of an eye by the 24-hour period of the RI cycle (Fig. 61-64). In the storm-relative composite a ring of 245 K PCTs exists 50 km from the core, fully encompassing the eye (Fig. 61a). Just 6 hours later this convection has intensified, with PCTs below 240 K surrounding the eye with a region of near 230 K to the rear of the system (Fig. 61b). After another 6 hours the convection has weakened slightly but still has a widespread area below 240 K (Fig. 61c). By 18 hours after the initiation of RI (Fig. 61d) the ice scattering signal in the eyewall has contracted with the eye being only 15-20 km wide and eventually disappears entirely at the 24 hour mark (Fig. 61e) with the 55 km annuli nearly fully filled with brightness temperatures below 245 K and numerous regions below 235K. The shear-relative composite is close to identical, with the most notable difference being the convective ring at the start of RI being weak in the upshear left quadrant (Fig. 62a).

The rain rate storm-relative composite at inception of RI has a ring of precipitation at 7-9 mm/hr rates surrounding the core (Fig. 63a). At the next stage this convection has intensified with rates approaching 15 mm/hr covering the rear portion of the storm and much of the eyewall possessing rainfall above 9 mm/hr (Fig. 63b). At 12 hours the eyewall has weakened but become more axisymmetric with rain rates of 9 mm/hr at a radius of 55 km (Fig. 63c). The convective activity has re-intensified by the 18-hour mark, this time to the front of the system with rates of 13 mm/hr over a wide area (Fig. 63d). By this point in time the eye is hardly distinguishable, and is replaced with rain rates once more approaching 15 mm/hr at the finale of RI. In the shear-relative system the upshear left eyewall is weaker over the first 6 hours (Fig. 64a, b) before becoming better defined at 12

and 18 hours (Fig. 64c, d). As RI completes an eye is no longer present with widespread rain rates of 11 to 14 mm/hr within the innermost ½° (Fig. 64e).

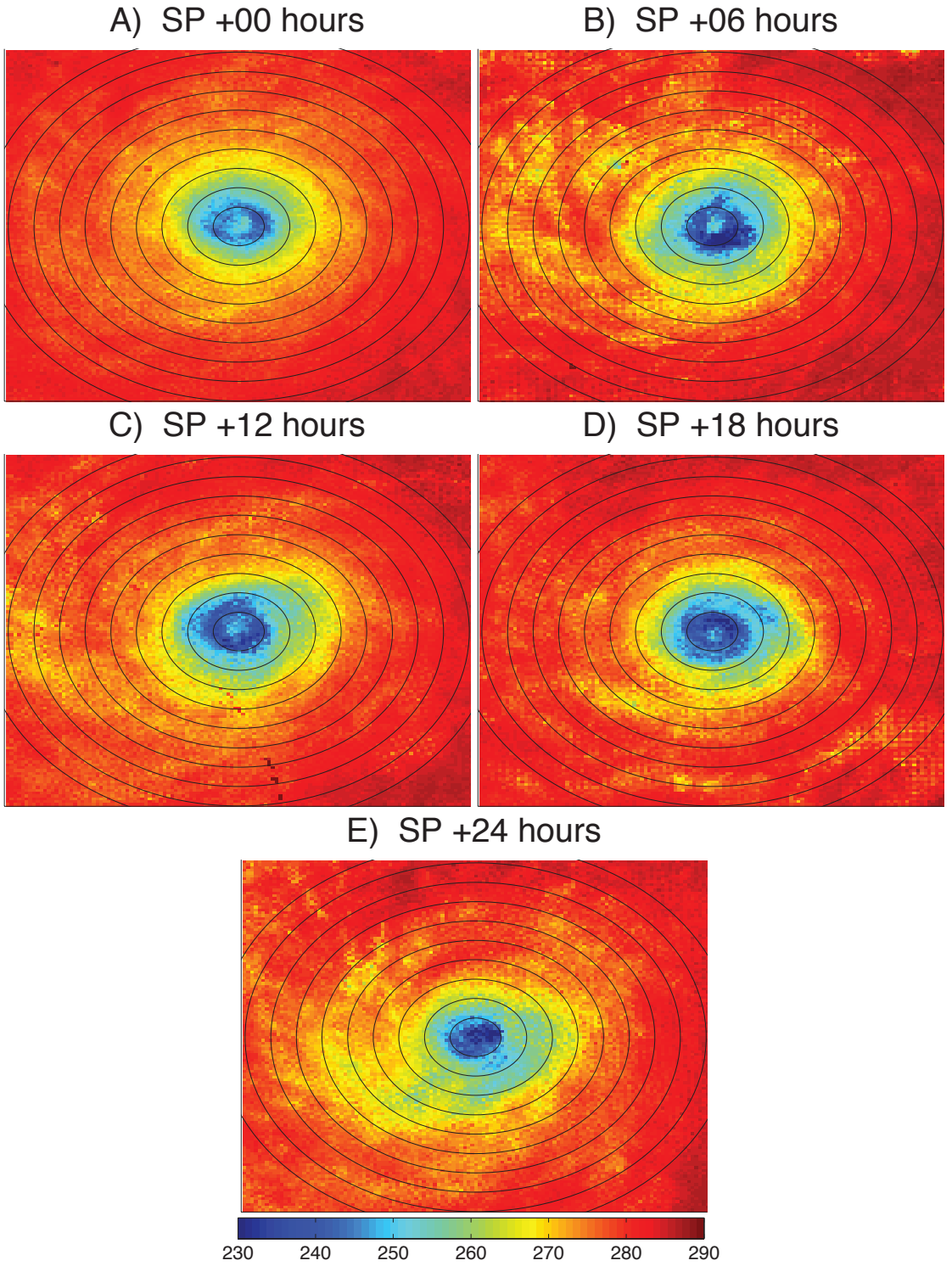

Figure 61: As in Figure 45, except for South Pacific.

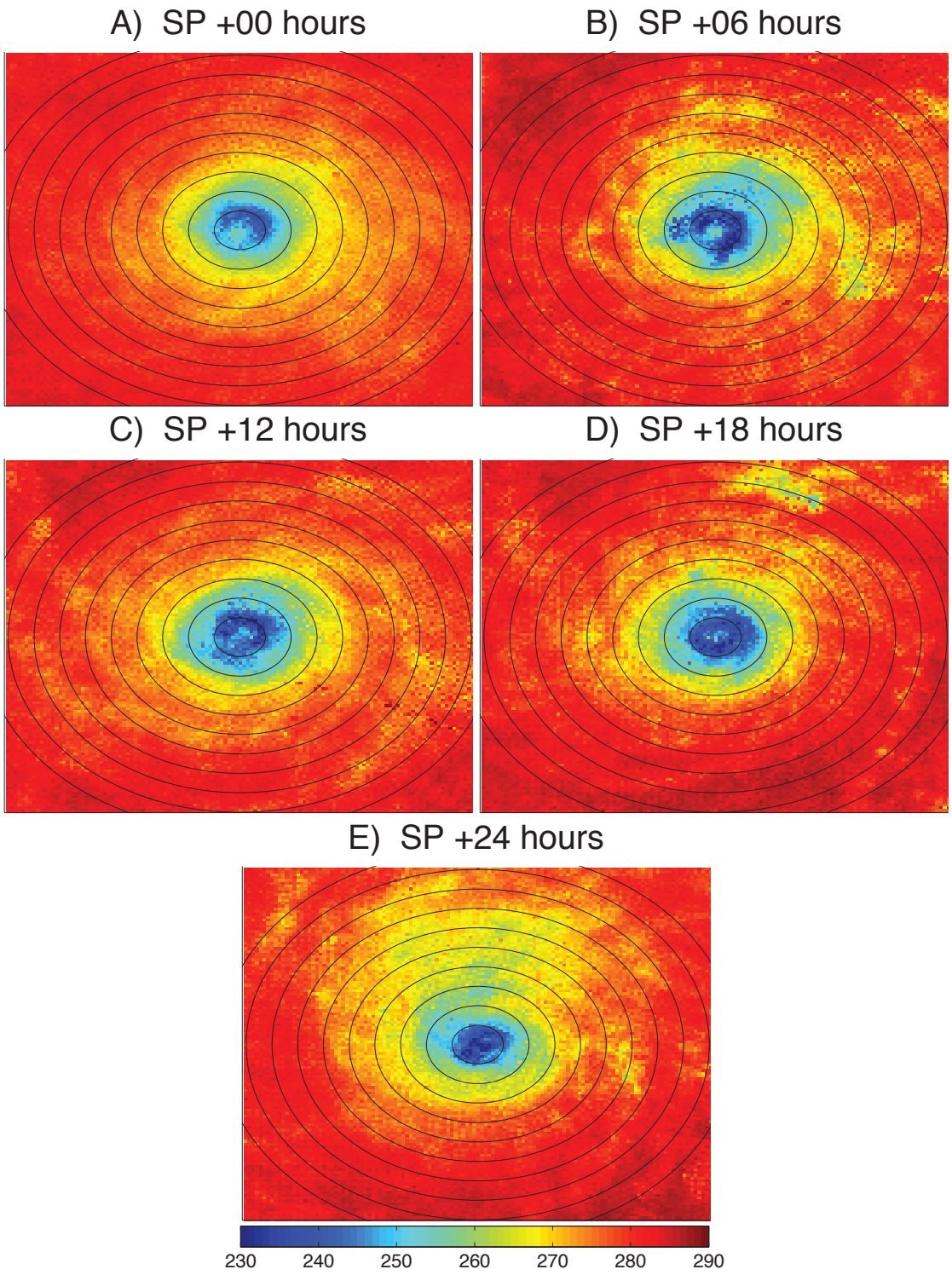

Figure 62: As in Figure 45, except for South Pacific in a shear-relative coordinate system. Shear vector is oriented towards the top of the page.

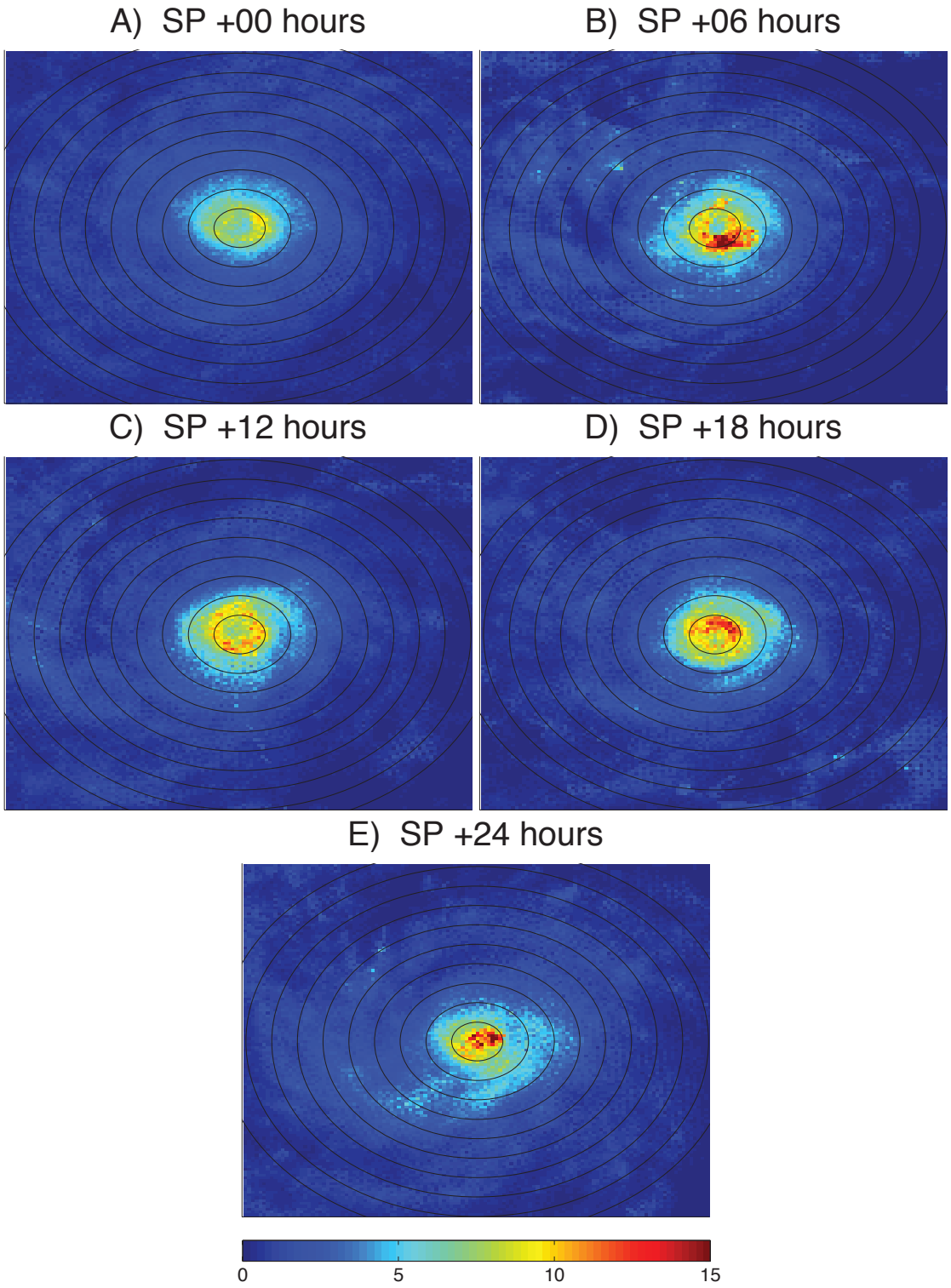

Figure 63: As in Figure 45, except rain rates (mm/hr) for South Pacific.

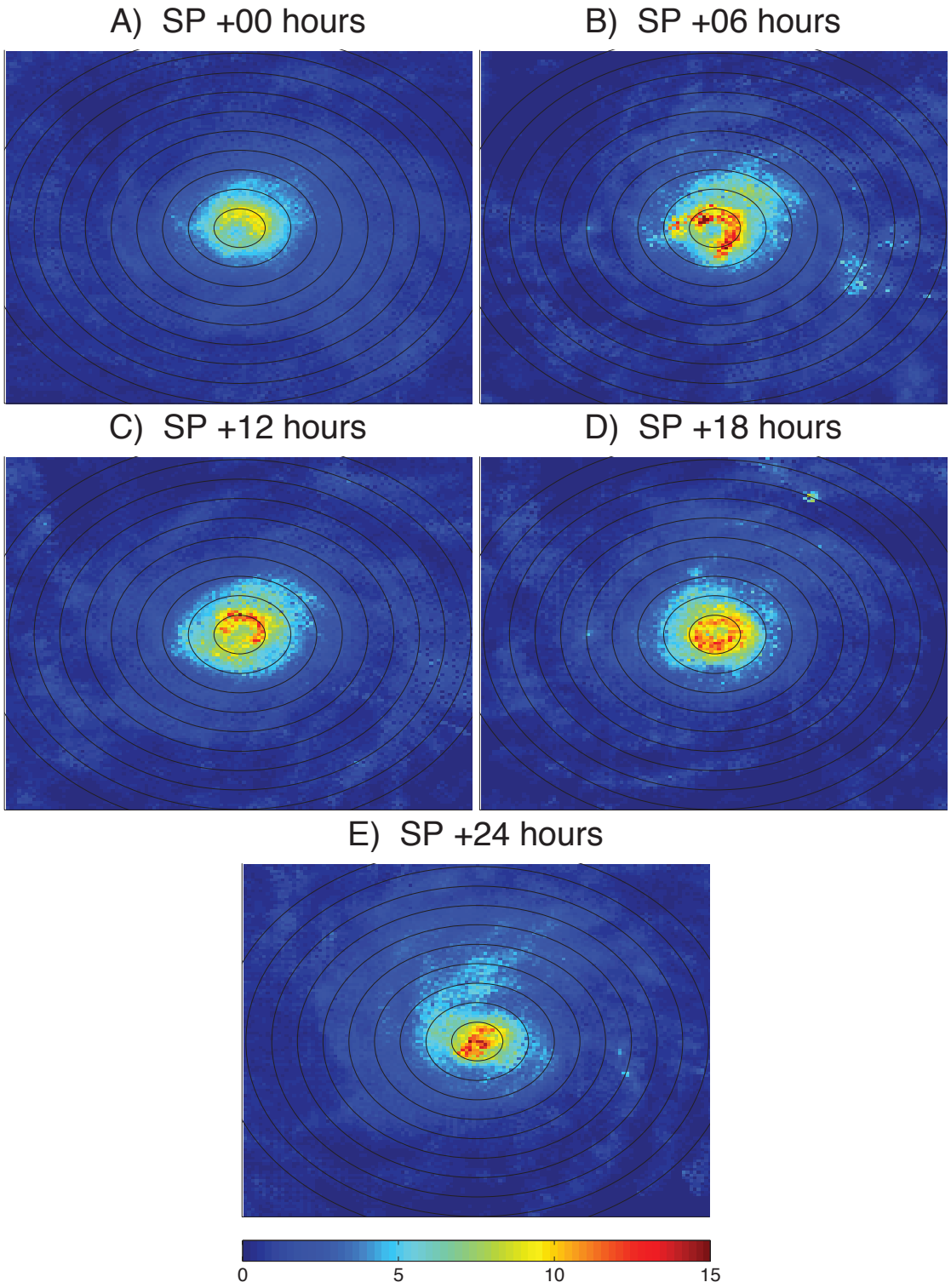

Figure 64: As in Figure 45, except rain rates (mm/hr) for South Pacific in a shear-relative coordinate system. Shear vector is oriented towards the top of the page.

Last is the West Pacific basin, which, in a composite sense, has a pronounced eyewall initially, however a somewhat muddled transitional structure before a small eye becomes evident late in the RI life cycle (Fig. 65-68). The 85 GHz PCT composites show a distinct circular eyewall just inside 55 km in both coordinate systems (Fig. 65a, 66a). At 6 hours after RI begins however, these are not apparent in the composites as the innermost ½° is filled with the majority of pixels < 245 K (Fig. 65b, 66b). After another 6 hours the smallest annuli region has seen its ice-scattering increase with many pixels < 240 K but the hint of an eye returns, centered in the storm-relative composite (Fig. 65c) and slightly downshear-left in the shear-relative composite (Fig. 66c). In the storm-relative plots the eye becomes better defined for 18 (Fig. 65d) and 24 hours (Fig. 65e) after RI begins while it remains relatively ambiguous in the shear-relative composites (Fig. 66d, e). In each of these coordinate systems the maximum convective intensity and ice-scattering signature in the eyewall is at 18 hours (Fig. 65d, 66d), not 24.

Rain rates show similar behavior to that seen in the ice-scattering composites. A nearly complete eyewall with voids to the left of storm motion and shear contains of precipitation rates around 7 mm/hr as RI is initiated (Fig. 67a, 68a). Moving forward six hours the eyewall becomes distorted with no eye apparent in either coordinates (Fig. 67b, 68b). Ill-defined eyes return for the remainder of the evolution composites in each coordinate system (Fig. 67c-e, 68c-e) with the maximum in eyewall precipitation rates occurring at 18 hours after RI ensues. This maxima occurs with 11-13 mm/hr rain rates to the right of storm-motion (Fig. 67d) and 11-14 mm/hr rain rates downshear (Fig. 68d).

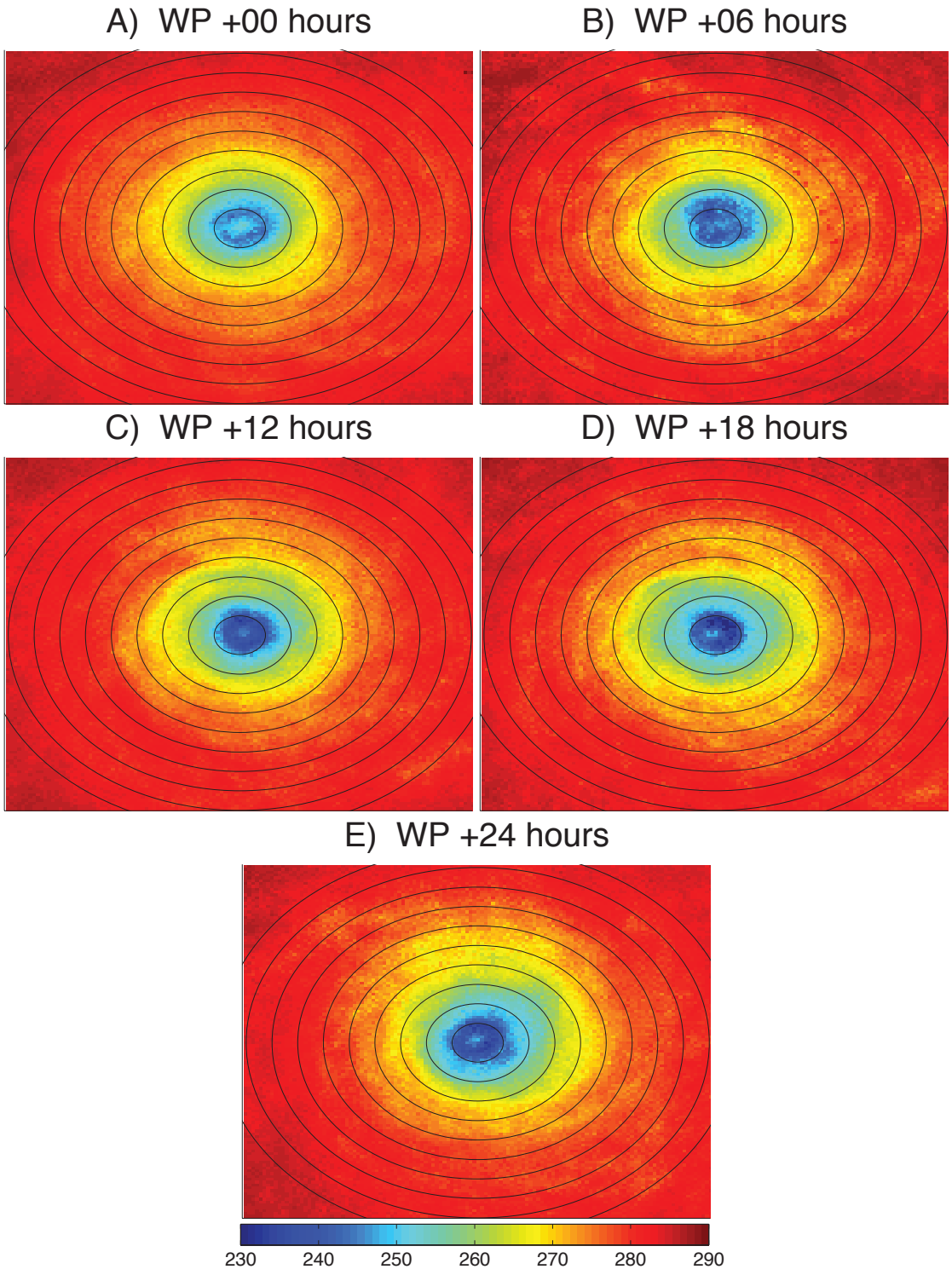

Figure 65: As in Figure 45, except for the West Pacific.

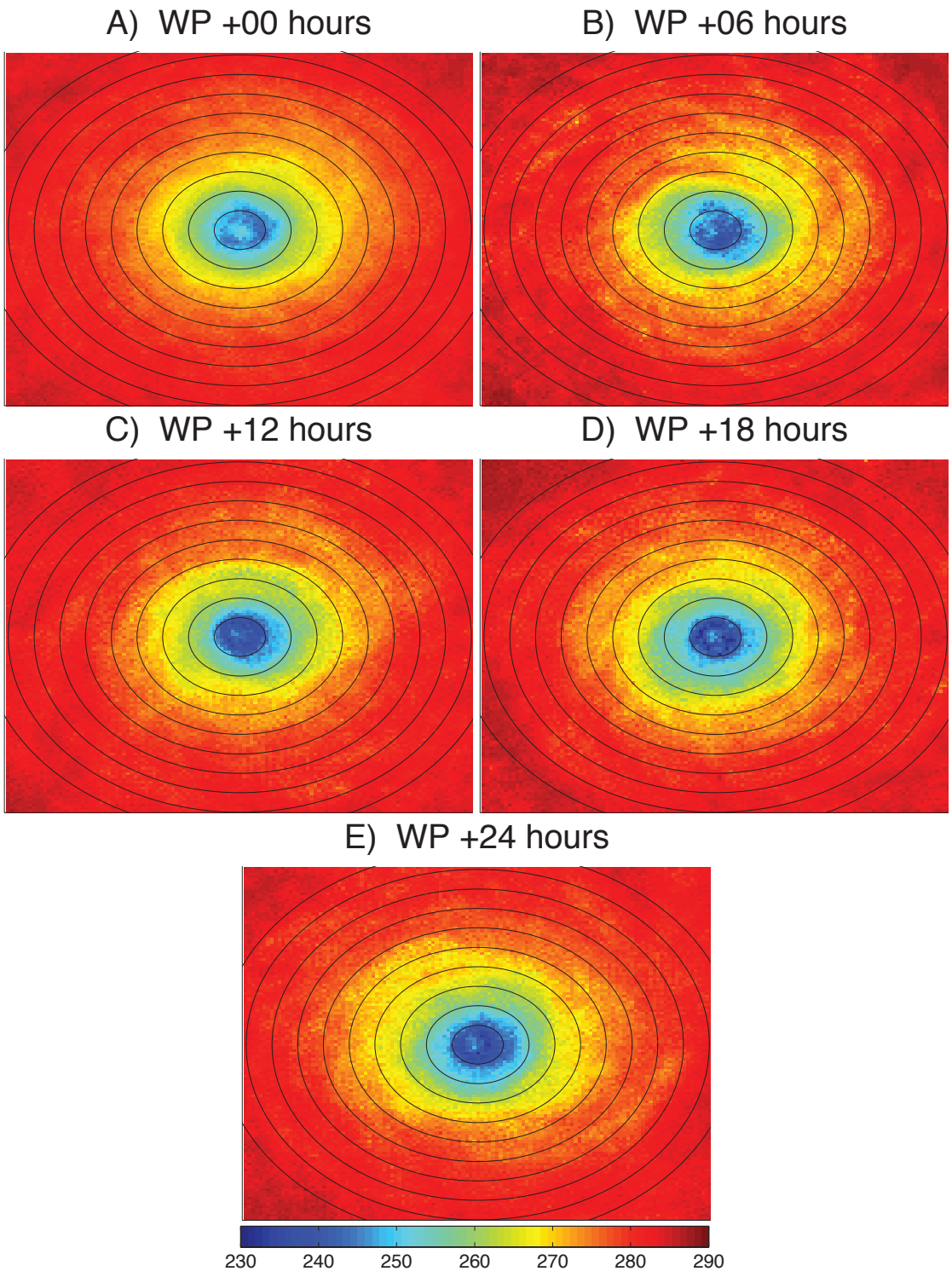

Figure 66: As in Figure 45, except for the West Pacific in a shear-relative coordinate system. Shear vector is oriented towards the top of the page.

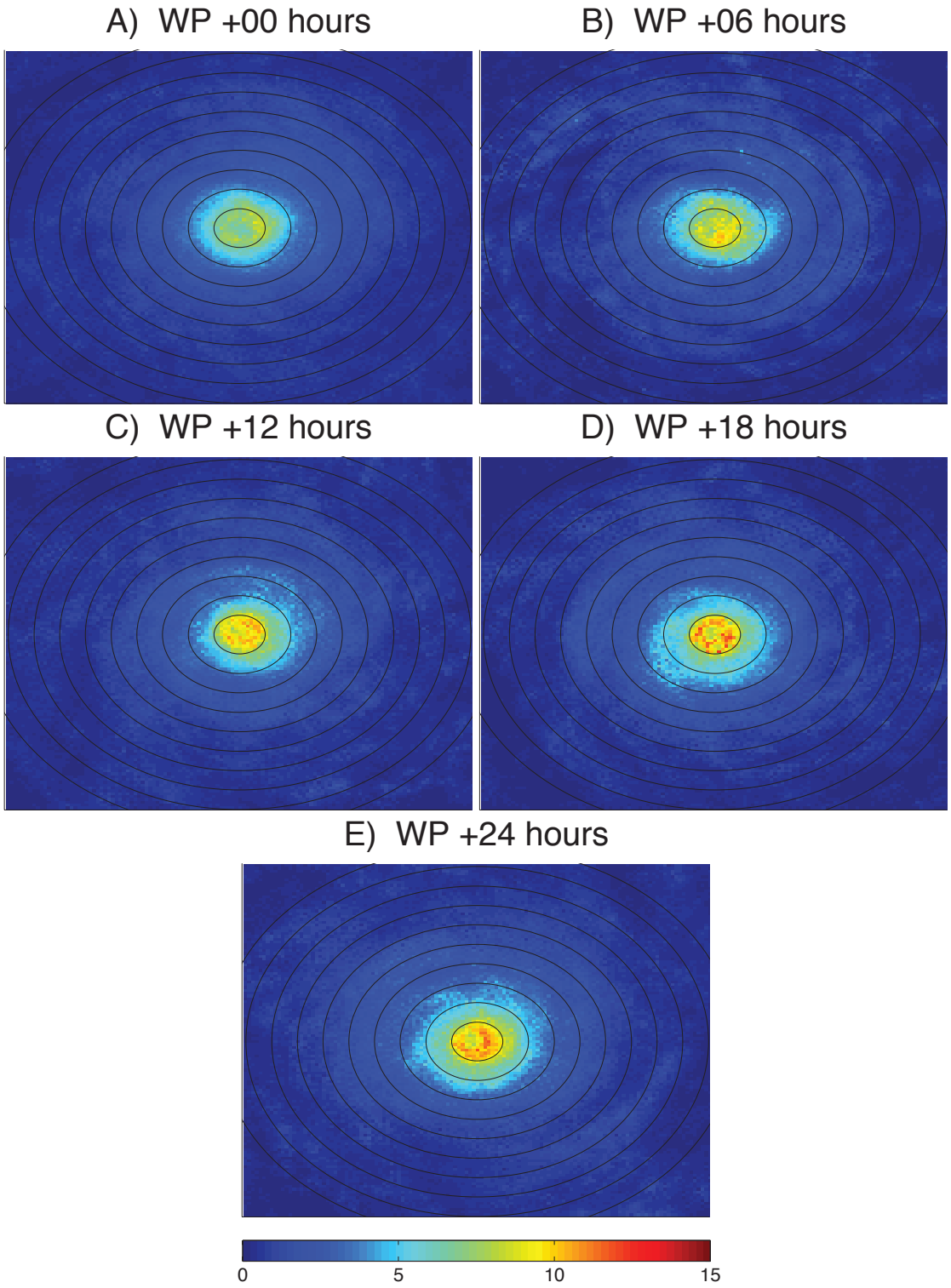

Figure 67: As in Figure 45, except rain rates (mm/hr) for the West Pacific.

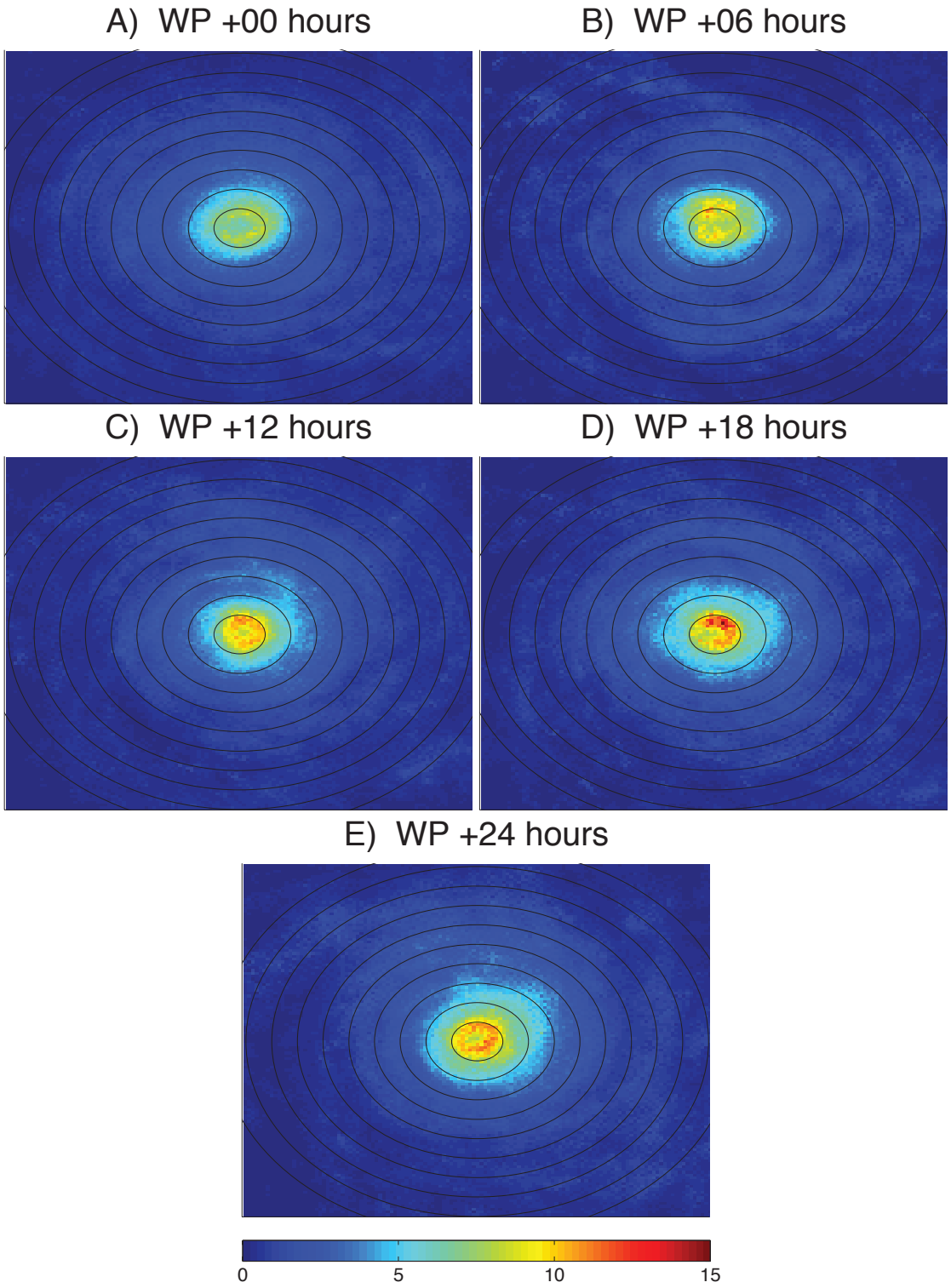

Figure 68: As in Figure 45, except rain rates (mm/hr) for the West Pacific in a shear-relative coordinate system. Shear vector is oriented towards the top of the page.

To evaluate the importance of axisymmetry and isolated convective bursts further in terms of cause and effect in RI, the area below 85 GHz PCT bins at 10 K intervals from 200-250 K is examined. Similar to the evolution composite plots, for each individual overpass of a storm at any point during RI its below each PCT threshold were calculated, summed, and normalized averages produced of the area for each bin as a function of radius with the results shown in Figure 69.

One somewhat surprising feature is the difference between the 18 and 24-hour areas for each threshold is < 1% at radii of 55 and 110 km. This exhibits that the widely used 24 hour period may not be best suited for determining RI, with most of the structural changes in microwave structure taking place on an 18-hour time scale. Utilizing area < 200 K as a proxy for convective burst shows that the majority of the increase in area occurs over the second half of the lifecycle, suggesting that bursts are primarily an effect during RI (Fig. 69f). Meanwhile twice as much increase is seen in 85 GHz area below 250 K (Fig. 69a) and 240 K (Fig. 69b) over the first half of the RI cycle, lending to the importance of areal coverage of moderate ice-scattering in the formative stages of RI. The large percentages of PCTs below 250 K even at the initiation of RI also help to reinforce this position.

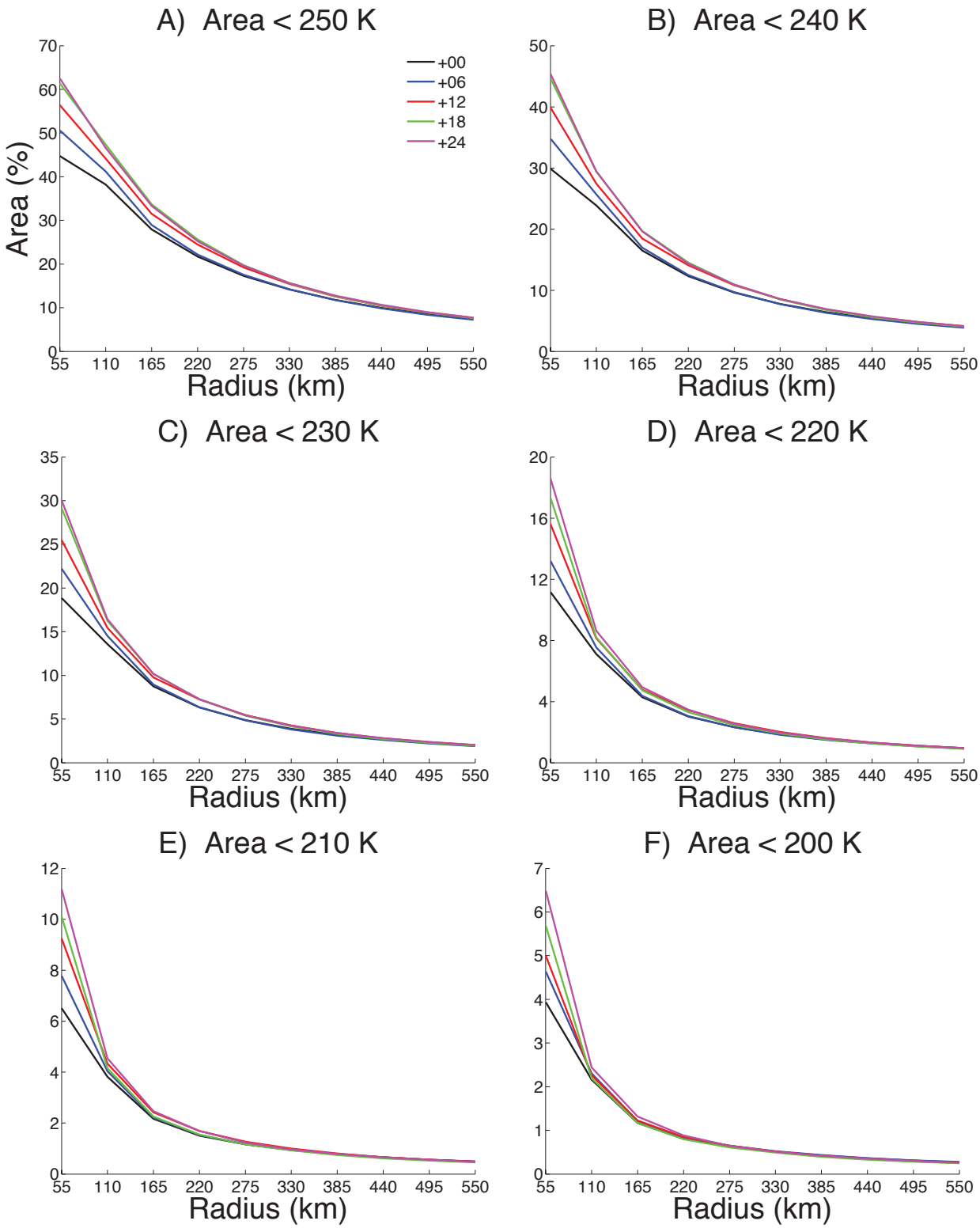

Figure 69: Percentage 85 GHz PCT area at 6-hour intervals during period of rapid intensification as a function of radii for (a) < 250 K, (b) < 240 K, (c) < 230 K, (d) < 220 K, (e) < 210 K, (f) < 200 K.

CHAPTER 4

CONCLUSIONS

This thesis has focused on the use of SSM/I and TMI data over the past two plus decades to examine the feasibility of prediction of TC intensity and intensity change. The expansive dataset dwarfs prior PM studies of TCs and with its unique framework of interpolated brightness temperatures across sensors and channels to a common resolution presents an unprecedented view of TC structure.

High frequency PM channels of 85 and 37 GHz as well as a multichannel algorithm combining scattering and emission signals into a rain rate approximation are evaluated via azimuth and annuli utilizing common statistics including: mean, median, minimum (or maximum for rain rate), 75th percentile, 90th percentile, 95th percentile, 99th percentile, and 99.9th percentile. These values are used in the context of best track intensity and intensity change over the period up to 36 hours after the initial satellite overpass in order to examine potential links between the microphysical information shown in the PM overpass and the resultant intensity variation. The complexities of TC intensity change are displayed, especially in cases of RI, however the prospect exists for morphological recognition for intensity change as opposed to basic statistical methods.

Correlation between brightness temperature statistics taken within 1.5° or less of the TC core show promise in prediction of both current and future system intensity. More extreme brightness temperature and rain rate statistics such as percentiles $\geq$ 90% performed poorly throughout compared to metrics evaluating the larger scale state of the TC inner core such as the median. Accordingly, as noted in Cecil and Zipser (1999), it is

deemed that the spatial coverage of convection appears more closely linked to intensity change than localized, intense convective activity. Statistics for the 85 and 37 GHz frequencies and rain rate metric examined here perform slightly less skillful for observed intensity as the 10 and 19 GHz values utilized by Hoshino and Nakazawa (2007), although this may well be a byproduct of their smaller sample size of under 1000 overpasses. With these statistics increased skill is consistently seen for periods of up to 24-hours following the overpass itself, lending credence to a lag between latent heat release from ice processes within convective activity and the resultant intensity change.

Attempts to correlate brightness temperature variables with intensity change values did not prove to be as skillful, however definite relationships appear to exist, especially on a scale of up to 12 hours. The relationships contain a large amount of scatter, and perform worst for storms weakening suddenly (often with signatures suggesting the TC making landfall) and for storms undergoing RI. It is believed that in both of these cases one error source is the intensity estimates themselves, as in situ observation is only common in the North Atlantic and the Dvorak method's satellite usage being the norm elsewhere. Another potential shortcoming is the inability of the simple parameters utilized in the study to resolve the important signature of the eyewall (either developing initially for storms undergoing RI or replacement cycles for those with rapid weakening). For simplistic detection of these eyewall structures other methods such as the automatic eye-detection algorithm in ARCHER (Wimmers and Velden, 2010) may be more ideal in these situations. Linear regression schemes of multiple variables (both passive microwave and environmental) such as is utilized in SHIPS-MI (Jones et al., 2006) may also prove to be more skillful.

The distributions of brightness temperature parameters amongst varying intensity change classes were analyzed, with a clear distinction seen between storms undergoing RI and those that do not. Distributions of median 85 GHz PCTs and rain rates showed a larger spatial signal of light to moderate convective activity present for storms beginning RI. For parameters that depict more extreme convective values, such as area below high ice-scatter thresholds and percentiles $\geq$ 90% the differences between the distributions are much smaller. Both of these act to show the importance of a large spatial contribution of weak to moderate convective activity surrounding the TC core as RI is initiated. It also depicts the lack of influence of convective bursts in the initiation of RI, and importance of axisymmetry to some extent.

As one would expect, intensifying storms had the closest signature to those beginning RI however some separation between the distributions was apparent. Meanwhile, storms that were steady state and weakening had distributions consistently possessing similar peaks and values and which were offset from the RI and intensifying distributions. This further underscores the prediction potential that may be possible in the future through utilizing of means other than the basic statistics utilized here, with the well-defined separation observed of the two classes intensifying systems to those that were not. Additionally, variance in storm structure and intensity was also observed across the different oceanic basins as expected, with the weakest signal between RI systems and nonRI TCs consistently seen in the North Atlantic. It is believed this is a byproduct of the direct aircraft reconnaissance occurring in this basin whereas the Dvorak analyses in other basins have a tendency to bias the storm intensity, however more analysis is necessary in this area.

In contrast to the differentiations seen at 85 GHz and through rain rates, a recurring theme throughout was the shortcomings of 37 GHz PCTs to depict TC structure in general through PCT gradients, and in particular delineate between storms undergoing varying states of intensity change. As for the source of this lack of information, Figure 70 depicts Hurricane Katrina (2005) as a Category 5 storm with pronounced structure. Rain rates in Figure 70a depict a mature eyewall with some values in excess of 40 mm/hr in addition to a developing secondary eyewall with rates of 15-20 mm/hr. These regions correspond to depressed 85 GHz PCT values of below 150 K in the eyewall and 200 K for the secondary eyewall (Fig. 70b). With the focus shifting to 37 GHz, the PCT field (Fig. 70c) depicts an eyewall with values of only around 260 K, with the secondary eyewall possessing similar values.

At 37 GHz emission by liquid hydrometeors and scatter by large (roughly > 8 mm) cloud ice in addition to the ambient background are the key variables of brightness temperature (McGaughey et al., 1996). To compensate for variable background radiation and capture the emission signature, the polarization difference at low frequency microwave channels has been noted to be a proxy for emission by atmospheric water (Liu and Curry, 1998). This is a byproduct of the strong emission by liquid hydrometeors as opposed to the highly polarized ocean surface, such that difference values closer to 0 are more representative of strong atmospheric emission/scattering. Differences at 37 GHz in the core region are highest in the area of the moat (Fig. 70d) aside from within the eye itself. The regions of deepest convection within the eyewall and developing secondary eyewall have difference values on the order of 5 K, with this difference likely a byproduct of the scatter by graupel. The individual 37 GHz vertical (Fig. 70e) and horizontal (Fig. 70f)

appear strikingly similar throughout the precipitating region of the overpass, as indicated in their difference (Fig. 70d), however over the cloud-free regions the ocean brightness temperatures are around 230 K in the vertical and 170 K in the horizontal. Entering these two approximate values results in a realistic SST for the Gulf of Mexico in late August of 29°C. The nature of the polarization correction however, depicts brightness temperature depressions, despite the ocean being consistently the coldest feature in each of the individual channels, negating the influence of emission in the corrected metric. Due to the modest updrafts observed in even intense tropical cyclones (Jorgensen et al., 1985) a relatively small amount of graupel and larger cloud ice exists to depress the 37 GHz PCT field. The individual 37 GHz polarizations may hold promise for TC prediction at early stages of development, however at later stages in the lifecycle the tendency of the 37 GHz temperatures to saturate at rain rates above 3-6 mm/hr presents a hurdle (McGaughey et al., 1996).

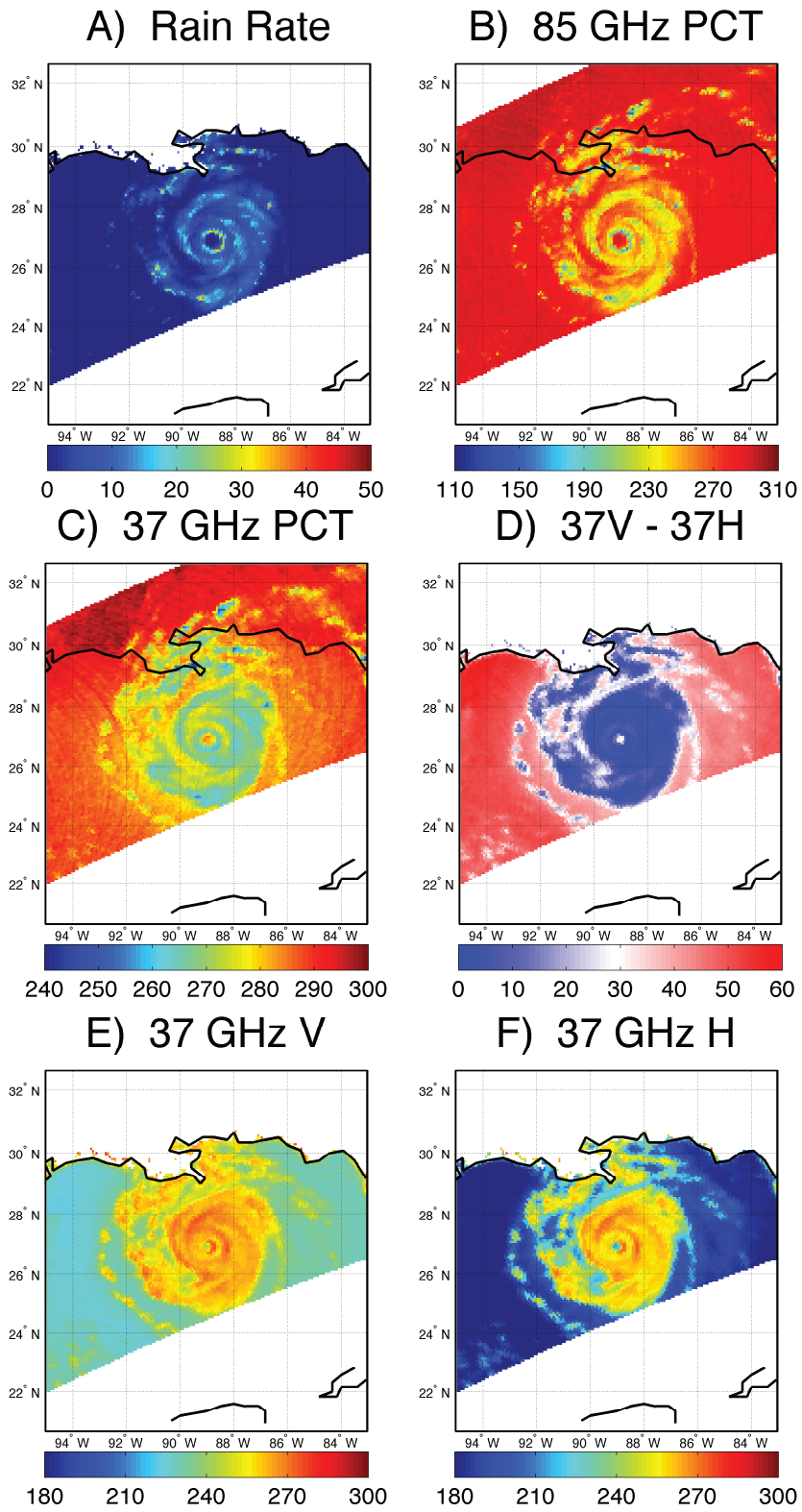

Figure 70: TMI overpass of Hurricane Katrina at 2133 UTC on 28 August 2005 depicting (a) rain rate (mm/hr) (b) 85 GHz PCT (K) (c) 37 GHz PCT (K) (d) 37 GHz polarization difference (K) (e) 37 GHz vertical polarization (K) (f) 37 GHz horizontal polarization (K).

With the promise seen in the 85 GHz PCT and rain rate results the evolution of RI over the 24 hours following its initiation were examined in the form of composites made of individual overpasses. A prominent ring feature with values indicative of modest convection (240-250 K 85 GHz PCTs and 7-8 mm/hr rain rates) is apparent at the time of RI initiation with a radius of 40-75 km from the storm center. This feature is not evident in any of the other intensity change classifications. A hint of a ring is evident in each of the other classifications however the gradient in the brightness temperature field is not near that seen in the RI subset. These annular structures are likely a byproduct of well-developed intense eyewalls and eyes in mature hurricanes that are biasing the composites in this manner. Evaluation of standard deviations of individual grid points rotated for storm-motion or shear vector orientation for the composites notes relatively small values within the ring structure region for the RI systems, suggesting that convective bursts and other extreme brightness temperature values are not present, with the spatial coverage of convective activity being a superior indicator of intensity change.

With the distinctions noted between the RI systems and other intensity changes, composites were made of this class over the 24-hour period following the initial overpass. In these a consistent pattern is noted of the intensification of the annular convective structure and its contraction with time. The process appears to be largely similar across oceanic basins over the first 18 hours, with the strongest brightness temperature signatures also seen at this point, suggesting RI occurs more on the order of 18 hours than the 24 hour period frequently utilized (Kaplan and DeMaria, 2003; 2010). One such example of the 18-hour RI evolution is seen in the case of Hurricane Kenneth (2005) in Figure 71 as the annular structure gains axisymmetry and becomes consolidated.

Structural differences in convective organization and intensity do exist throughout the evolution of RI in each basin but this key chain of events is a constant.

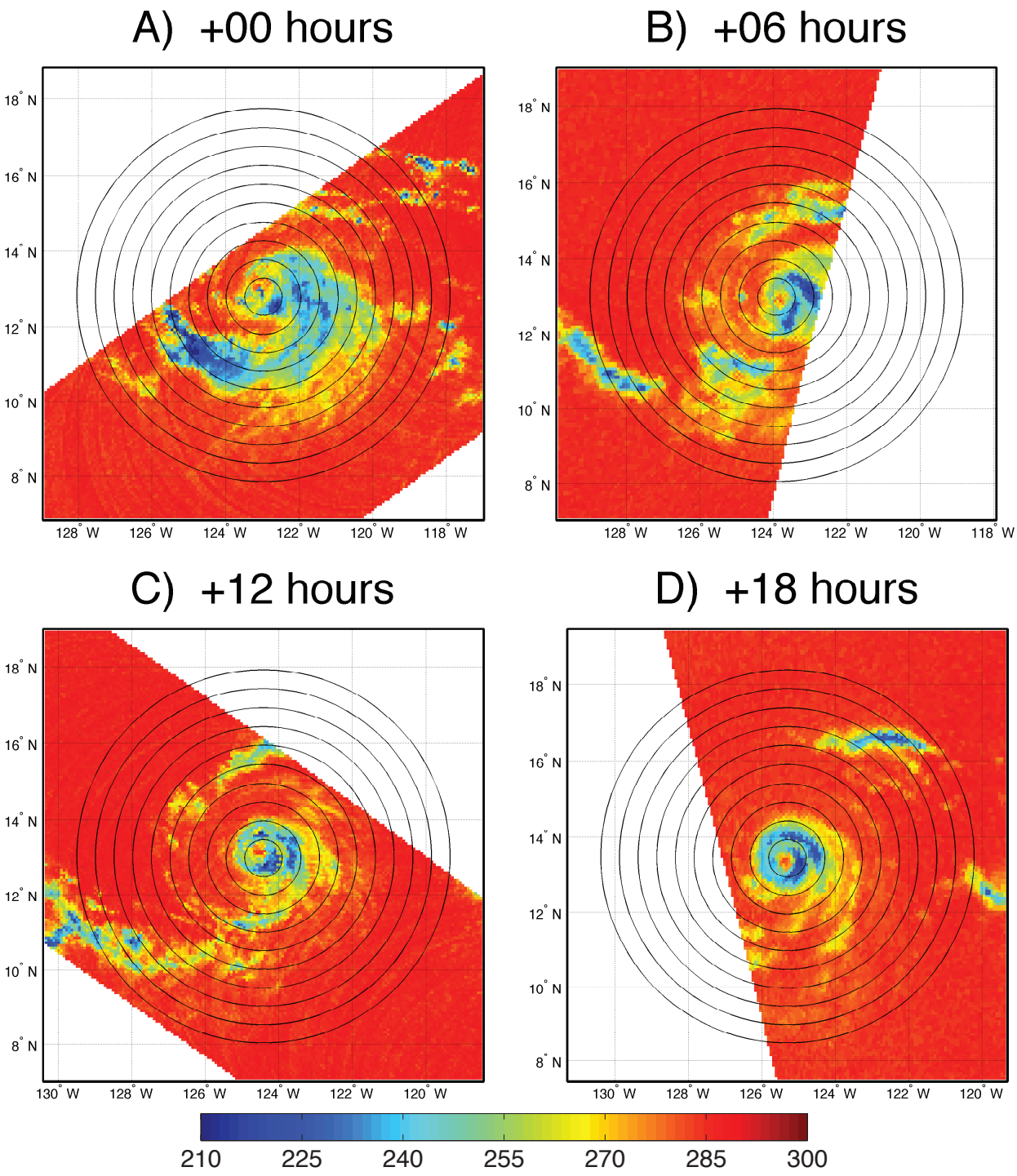

Figure 71: Hurricane Kenneth 85 GHz PCTs from the 2005 season on September (a) 16 at 1158 UTC – 66 kts intensity, (b) 16 at 1727 UTC – 66 kts intensity, (c) 16 at 2149 UTC – 74.8 kts intensity, (d) 17 at 436 UTC – 92.4 kts intensity. Figure (a) and (c) are from TMI while (b) and (d) are from SSM/I about DMSP F15.

With this pattern seen we support the idea of Rogers (2010) of the importance of updraft mass flux in the role of RI, whereby RI can be initiated by latent heat resultant from vigorous convection over a small area (as in Molinari and Vollaro, 2010) or moderate to light convective activity over a larger spatial area. A preference for the axisymmetric structure is seen here which requires further investigation to determine more the frequency of each mode of RI. Further stratification by environmental wind shear values and storm-motion speeds may yield further insight into these modes. Additional modeling studies such as those by Meyers et al. (2010) may also help further quantify the latent heat release necessary for RI to occur in each mode, in addition to the importance of emission and scattering processes.

REFERENCES

Braun, S. A., M. T. Montgomery, and Z. Pu, 2006: High-resolution simulation of Hurricane Bonnie (1998). Part I: The organization of eyewall vertical motion. *J. Atmos. Sci.,* **63,** 19-42.

Cecil, D. J. and E. J. Zipser, 1999: Relationships between tropical cyclone intensity and satellite-based indicators of inner core convection: 85-GHz ice-scattering signature and lightning. *Mon. Wea. Rev.*, **127,** 103-123.

Cecil, D. J., E. J. Zipser, and S. W. Nesbitt, 2002: Reflectivity, ice scattering, and lightning characteristics of hurricane eyewalls and rainbands. Part I: Quantitative description. *Mon. Wea. Rev.,* **130,** 769-784.

Cecil, D. J. and E. J. Zipser, 2002: Reflectivity, ice scattering, and lightning characteristics of hurricane eyewalls and rainbands. Part II: Intercomparison of observations. *Mon. Wea. Rev.,* **130,** 785-801.

Ferrarro, R. R. and G. F. Marks, 1995: The development of SSM/I rain-rate retrieval algorithms using ground-based radar measurements*. J. Atm. Oceanic Tech.,* **12,** 755-770.

Frank, W. M., and E. A. Ritchie, 1999: Effects of environmental flow upon tropical cyclone structure. *Mon. Wea. Rev.,* **127,** 2044-2061.

Frank, W. M., and E. A. Ritchie, 2001: Effects of vertical wind shear on the intensity and structure of numerically simulated hurricanes. *Mon. Wea. Rev.,* **129,** 2249-2269.

Grody, N. C., and F. Weng, 2008: Microwave emission and scattering from deserts: Theory compared with satellite measurements. *IEEE Trans. Geoscience,* **46,** 361-375.

Hollinger, J., R. Lo, G. Poe, R. Savage, and J. Pierce, 1987: *Special Sensor Microwave Imager User's Guide*. Naval Research Laboratory, 120 pp.

Hoshino, S. and T. Nakazawa, 2007: Estimation of tropical cyclone's intensity using TRMM/TMI brightness temperature data. *J. Meteor. Soc. Japan,* **85,** 437-454.

Jones, T. A., D. Cecil, and M. DeMaria, 2006: Passive-microwave-enhanced statistical hurricane intensity prediction scheme. *Wea. Forecasting,* **21,** 613-635.

Jorgensen, D. P., E. J. Zipser, and M. A. LeMone, 1985: Vertical motions in intense hurricanes. *J. Atmos. Sci.,* **42,** 839-856.

Kalney, E., and 21 co-authors, 1996: The NCEP/NCAR 40-year reanalysis project. *Bull. Amer. Met. Soc.,* **77,** 437-471.

Kaplan, J., and M. DeMaria, 2003: Large-scale characteristics of rapidly intensifying tropical cyclones in the North Atlantic basin. *Wea. Forecasting,* **18,** 1093-1108.

Kaplan, J., M. DeMaria, and J. A. Knaff, 2010: A revised tropical cyclone rapid intensification index for the Atlantic and Eastern North Pacific basins. *Wea. Forecasting,* **25,** 220-241.

Kieper, M. E., 2008: A Technique for Anticipating Initial Rapid Increases in Intensity in Tropical Cyclones, Using 37 gHz Microwave Imagery. *28th AMS Conference on Hurricanes and Tropical Meteorology,* Orlando, FL, 28 April - 2 May, 2008.

Knapp, K. R, 2008: Hurricane Satellite (HURSAT) data sets: Low Earth orbit infrared and microwave data. *28th AMS Conference on Hurricanes and Tropical Meteorology,* Orlando, FL, 28 April - 2 May, 2008.

Knapp, K. R., M. C. Kruk, D. H. Levinson, H. J. Diamond, and C. J. Neumann, 2010: The International Best Track Archive for Climate Stewardship (IBTrACS): Unifying tropical cyclone best track data. *Bulletin of the American Meteor. Society,* **91,** 363 -376.

Kummerow, C., W. Barnes, T. Kozu, J. Shiue, and J. Simpson, 1998: The Tropical Rainfall Measuring Mission (TRMM) sensor package. *J. Atmos. Oceanic Tech.,* **15,** 809-817.

Liu, G., and J. A. Curry, 1998: An investigation between the relationship between emission and scattering signals in SSM/I data. *J. Atmos. Sci.,* **55,** 1628-1643.

Lonfat, M., F. D. Marks Jr., and S. S. Chen, 2004: Precipitation Distribution in Tropical Cyclones Using the Tropical Rainfall Measuring Mission (TRMM) Microwave Imager: A Global Perspective. *Mon. Wea. Rev.,* **132,** 1645-1660.

McGaughey, G., E. J. Zipser, R. W. Spencer, and R. E. Hood: High-resolution passive microwave observations of convective systems over the tropical Pacific Ocean. *J. Appl. Meteor.,* **35,** 1921-1947.

Meyers, E. C., G. M. McFarquhar, B. F. Jewett, and S. W. Nesbitt, 2010: Vertical velocity and microphysical distributions related to the rapid intensification of Hurricane Dennis (2005). *29th AMS Conference on Hurricanes and Tropical Meteorology,* Tucson, AZ, 10-14 May, 2010.

Miyamoto, Y., 2010: Axisymmetric and asymmetric processes of tropical cyclone-like vortex during the rapid intensification phase. *29th AMS Conference on Hurricanes and Tropical Meteorology,* Tucson, AZ, 10-14 May, 2010.

Molinari, J., and D. Vollaro, 2010: Rapid intensification of a sheared tropical storm. *Mon. Wea. Rev.,* In press.

Nolan, D. S., and M. T. Montgomery, 2002: Nonhydrostatic, three-dimensional perturbations to balanced, hurricane-like vortices. Part I: Linearized formulation, stability, and evolution. *J. Atmos. Sci.,* **59,** 2989-3020.

Nolan, D. S., and L. D. Grasso, 2003: Nonhydrostatic, three-dimensional perturbations to balanced, hurricane-like vortices. Part II: Symmetric response and nonlinear simulations. *J. Atmos. Sci.,* **60,** 2717–2745.

Pielke Jr., R. A., J. Gratz, C. W. Landsea, D. Collins, M. A. Saunders, and R. Musulin, 2008: Normalized hurricane damage in the United States: 1900-2005. *Nat. Hazards. Rev.,* **9,** 29-42.

Rao. G. V. and P. D. MacArthur, 1994: The SSM/I estimatetd rainfall amounts in tropical cyclones and their potential in predicting the cyclone intensity changes. *Mon. Wea. Rev.,* **122,** 1568-1574.

Rao, G. V. and J. H. McCoy, 1997: SSM/I measured microwave brightness temperature (TB's), anomalies of TB's, and their relationship to typhoon intensification. *Nat. Hazards,* **15,** 1-19.

Rappaport, E.N., and 17 co-authors, 2009: Advances and challenges at the National Hurricane Center. *Wea. Forecasting,* **24,** 395-419.

Roca, R., 2010: The Megha-Tropiques mission. *29th AMS Conference on Hurricanes and Tropical Meteorology,* Tucson, AZ, 10-14 May, 2010.

Rodgers, E. B., S. W. Chang, and H. F. Pierce, 1994: A satellite observational and numerical study of precipitation characteristics in western north Atlantic tropical cyclones. *J. Appl. Meteor.,* **33,** 129-139.

Rodgers, E. B., and H. F. Pierce, 1995: A satellite observational study of precipitation characteristics in western north Pacific tropical cyclones. *J. Appl. Meteor.,* **34,** 2587-2599.

Rogers, R., 2010: Convective-scale structure and evolution during a high-resolution simulation of tropical cyclone rapid intensification. *J. Atmos. Sci.,* **67,** 44-70.

Sears, J., T. Olander, and C. Velden, 2010: Recent statistical analyses of the Advanced Dvorak Technique (ADT). *29th AMS Conference on Hurricanes and Tropical Meteorology,* Tucson, AZ, 10-14 May, 2010.

Smith, E. A., and 31 co-authors, 2004: International Global Precipitation Measurement (GPM) program and mission: An overview. *Measuring Precipitation from Space: EURAINSAT and the Future.,* 1-44.

Spencer, R. W., H. M. Goodman, and R. E. Hood, 1989: Precipitation retrieval over land and ocean with the SSM/I: Identification and characteristics of the scattering signal. *J. Atmos. Oceanic Tech.,* **6,** 254-273.

Rappaport, E. N., and 17 co-authors, 2009: Advances and challenges at the National Hurricane Center. *Wea. Forecasting,* **24,** 395-419.

Velden, C. S., C. Rozoff, A. J. Wimmers, M. Sitkowski, M. E. Kieper, J. Kossin, J. Hawkins, and J. Knaff, 2010: An objective method to predict near real time rapid intensification of tropical cyclones using satellite passive microwave observations. *29th AMS Conference on Hurricanes and Tropical Meteorology,* Tucson, AZ, 10-14 May, 2010.

Vigh, J. L., 2010: Structure and intensity changes during hurricane eye formation. *29th AMS Conference on Hurricanes and Tropical Meteorology,* Tucson, AZ, 10-14 May, 2010.

Vivekanandan, J., J. Turk, and V. N. Bringi, 1991: Ice water path estimation and characterization using passive microwave radiometry. *J. Appl. Meteor.,* **30,** 1407-1421.

Willoughby, H. E., I. Gonzales, and R. J. Hergert, 2010: Predictability of hurricane activity and impacts. *29th AMS Conference on Hurricanes and Tropical Meteorology,* Tucson, AZ, 10-14 May, 2010.

Wimmers, A. J, and C. S. Velden, 2010: Objectively determining the rotational center of tropical cyclones in passive microwave satellite imagery. *J. Appl. Meteor.,* In press.